

# Tissue Engineering in Gene and Cell Therapies for Neurological Disorders

Guest Editors: Jun Liu, William Z. Suo, Xing-Mei Zhang, Chen Zhang, and Gongxiong Wu



# **Tissue Engineering in Gene and Cell Therapies for Neurological Disorders**

## **Tissue Engineering in Gene and Cell Therapies for Neurological Disorders**

Guest Editors: Jun Liu, William Z. Suo, Xing-Mei Zhang,  
Chen Zhang, and Gongxiong Wu



Copyright © 2016 Hindawi Publishing Corporation. All rights reserved.

This is a special issue published in "BioMed Research International." All articles are open access articles distributed under the Creative Commons Attribution License, which permits unrestricted use, distribution, and reproduction in any medium, provided the original work is properly cited.

## Contents

**In Vivo Targeted Magnetic Resonance Imaging of Endogenous Neural Stem Cells in the Adult Rodent Brain**

Xiao-Mei Zhong, Fang Zhang, Ming Yang, Xue-Hua Wen, Xiang Zhang, Xiao-Hui Duan, and Jun Shen  
Volume 2015, Article ID 131054, 11 pages

**Calreticulin Binds to Fas Ligand and Inhibits Neuronal Cell Apoptosis Induced by Ischemia-Reperfusion Injury**

Beilei Chen, Zhengzheng Wu, Jun Xu, and Yun Xu  
Volume 2015, Article ID 895284, 8 pages

**Effects of Nogo-A Silencing on TNF- $\alpha$  and IL-6 Secretion and TH Downregulation in Lipopolysaccharide-Stimulated PC12 Cells**

Jianbin Zhong, Shengnuo Fan, Zhenwen Yan, Songhua Xiao, Limei Wan, Chibang Chen, Simin Zhong, Lu Liu, and Jun Liu  
Volume 2015, Article ID 817914, 6 pages

**Screening and Identification of ssDNA Aptamer for Human GP73**

Jingchun Du, Jianming Hong, Chun Xu, Yuanyuan Cai, Bo Xiang, Chengbo Zhou, and Xia Xu  
Volume 2015, Article ID 610281, 8 pages

**PI3K/AKT/mTOR/p70S6K Pathway Is Involved in A $\beta$ 25-35-Induced Autophagy**

Shengnuo Fan, Bei Zhang, Ping Luan, Beibei Gu, Qing Wan, Xiaoyun Huang, Wang Liao, and Jun Liu  
Volume 2015, Article ID 161020, 9 pages

**Overexpression of NTRK1 Promotes Differentiation of Neural Stem Cells into Cholinergic Neurons**

Limin Wang, Feng He, Zhuoyuan Zhong, Ruiyan Lv, Songhua Xiao, and Zhonglin Liu  
Volume 2015, Article ID 857202, 6 pages

## Editorial

# Tissue Engineering in Gene and Cell Therapies for Neurological Disorders

Jun Liu,<sup>1</sup> William Z. Suo,<sup>2,3</sup> Xing-Mei Zhang,<sup>4</sup> Chen Zhang,<sup>5</sup> and Gongxiong Wu<sup>6</sup>

<sup>1</sup>Department of Neurology, Sun Yat-sen Memorial Hospital, Sun Yat-sen University, Guangzhou, Guangdong 510120, China

<sup>2</sup>Laboratory for Alzheimer's Disease and Aging Research, Veterans Affairs Medical Center, Kansas City, MO 64128, USA

<sup>3</sup>Department of Neurology, University of Kansas Medical College, Kansas City, MO 64128, USA

<sup>4</sup>Immunology-Immunotherapy, Department of Clinical Neuroscience, Karolinska Institutet, 171 76 Stockholm, Sweden

<sup>5</sup>State Key Laboratory of Membrane Biology, School of Life Sciences, PKU-IDG/McGovern Institute for Brain Research, Peking University, Beijing 100871, China

<sup>6</sup>Laboratory for Translational Research, Harvard Medical School, Cambridge, MA 02215, USA

Correspondence should be addressed to Jun Liu; docliu jun@hotmail.com

Received 25 October 2015; Accepted 27 October 2015

Copyright © 2016 Jun Liu et al. This is an open access article distributed under the Creative Commons Attribution License, which permits unrestricted use, distribution, and reproduction in any medium, provided the original work is properly cited.

Neurological diseases such as stroke, encephalitis, neurologic tumors, and neurodegenerative diseases are far from alien to us. These diseases are refractory, harmful, and sometimes devastating. The pathogenesis of some nervous system diseases remains elusive, especially the neurodegenerative diseases such as AD and PD. Many therapeutic strategies have been developed to potentially intervene in these progressive neurodegenerative events and minimize damage to the CNS. Despite the promising results that these researches have shown in in vivo and in vitro studies, challenges still remain, particularly when it comes to clinical translation. The causes are various, which may include biologic and physiologic differences between the preclinical models and the human condition and discrepancies in dosing and the timing of drug therapy. The last few years have witnessed an explosion in the use of genes and cells as biomedicines. Gene and cell therapies are researches with the goals of repairing the direct cause of genetic diseases in the DNA or cellular population, respectively. In many diseases, gene and cell therapies are combined in the development of promising therapies, which have helped provide reagents, concepts, and techniques that are elucidating the finer points of gene regulation, stem cell lineage, regenerative capacity, and remodeling. Additionally, increasing studies of novel drug delivery systems bring more considerable future on gene and cell therapies.

This special issue mainly focuses on the latest ideas, developments, and applications in the field of gene and cell therapies for neurological disorders, most notably development of highly efficient gene expression and delivery system including viral and nonviral gene vectors for tissue repair in the nervous system; exploration and evaluation of the efficiency of new ideal routes of administration of gene and cells into brain; evaluation of appropriate biomaterials in terms of biocompatibility and biodegradability, biomechanical competency, and functionalization with instructive cues to guide neuroregeneration; tissue engineering that integrates cell therapies and scaffolding technologies to replace damaged neurons and to reestablish the coaxial connection of neuronal circuits for functional recovery; assessment of the safety and toxic side effects with gene and cell therapies; latest technologies of noninvasive in vivo imaging to track the transplanted gene or cells; new insights into the pathogenesis of neurological disorders by using cellular or animal models.

In the accepted papers, researches of pathogenesis of some diseases, such as  $A\beta$ -induced autophagy in AD and ischemia-reperfusion injury induced apoptosis in stroke, were discussed. Studying specific aptamer for GP73 through systematic evolution of ligands by exponential enrichment and identifying its application in detecting hepatocellular carcinoma might provide a novel molecular probe for cell

therapy. In vivo targeted MR imaging of endogenous neural stem cells (NSCs) in adult mouse brain by using certain nanoparticles offered a promising molecular probe in NSCs research. Moreover, the role of Nogo-A in PD and NTRK1 in NSCs differentiation was preliminarily explored. These findings above provided new insights into the pathogenesis of certain diseases and also represented part of the latest ideas, developments, and applications in the field of gene and cell therapies for neurological disorders.

*Jun Liu  
William Z. Suo  
Xing-Mei Zhang  
Chen Zhang  
Gongxiong Wu*

## Research Article

# In Vivo Targeted Magnetic Resonance Imaging of Endogenous Neural Stem Cells in the Adult Rodent Brain

Xiao-Mei Zhong,<sup>1</sup> Fang Zhang,<sup>1</sup> Ming Yang,<sup>2</sup> Xue-Hua Wen,<sup>1</sup>  
Xiang Zhang,<sup>1</sup> Xiao-Hui Duan,<sup>1</sup> and Jun Shen<sup>1</sup>

<sup>1</sup>Department of Radiology, Sun Yat-Sen Memorial Hospital, Sun Yat-Sen University, No. 107 Yanjiang Road West, Guangzhou, Guangdong 510120, China

<sup>2</sup>Department of Radiology, Zhongda Hospital of Southeast University, Nanjing 210009, China

Correspondence should be addressed to Jun Shen; shenjun@mail.sysu.edu.cn

Received 2 July 2015; Accepted 11 August 2015

Academic Editor: William Z. Suo

Copyright © 2015 Xiao-Mei Zhong et al. This is an open access article distributed under the Creative Commons Attribution License, which permits unrestricted use, distribution, and reproduction in any medium, provided the original work is properly cited.

Neural stem cells in the adult mammalian brain have a significant level of neurogenesis plasticity. In vivo monitoring of adult endogenous NSCs would be of great benefit to the understanding of the neurogenesis plasticity under normal and pathological conditions. Here we show the feasibility of in vivo targeted MR imaging of endogenous NSCs in adult mouse brain by intraventricular delivery of monoclonal anti-CD15 antibody conjugated superparamagnetic iron oxide nanoparticles. After intraventricular administration of these nanoparticles, the subpopulation of NSCs in the anterior subventricular zone and the beginning of the rostral migratory stream could be *in situ* labeled and were in vivo visualized with 7.0-T MR imaging during a period from 1 day to 7 days after the injection. Histology confirmed that the injected targeted nanoparticles were specifically bound to CD15 positive cells and their surrounding extracellular matrix. Our results suggest that in vivo targeted MR imaging of endogenous neural stem cells in adult rodent brain could be achieved by using anti-CD15-SPIONs as the molecular probe; and this targeting imaging strategy has the advantage of a rapid in vivo monitoring of the subpopulation of endogenous NSCs in adult brains.

## 1. Introduction

Neural stem/progenitor cells (NSCs) persist in the adult rodent brain and have been identified in the subventricular zone (SVZ) of the lateral wall of the lateral ventricle and the hippocampus. The SVZ is the largest source of progenitors in the brain. Primary progenitors in this region correspond to type B cells, which have properties of astrocytes. These cells divide to generate transit-amplifying type C cells, which generate new neurons that migrate along a well-defined pathway, the rostral migratory stream (RMS), to the olfactory bulbs (OBs) where they differentiate into interneurons [1].

The SVZ retains a significant level of plasticity, where the generation and flow of cells change in response to signals from the anatomically remote areas of the brain or even from the external environment of the organism. Following

cerebral ischemia [2], traumatic brain injury [3], or stroke [4], NSCs and neuroblasts respond by proliferation and migration towards damaged brain regions and subsequently differentiate into the phenotype of the destroyed cells [5, 6]. Disturbed adult neurogenesis has also been found in neurodegenerative diseases such as Huntington's disease, Alzheimer's disease, and Parkinson's disease [4, 7, 8]. The intrinsic sensitivity and responsiveness of SVZ to disease states raise the prospect of direct manipulation of endogenous NSCs to develop new cell replacement strategies to enhance the neurogenic response of the SVZ and contribution to brain repair [9, 10].

Development of methods capable of in vivo monitoring and tracking of endogenous NSCs would be of great benefit to the understanding of the plasticity of the SVZ under normal and pathological conditions and will be essential to ensure the safety and efficacy of neurogenesis-based therapies. To date,

numerous studies had investigated the adult neurogenesis and NSC migration from SVZ by using the methods of thymidine [11], retroviruses [12], bromodeoxyuridine (BrdU) labeling [13], and transgenic systems [14, 15], whereas all of these labeling methods rely on ex vivo processing of tissue, thus limiting the ability for longitudinal studying of the neurogenesis and migration throughout the brain within a living animal.

It has been reported that magnetic resonance spectroscopy can be used to in vivo monitor endogenous NSCs based on a distinct peak of NSCs in the spectroscopic profile [16]. However, this metabolic biomarker, previously believed to be exclusive to NSCs, was demonstrated to be nonspecific for NSCs [17]. Recently, injection of micron-sized particles of iron oxide (MPIOs) or superparamagnetic iron oxide nanoparticles (SPIONs) into the lateral ventricle [18–22] or directly into the anterior SVZ [21] has been demonstrated successfully in situ to label endogenous NSCs in adult or postnatal developing rodent brains; as such, NSCs migration under normal condition [18–22] or migration towards hypoxia-ischemia lesion sites under pathological conditions could be monitored in vivo by MR imaging [23]. These approaches offer the unique advantage of in situ labeling and in vivo study of NSCs. However, these strategies suffer from some limitations. For example, the injected MPIOs could result in a large degree of signal inhomogeneity (loss of signal intensity) and image distortion on the MR images, which hampers the visualization of the SVZ and beginning of the RMS. This shortcoming could be overcome in part either by combined use of transfection agents such as poly-L-lysine or protamine sulphate or by reducing the number of MPIOs used [20] or decreasing the size of the iron oxide particles needed [21]. Most importantly, these labeling strategies suffered from an intrinsic limitation of nontargeting [18–23]. The iron oxide particles used were unmodified and have a low labeling efficiency (~30%) [19]. After administration, these iron oxide particles were nonselectively endocytosed by all cells residing within the SVZ but not exclusively by NSCs; therefore the migrating dynamics of cells with RMS were essential to transport iron oxides and play a critical role in MR imaging of endogenous NSCs.

Previous cell biological study showed that a cell surface biomarker, the LeX antigen, which is the trisaccharide 3-fucosyl-N-acetyllactosamine, also known as SSEA-1 (stage-specific embryonic antigen 1) or CD15 antigen, was highly and specifically expressed by adult mouse NSCs and shed into their microenvironment within the SVZ [24]. In view of this specific expression of CD15 antigen by a subpopulation of adult NSCs, in this study we investigate the feasibility of in vivo targeted MR imaging of endogenous NSCs in healthy adult rodent brains by using anti-CD15 monoclonal antibody-conjugated SPIONs (anti-CD15-SPIONs) as the molecular probe.

## 2. Materials and Methods

**2.1. Animals.** Adult 8–10-week-old C57BL/6J mice (weighing 20–25 g) were obtained from the Laboratory Animal Center of Sun Yat-Sen University. All animals were housed in a

standard animal facility with 12 h on/off light conditions and allowed standard food and water ad libitum. All experimental procedures adhered to the guidelines for the care and use of laboratory animals and the ethical review process of our institution and were approved by the Institutional Animal Care and Use Committee.

**2.2. Characterization of Anti-CD15-SPIONs.** Commercially available SPIONs (Miltenyi Biotec, Bergisch Gladbach, Germany), conjugated with a monoclonal rat anti-mouse CD15 IgM antibody, stabilized with sodium citrate, and approved for clinical use in humans as magnetic cell separators, were used as the targeted probe. These iron oxide particles were composed of a biodegradable, nontoxic dextran-based ferromagnetic matrix, and their nominal overall mean diameter was approximately 50 nm. Assuming a diameter of 30 nm for the magnetic core, there were typically 10–200 antibody molecules per particle [25]. SPIONs conjugated with anti-mouse IgM antibody (Miltenyi Biotec, Bergisch Gladbach, Germany) were used as nontargeted control probe. To verify the conjugation of anti-CD15 antibody to the SPIONs, anti-CD15-SPIONs were tested with FITC-conjugated anti-mouse IgM (1:200, Chemicon, CA, USA) for 30 min and observed under a fluorescence microscope (TE2000-U, Nikon Company, Japan). The actual average size of anti-CD15-SPIONs used was determined by using a transmission electron (JEM-2010HR, JEOL, Japan) operated at 160 kV. Their actual iron content was measured by inductively coupled plasma optical emission spectrometry using a polarized Zeeman Atomic Absorption Spectrophotometer (AAS, Z-2000, Hitachi, Japan) and their  $r_2$  relaxivity was assessed at 1.5-T MR scanner (Philips Intera, Best, Netherlands) by measuring particles in vitro at room temperature (~25°C).

**2.3. Cell Sorting Using Anti-CD15-SPIONs.** To verify the specific expression of CD15 antigen of NSCs in SVZ, acutely isolated SVZ cell suspensions were labeled with anti-CD15-SPIONs and then were sorted using a magnetic-activated cell sorting method according to the manufacturer's instructions. In brief, single cell suspension was obtained from dissociated SVZ of five adult mouse brains, as described previously [24]. Then the cells were incubated with anti-CD15-SPIONs for 30 min on ice. After being washed twice with 0.1 M phosphate-buffered saline (PBS), cells were sorted on a CliniMACS system (CliniMACS, Miltenyi Biotec, Bergisch Gladbach, Germany). The sorted CD15 positive cells were collected and then were cultured in a plastic flask at a density of  $5 \times 10^4$  viable cells/cm<sup>2</sup> in a humidified incubator at 37°C with 95% air and 5% CO<sub>2</sub>. The culture medium was serum-free DMEM/F12 (Dulbecco's modified Eagle's medium: nutrient mixture F12, 1:1, Gibco, NY, USA), supplemented with components which consisted of basic fibroblast growth factor (bFGF, 20 ng/mL, R&D systems, MN, USA), epidermal growth factor (EGF, 20 ng/mL, R&D systems), and B27 Supplement (Gibco). The culture medium was replenished regularly until typical neurospheres were generated. The generated neurospheres were identified and characterized by using immunofluorescence staining for Nestin and CD15. For immunofluorescent staining, cells were

fixed with 4% paraformaldehyde for 45 min. Then, the cells were incubated with the primary antibodies against Nestin (1:200, Chemicon, CA, USA) and against CD15 (1:200, BD Pharmingen, CA, USA) overnight at 4°C in 0.1 M PBS. Afterwards, the cells were incubated with the secondary antibody, Cy3-conjugated anti-mouse IgG (1:100, Chemicon, CA, USA), or FITC-conjugated anti-mouse IgM (1:200, Chemicon, CA, USA) for 30 min.

To determine whether the subpopulation of sorted CD15 positive cells exhibit the stem cell properties, the obtained neurospheres were then transferred to the culture medium containing 10% fetal bovine serum (FBS, Gibco) to induce lineage differentiation. After 7–10 days of induction, cells were identified by immunofluorescence staining for neural cell phenotype specific markers including glial fibrillary acidic protein (GFAP), microtubule-associated protein 2 (MAP2), and O4. Differentiated cells were incubated with the primary antibodies against GFAP (1:100, Thermo Fisher Scientific, CA, USA) or MAP2 (1:100, Thermo Fisher Scientific, CA, USA) or O4 (1:100, Chemicon, CA, USA) overnight at 4°C in 0.1 M PBS; then Cy3-conjugated secondary IgG antibody (1:100, Chemicon), TR-conjugated secondary IgG antibody (1:100, Santa Cruz, CA, USA), or FITC-conjugated secondary IgM antibody (1:100, Chemicon) was applied to determine whether these cells could demonstrate glial differentiation, neuronal differentiation, and oligodendrocytic differentiation, respectively. Fluorescence images were obtained on a fluorescence microscope (TE2000-U, Nikon Company, Japan).

**2.4. In Vitro Binding of Anti-CD15-SPIONs.** To detect the in vitro binding of anti-CD15-SPIONs to NSCs, the obtained neurospheres were triturated until single cell suspension was achieved.  $10^6$  single cells were incubated with 20  $\mu$ L anti-CD15-SPIONs at 4°C for 15 min in 80  $\mu$ L 0.1 M PBS. Then the cells were washed three times with PBS by centrifugation (5 min, 300  $\times g$ , 25°C) to remove excess unbound particles. The presence of anti-CD15-SPIONs binding was verified by Prussian blue staining. The average iron content of cells was determined by AAS and the distribution of nanoparticles was determined by using transmission electron microscopy. The cells with anti-CD15-SPION binding were assessed by using in vitro MR imaging. The same number of untreated NSCs and cells incubated with nontargeted SPIONs or anti-CD15 mAb alone under the same condition was used as negative controls.

For Prussian blue staining, cells were fixed with 4% glutaraldehyde, washed, incubated for 30 minutes with 10% potassium ferrocyanide (Perls reagent) in 15% hydrochloric acid, and then washed and counterstained with nuclear fast red. For iron content measurement, cells were suspended in 10 mL 1 M HCl solutions for at least 24 hours. Then, the iron concentration of cells was determined by AAS. For electron microscopy, cells were fixed in 3% glutaraldehyde-cacodylate buffer at 3°C overnight and then fixed for 1 h in 1% OsO<sub>4</sub>. After being dehydrated in graded dilutions of ethanol, cells were embedded in artificial resin (Epon, Merck, Darmstadt, Germany) and processed for electron microscopy. Thin sections of the cell probes were evaluated unstained (i.e.,

without double staining with uranyl acetate and lead citrate) to prevent false-positive findings. The presence and localization of SPIONs were observed under transmission electron microscopy (CM-10, Philips, Eindhoven, Netherlands) at 60–80 kV. For in vitro MR imaging, the cell pellets were collected in 1.5 mL EP tubes and resuspended in 50  $\mu$ L 4% gelatin solution and then imaged.

**2.5. In Vitro MR Imaging.** In vitro MR imaging was performed at a clinical 1.5-T MR scanner (Intera, Philips Medical Systems, Best, Netherlands) and a circular 11 cm surface coil was used. MR pulse sequences included two-dimensional T2-weighted fast spin-echo sequences (repetition time/echo time msec, 2600/100; turbo spin-echo factor, 15; matrix, 384  $\times$  256; number of signals acquired, 2; section thickness, 1.5 mm; field of view, 90 mm) and two-dimensional T2\*-weighted fast field echo sequences (210/18; matrix, 304  $\times$  256; flip angel, 30°; number of signals acquired, 2; section thickness, 1.5 mm; field of view, 90 mm). T2 relaxation data were acquired by using a multi-spin-echo sequence. The following parameters were used: repetition time, 2000 ms; stepped echo time, 20–160 msec for eight steps; echo spacing, 20 msec; field of view, 90 mm; matrix, 256  $\times$  256; section thickness, 1.5 mm; number of signals acquired, 2. T2 maps were calculated from T2 relaxation data with the available software tools provided by the manufacturer, which are based on least-squares algorithms [26]. On T2 maps, T2 values were derived by means of region-of-interest measurements. During measurement, a circular region of interest was used with a minimum of 15 pixels per region. Each experiment of in vitro MR imaging was repeated eight times. For measurement of  $r_2$  relaxivity of the nanoparticles, T2 relaxivity ( $s^{-1} \text{mM}^{-1}$ ) was calculated through the curve fitting of 1/T2 relaxation time ( $s^{-1}$ ) versus the magnetic atoms (Fe) concentration (mM).

**2.6. Surgical Injection.** Thirty-six 8–10-week-old adult C57BL/6J mice were randomly divided into three groups: targeted group ( $n = 12$ ), in which animals received stereotactic injection of 7  $\mu$ L anti-CD15-SPIONs; nontargeted group ( $n = 12$ ), in which 7  $\mu$ L nontargeted IgM SPIONs were injected; medium alone group ( $n = 12$ ), in which 7  $\mu$ L anti-CD15 mAb alone ( $n = 9$ ) or 7  $\mu$ L PBS ( $n = 3$ ) was injected. Before injection, the iron content of the nontargeted SPIONs was adjusted to be the same as that of the anti-CD15-SPIONs by dilution with PBS. For injection, mice were anesthetized using isoflurane and were placed in a stereotaxic frame. The head was shaved and ~1 cm incision was made to expose the skull. The injection into the anterior portion of the right lateral ventricles (stereotaxic coordinates: 0.95 mm lateral to bregma, 0.02 mm rostral to bregma, and 2.6 mm deep from the pial surface) was performed by an author (X.M.Z, with 3-year experience with microsurgical procedures), using a 26s gauge needle attached to a 10  $\mu$ L Hamilton syringe mounted on a microinjector. The medium was slowly injected at a constant rate of 0.5  $\mu$ L/min. After injection, the needle was left in place for additional 5 min and then slowly withdrawn. The skin over the skull was sutured closed and animals were placed in separate, heated cages and monitored until fully

recovered. Brain MR imaging was performed before injection (baseline data) and at 1, 3, 7, and 10 days after injection.

**2.7. In Vivo MR Imaging.** After intraventricular injection, brain MR imaging was performed at 7.0T micro-MR scanner (PharmaScan, Bruker, Germany) with a 23 mm mouse brain coil. During MR imaging, mice were positioned in a plastic holder with a stereotaxic head-frame and anesthetized by isoflurane (1–1.5% at 0.8–1.0 L/min air flow via a nose cone) with respiratory monitoring. Axial, coronal, and sagittal brain images were obtained. The pulse sequences included two-dimensional T2\*-weighted fast low angle shot gradient echo sequence (400/3.5; flip angle, 30°; matrix, 256 × 256; field of view, 30 mm; number of signals acquired, 8; section thickness, 0.5 mm; section gap, 0) and two-dimensional T2-weighted turbo rapid acquisition with relaxation enhancement sequence (6000/60; matrix, 256 × 256; field of view, 30 mm; number of signals acquired, 6; section thickness, 0.5 mm; section gap, 0). On T2\*-weighted imaging, the signal intensity of RMS was measured by an author (J.S., with more than 12-year experience with MR imaging), using the technique of region of interest with a minimum size of 50 pixels and the decrease of signal intensity was normalized to the contralateral normal brain parenchyma.

**2.8. Histology.** In animals that received anti-CD15-SPION or IgM SPION injection, two animals of each of them were randomly sacrificed for histological assessment after MR imaging at 1 day and 3 days after injection. In animals that received anti-CD15 mAb or PBS injection, one animal was randomly sacrificed at 1 day and 3 days after injection. The animals were anesthetized with a dose of 10% chloral hydrate (350 mg/kg) intraperitoneally and were then transcardially perfused with saline followed by 4% paraformaldehyde in PBS. The brains were removed, fixed in 10% paraformaldehyde overnight, and then cryoprotected in 30% sucrose solution. Contiguous 5 μm thickness sagittal sections were cut and processed for diaminobenzide- (DAB-) enhanced Prussian blue staining to determine the distribution of nanoparticles and immunofluorescence staining for CD15 and Nestin to verify the presence of anti-CD15 SPIONs.

For DAB-enhanced Prussian blue staining, sections were incubated with 2 mL Prussian blue solution containing 15% hydrochloride and 10% potassium ferrocyanide (II) trihydrate for 30 min at 37°C and then reacted with unactivated and activated (containing 0.03% hydrogen peroxide) 0.014% diaminobenzide for 15 minutes each, washed three times, and then counterstained with nuclear fast red. For immunofluorescence staining, sections were incubated with the primary antibodies against Nestin (1:200, Chemicon) or CD15 (1:200, BD Pharmingen) overnight at 4°C. The secondary antibody Cy3-conjugated anti-mouse IgG (Chemicon) or FITC-conjugated anti-mouse IgM (Chemicon) was applied for 30 min at room temperature. DAPI (1:1,000, Sigma-Aldrich, St. Louis, MO) was used to label the nuclei. Fluorescence images were obtained on a confocal microscope (LSM 510, Carl Zeiss Inc., Germany) or a fluorescence microscope (TE2000-U, Nikon Company, Japan).

**2.9. Statistical Analysis.** Data were expressed as mean ± SD. Analysis of variance significance (ANOVA) was performed to test for statistical significance in T2 values between cells incubated with anti-CD15-SPIONs and control cells. The normalized signal intensity of RMS was compared among animals injected with different medium by using a repeated-measures one-way ANOVA test, followed by the Bonferroni post hoc test for multiple pairwise comparisons among different times. Statistical analysis was performed with SPSS 13.0 software for Windows.  $P < 0.05$  was considered to indicate a statistically significant difference.

### 3. Results

**3.1. Characterization of Anti-CD15-SPIONs.** The obtained anti-CD15-SPIONs were strongly positive for anti-CD15 fluorescence staining. Their actual average size was  $73.77 \pm 10.11$  nm, as determined by transmission electron microscopy, and the iron concentration was  $2.58 \mu\text{mol}/\text{mL}$ . The measured  $r_2$  of anti-CD15-SPIONs and nontargeted IgM SPIONs was  $0.30 \times 10^6$  and  $0.468 \times 10^6 \text{ mol}^{-1} \cdot \text{s}^{-1}$ , respectively (Figure 1).

**3.2. Cell Sorting.** After being sorted by anti-CD15-SPIONs, the obtained cell subpopulation from mouse SVZ could self-renew and generate numerous neurospheres after 72 h of culturing (Figure 2(a)). Immunofluorescence staining showed that these neurospheres were positive for anti-CD15 staining but weakly positive for anti-Nestin staining (Figures 2(b) and 2(c)). After induction, the differentiated cells were positive for GFAP or MAP2 or O4 staining (Figures 2(d), 2(e), and 2(f)).

**3.3. In Vitro Cell Binding of CD15-SPIONs.** After incubation with anti-CD15-SPIONs, cells showed positive staining for CD15. Unlike endosome incorporation of iron oxide nanoparticles present in exogenous stem cell labeling, the anti-CD15 SPIONs were bound to the cell membrane via antigen-antibody interaction as revealed by Prussian blue staining and electron microscopy (Figure 3). No high-density electron particles of the iron oxide nanoparticle were present within the cytoplasm.

Compared with control cells, cells incubated with anti-CD15-SPIONs showed significantly decreased signal intensity on T2-weighted imaging and T2\*-weighted imaging (Figure 4). T2 values of cells incubated with anti-CD15-SPIONs, nontargeted SPIONs, anti-CD15 mAb, and untreated cells were  $40 \pm 4$  ms,  $145 \pm 9$  ms,  $278 \pm 20$  ms, and  $323 \pm 30$  ms, respectively (Figure 5). T2 value of cells labeled with anti-CD15-SPIONs was eight times shorter than that of unlabeled cells ( $P < 0.001$ ). The mean iron concentration of cells incubated with anti-CD15 SPIONs was 19.279 pg in a single cell.

**3.4. In Vivo MR Imaging.** Baseline data showed that RMS was visualized as a linear structure with slight hypointense signal on T2-weighted imaging and T2\*-weighted imaging compared with surrounding cerebellar parenchyma. At 1 day after intraventricular injection of anti-CD15-SPIONs, spotty

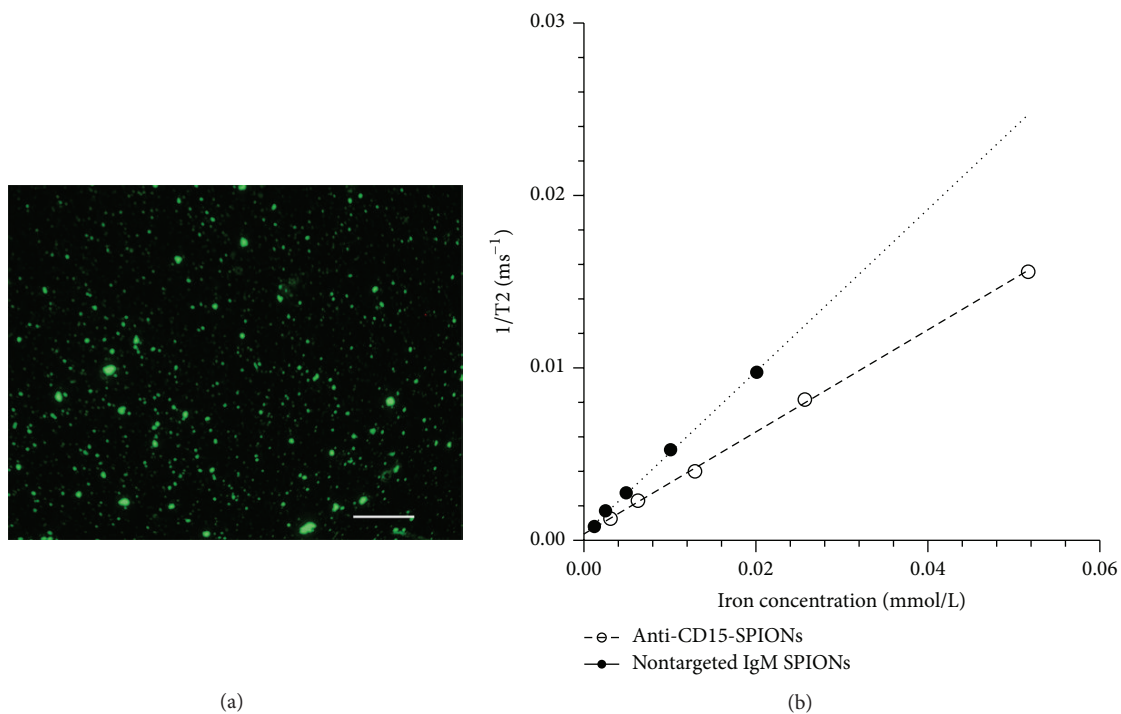


FIGURE 1: Characteristics of anti-CD15-SPIONs. Fluorescence micrograph (a) shows that anti-CD15-SPIONs were substantially positive for anti-mouse IgM staining (bar = 100  $\mu\text{m}$ ). Graphs (b) show  $r_2$  relaxivity of anti-CD15-SPIONs and nontargeted IgM SPIONs (b).

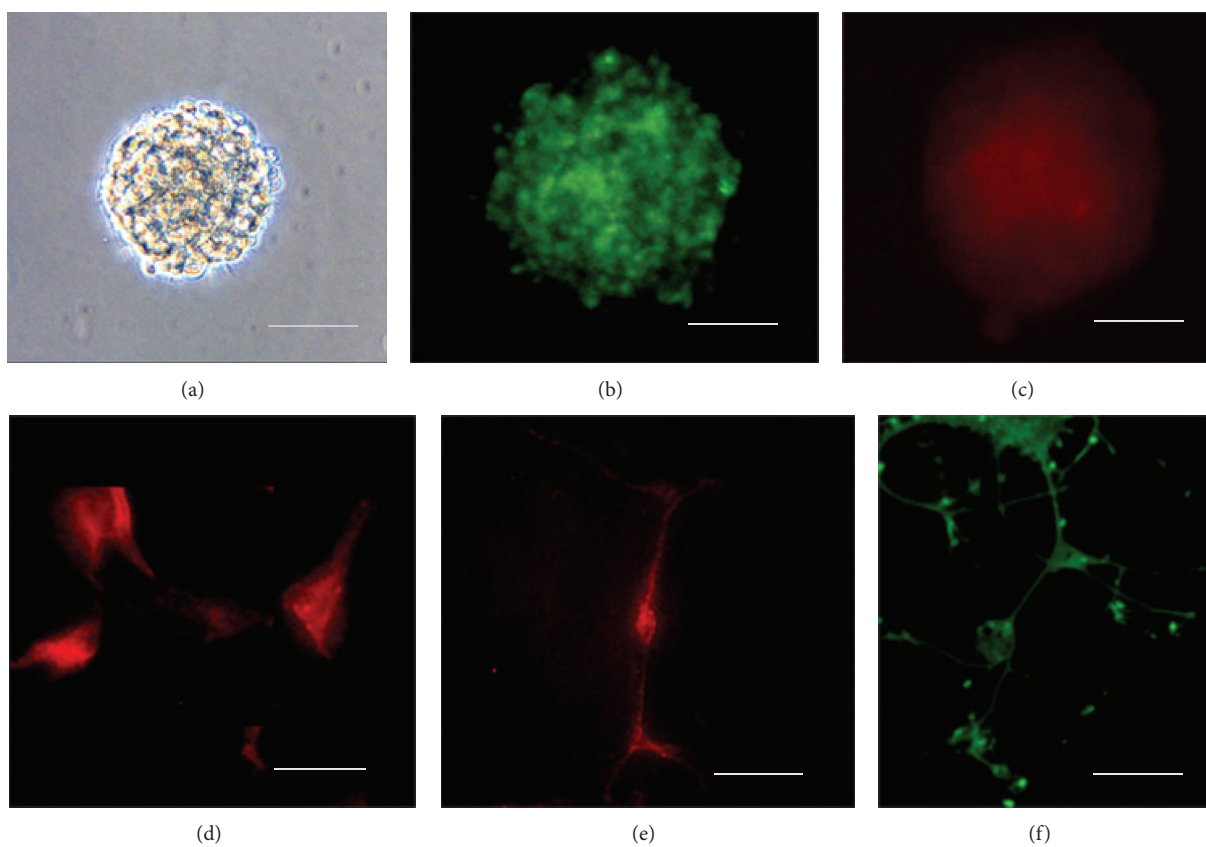


FIGURE 2: Stem cell properties of CD15 positive cells sorted from SVZ. Light microscopy micrograph shows that the sorted CD15 positive cells from SVZ could generate typical neurospheres after in vitro culturing (a). Fluorescence micrographs show that these neurospheres were positive for CD15 staining (b) and weakly positive for Nestin staining (c) and could be differentiated into cells, which are positive for GFAP (d) or MAP2 (e) or O4 staining (f). Bars in (a), (b), (c), and (f) equal 50  $\mu\text{m}$ ; bars in (d) and (e) equal 25  $\mu\text{m}$ .

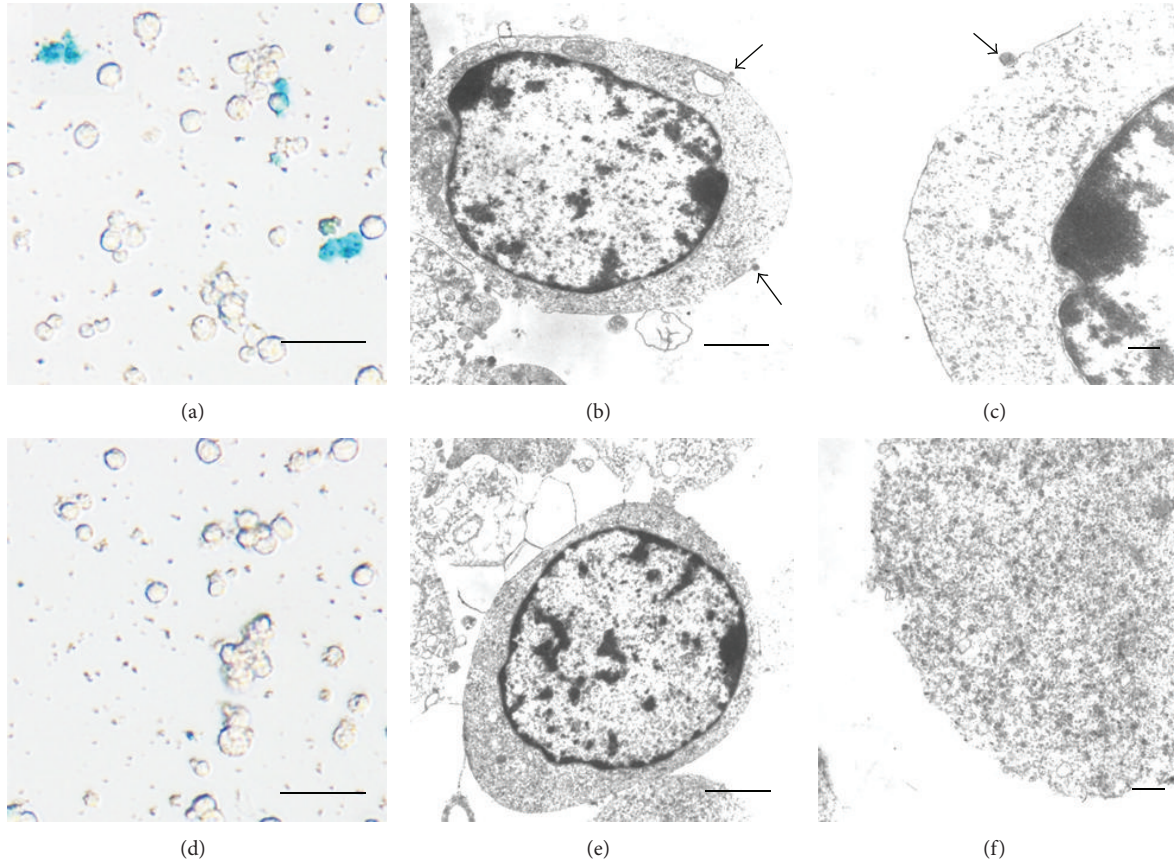


FIGURE 3: Histologic assessment of in vitro cell binding of anti-CD15-SPIONs. Prussian blue staining (a, d) and electron microscopy micrographs (b, c, e, f) demonstrate that the positive SPIONs (arrows) are bound to the cell membrane after cells were incubated with anti-CD15-SPIONs (a, b, c), while there is absence of positive SPIONs when cells were incubated with nontargeted SPIONs (d, e, f). Bars in (a) and (d) equal  $25\text{ }\mu\text{m}$ ; bars in (b), (c), (e), and (f) equal  $1\text{ }\mu\text{m}$ .

hypointense signal was present in SVZ and linear hypointense signal in the beginning of the RMS on T2-weighted imaging and T2<sup>\*</sup>-weighted imaging. This decreased signal intensity persisted to 3 days after injection and returned to almost baseline level by 7 days after injection while it almost disappeared by 10 days after injection. Note that there was no hypointense artifact associated with the iron oxide particles found within and around lateral ventricles. In contrast, there was no such developing hypointense signal found in the SVZ and RMS of animals injected with either nontargeted SPIONs or antibody or PBS alone during the entire study period (Figure 6).

The measured T2<sup>\*</sup> signal intensity of RMS of each group was shown in Table 1. At 1 day and 3 days after injection, the signal intensity was significantly lower in animals receiving anti-CD15-SPIONs ( $P < 0.01$ ) but recovered over time, to preinjection level until 7 days after injection ( $P < 0.05$ ). No statistical difference was found between animals injected with nontargeted SPIONs and those with simple mAb or PBS at each time point ( $P = 0.172$ – $1.000$ ) (Figure 7).

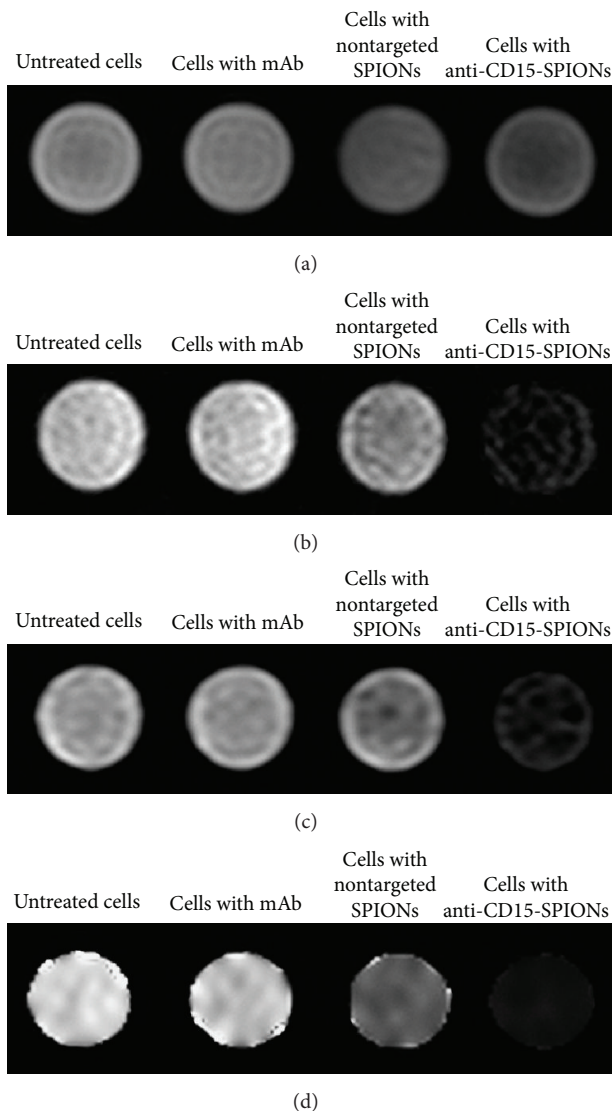
Whether animals received anti-CD15 or nontargeted SPIONs, a hypointense signal was present in the corpus callosum. To determine whether the decreased signal observed in the RMS resulted from the rostral diffusion of nanoparticles

TABLE 1: The signal intensity decrease of the RMS.

Follow-up	Targeted group (n = 8)	Nontargeted group (n = 8)	Medium alone (n = 8)
0 d	$0.140 \pm 0.024$	$0.156 \pm 0.029$	$0.134 \pm 0.030$
1 d	$0.463 \pm 0.032$	$0.160 \pm 0.031$	$0.155 \pm 0.032$
3 d	$0.328 \pm 0.057$	$0.145 \pm 0.029$	$0.122 \pm 0.025$
7 d	$0.237 \pm 0.025$	$0.109 \pm 0.031$	$0.140 \pm 0.024$
10 d	$0.182 \pm 0.028$	$0.118 \pm 0.041$	$0.126 \pm 0.021$

Note. There were 8 animals yielding complete data in the animals injected with anti-CD15-SPIONs or nontargeted SPIONs or medium alone. The signal intensity decrease of the RMS was normalized to the contralateral normal brain parenchyma.

along the corpus callosum,  $7\text{ }\mu\text{L}$  anti-CD15-SPIONs were dedicatedly injected into the corpus callosum in another three animals. After injection, the expected hypointense signal occurred in the corpus callosum, whereas no concurrent hypointense signal intensity was found in the RMS even though the decreased signal intensity of the corpus callosum persisted to 7 days following injection. DAB-enhanced Prussian blue staining confirmed that there were no anti-CD15-SPIONs present within the SVZ and the RMS (Figure 8).



**FIGURE 4:** In vitro MRI of cells binding to anti-CD15-SPIONs. Cells incubated with anti-CD15 SPIONs show decreased signal intensity on T1-weighted imaging (a), T2-weighted imaging (b), and T2\*-weighted imaging (c) and T2 map (d) in comparison with negative control cells.

**3.5. Histology.** DAB-enhanced Prussian blue staining revealed that there were positive cells within SVZ and RMS of animals injected with anti-CD15-SPIONs at 1 day and 3 days after injection. A majority of nanoparticles were present not only in cells but also within extracellular matrix (Figure 9). The location of these SPIONs was well matched with hypointense signal observed on MR imaging. Immunofluorescence staining confirmed the presence and distribution of anti-CD15-SPIONs in the SVZ and RMS. Confocal microscopy images showed that those cells binding anti-CD15-SPIONs were positive for CD15 staining, whereas they were negative for Nestin staining. In contrast, no positive SPIONs were found in the SVZ or RMS of animals injected with nontargeted SPIONs or mAb or PBS alone (Figure 9).

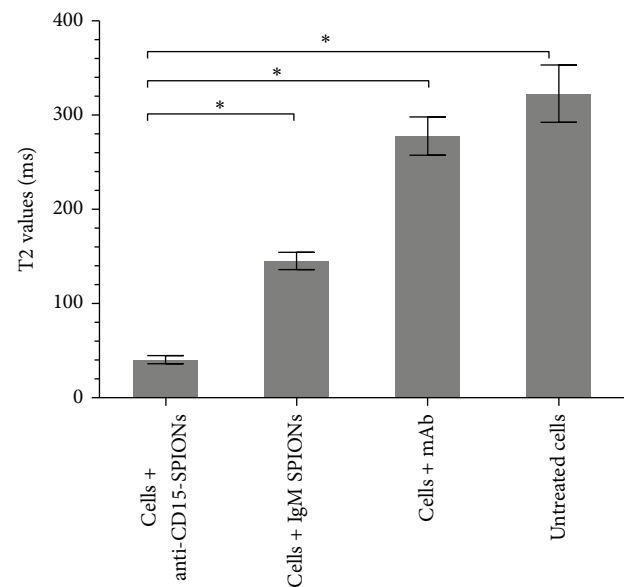


**FIGURE 5:** Graphs show T2 values of cell binding. T2 values of cells incubated with anti-CD15-SPIONs were lower than control cells.  
\* $P < 0.05$ .

#### 4. Discussion

Our study results demonstrated that anti-CD15 antibody-conjugated SPIONs delivered by intraventricular injection could specifically accumulate around a subpopulation of NSCs with a CD15 phenotype in the SVZ and RMS of adult rodent brains. Upon this targeted binding, the *in vivo* distribution and location of NSCs could be readily visualized on MR imaging. The targeted imaging of endogenous NSCs could be achieved rapidly 1 day after delivery and longitudinally persists for at least 1 week in the same living animals.

SVZ is a continual germinal zone surrounding the ventricles, which expands prominently during the latter third trimester of prenatal period and remains constant thereafter throughout the mammalian life. It is the largest source of NSCs and transit-amplifying progenitor cells that can generate progeny during mammalian forebrain development [27, 28]. Enormous progress has been made in recent decades in uncovering the contributions of NSCs in SVZ to normal brain development. It is becoming increasingly imperative to investigate a tool with the ability to identify and track NSCs *in vivo*, which could be greatly helpful for the follow-up of deviating NSC migration patterns and designing therapeutic interventions for exploration of their curative potential.

However, endogenous NSCs are a rare cell population in adult mammalian brains, and little is known about their unique biological characteristics. Genes expressed by adult neural stem cells include Nestin, Musashi, Notch1, and GFAP, but other neural cell types also express these. Moreover, these markers are intracellular. The nonspecific expression and intracellular location limited their usefulness for stem cell positive identification. A more generally useful marker would be surface molecule allowing stem cell localization

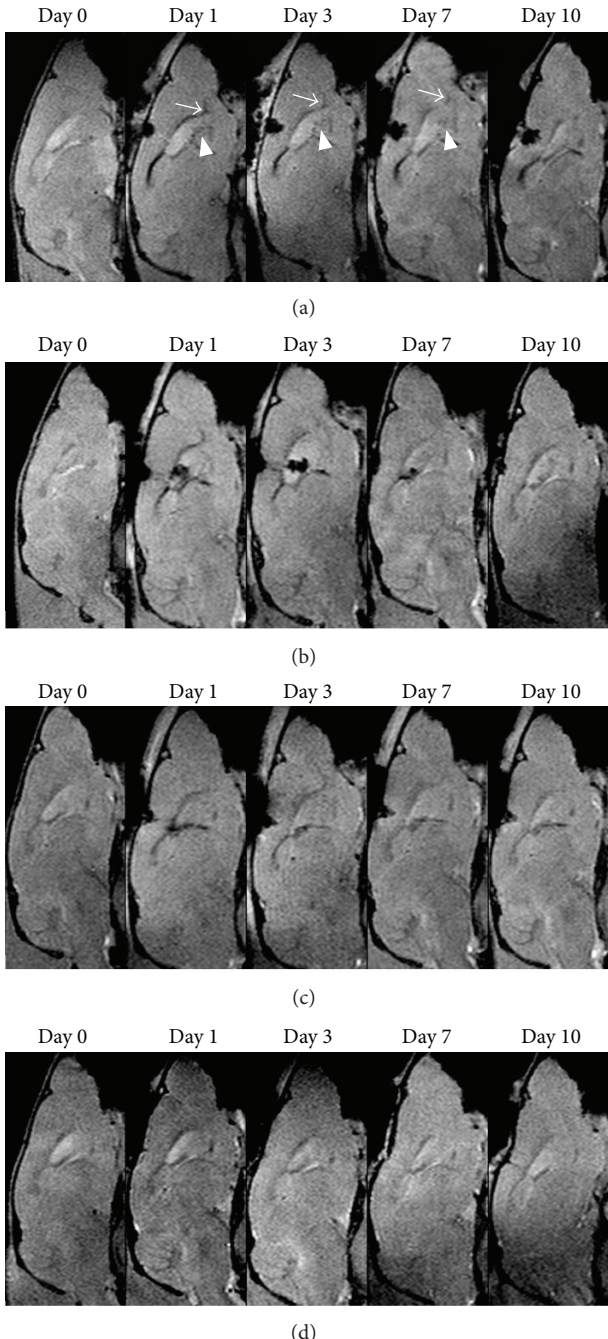


**FIGURE 6:** In vivo MR imaging of endogenous NSCs. Serial sagittal T2\*-weighted images showed that linear (arrows) and spotty hypointense signal (arrowheads) appear in the beginning of RMS and SVZ and in animals injected with anti-CD15-SPIONs (a); these hypointense signal patterns persist to 3 days after injection and are almost invisible by 7 days and disappear by 10 days after injection. No such developing signal intensity is found in the SVZ and RMS in animals injected with nontargeted SPIONs (b) or mAb (c) or PBS (d) alone.

and clarification from other neural cells. Recently, LeX/SSEA-1/CD15 was indicated as a specific gene product that is exclusively expressed on the surface of distinct pools of

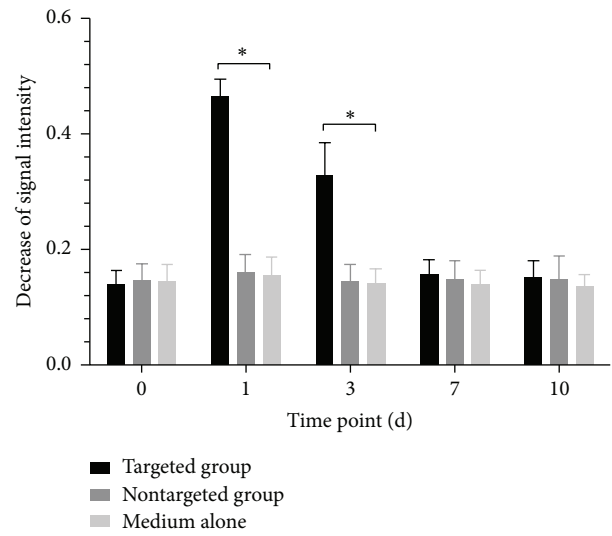


**FIGURE 7:** Graphs show the time course of T2\* signal intensity change of RMS. \* $P < 0.05$  compared to controls.

adult NSCs and is shed in the microenvironment [23]. This characterization of LeX expression by adult CNS stem cells aids in vivo identification of these important cells. In this study, SVZ cells sorted by anti-CD15-SPIONs demonstrated the ability to self-renew and generate neurospheres and could be differentiated to three different neural cell types. This further corroborates their potential role of a useful cell type marker for in vivo identification of adult NSCs.

Previous animal studies demonstrated that direct injection of MPIOs or SPIONs with canonic reagents into the lateral ventricles could be used to label NSCs within SVZ. The iron oxide particles were endocytosed by cells within SVZ and then could be distinguished from the surrounding tissue as they appear as hypointense spots on T2\*-weighted MR images. By virtue of the migrating nature of NSCs along the RMS to the olfactory bulb, the NSC dynamics could be followed in vivo by MR imaging [18–23]. However, it was shown that the uptake of MPIOs or iron oxide nanoparticles by the precursors in the SVZ is small (~30%) and 4% iron oxide particles were likely engulfed by ependymal cells [19]. There is also a possibility that MPIOs could travel along the RMS and then be endocytosed locally by other cells. Moreover, a varied, prolonged period of time was required for in vivo tracking NSCs by using MPIO or cationic protein-complexed SPIONs, for example, 2 weeks to 5 weeks were needed for tracking NSCs in adult mature brain [19–22] and 1 week to 2 weeks were required for tracking NSCs in neonatal brain [23]. On the other hand, the intracellular and nonspecific retention of iron oxide particles within cells could persist for a long period of time, even until 8 weeks after injection [18]. Such prolonged retaining of MPIOs or SPIONs could probably cause detrimental effects on the biological behavior of labeled cells, since MPIOs while being inert inside a cell could have significant impact on cellular processes due to their large particle size and styrene/divinylbenzene coating [29].

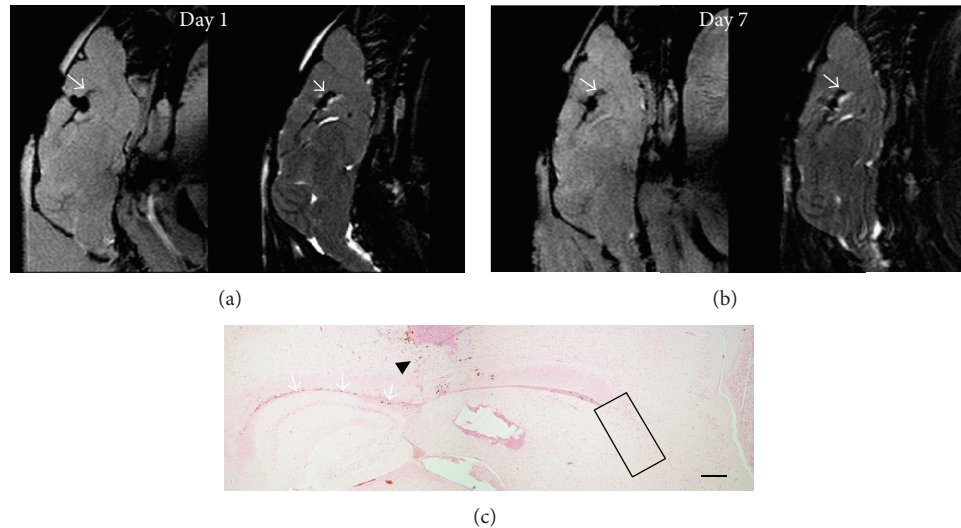


FIGURE 8: Anti-CD15-SPIONs injected into the corpus callosum. After injection of anti-CD15-SPIONs into the corpus callosum, the corpus callosum (arrows) shows decreased signal intensity on T2\*-weighted (a) and T2-weighted images (b), which was retained until 7 days after injection. No decreased signal intensity appears in the RMS or SVZ. Prussian blue staining reveals that there were positive SPIONs in the needle track (black arrowhead) and the corpus callosum (arrows), while no positive SPIONs are present in the SVZ and RMS (black rectangle). Bar = 200  $\mu$ m.

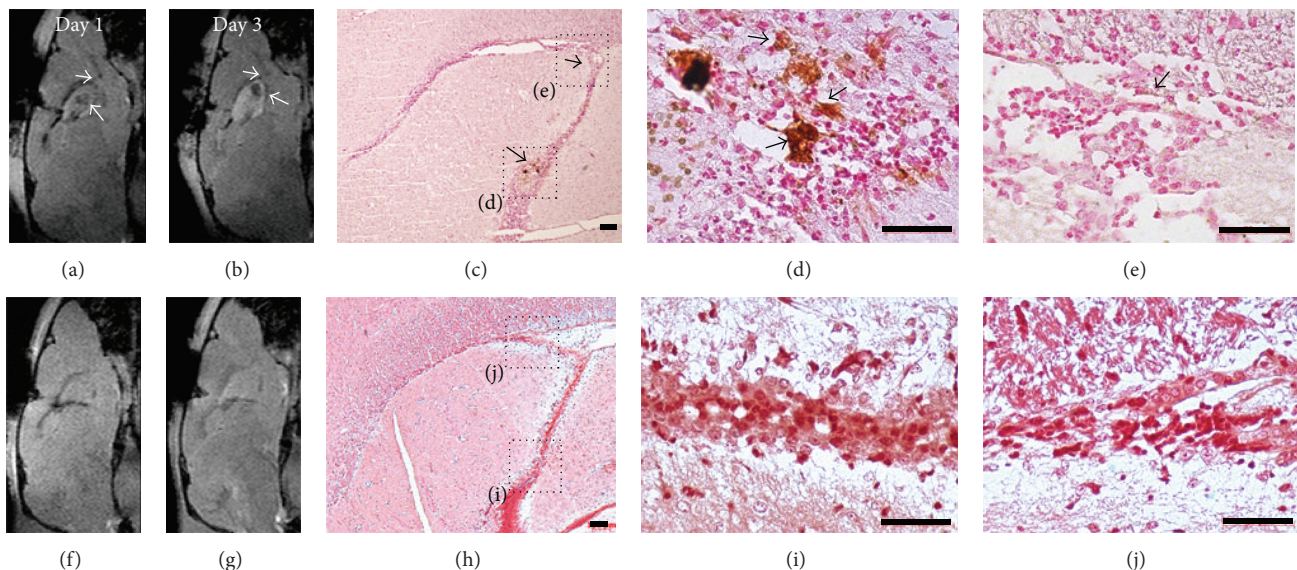


FIGURE 9: Histologic assessment of the distribution of SPIONs. At 1 day and 3 days after injection, T2\*-weighted images show hypointense signal in the SVZ and the beginning of RMS (arrows) in an animal injected with anti-CD15-SPIONs ((a), (b)). The corresponding DAB-enhanced Prussian blue staining reveals that anti-CD15-SPIONs are localized around cells and extracellular matrix (arrows) within SVZ ((c), (d)) and RMS (e) at 3 days after injection, which is well matched with MRI findings. In an animal that received nontargeted SPION injection, no hypointense signal is present in the SVZ and RMS ((f), (g)). DAB-enhanced Prussian blue staining reveals that no iron oxide nanoparticles were found in the SVZ or RMS. Bars in (c) and (h) equal 100  $\mu$ m; bars in (d), (e), (i), and (j) equal 50  $\mu$ m.

In our study, on the basis of specific expression of CD15 antigen on the surface of distinct pools of NSCs in adult mice, a targeting SPION with anti-CD15 mAb as the ligand was used for in vivo MR imaging of the NSCs. After intraventricular delivery of anti-CD15-SPIONs, the endogenous NSCs, those residing in the SVZ and RMS in adult mouse brain, were detected as hypointense signal at a rapid time,

that is, 1 day after injection. Furthermore, the presence of iron oxide nanoparticle persisted in a relatively short period of time (7 days after injection). Histology confirmed that these nanoparticles are targeted to cell surface of CD15 positive NSCs and their extracellular environments. Together with previous observation of histologic distribution of CD15 antigen in SVZ [24], our findings suggested that targeted

MR imaging of endogenous NSCs in adult mouse brain was successfully achieved by using CD15-conjugated SPIONs.

Unlike MPIO or SPIO complex, the use of CD15-targeted SPIONs has several advantages. Since the small size of the nanoparticles and a small volume are needed, the image of entire SVZ and RMS in our study was almost free from the susceptibility artifact. Due to the specific binding between antibody and CD15 antigen, the targeting nanoparticles were only present around CD15 positive NSCs and their surrounding matrix; the resulting signal change on MR imaging is highly likely to reflect the actual change in NSCs plasticity. It has been revealed that in mice many new neurons reach the OB by two days and a majority arrives in the OB by day 6 [30]. Therefore, tracking NSC migrating patterns in such highly active state would greatly benefit from our strategy. Moreover, in comparison with internalization of larger MPIOs or SPIO complex, cellular surface binding of the biodegradable nanoparticles used in our study would be more favorable for *in vivo* cellular imaging as the intact biological behavior of cells could be less likely affected.

A number of limitations exist in the current study. First, like targeting immunotherapy and targeting imaging where an antibody ligand is coupled to targeting probe, a common problem of using CD15-targeted nanoparticles is that introduction of heterologous antibody could result in host immunological reaction. In our study, a homologous murine monoclonal antibody was conjugated to iron oxide nanoparticles with which the immunological reaction might be alleviated. With the advancement of molecular biology, use of specific single-chain Fv antibody would be potentially preferred in the future owing to the advantages such as decreased immunogenicity and favorable pharmacokinetics/biodistribution profiles [31]. The second is the lack of the immunohistological staining for several other neural cell phenotypes, such as ependymal cells, neuroblasts, oligodendrocytes, and microglia, and the absence of quantitative analysis of labeled cells. Previous study had characterized CD15 positive population in the SVZ [24]. The results had shown that there was little overlap between CD15 phenotype and other phenotypes such as GFAP,  $\beta$ -tubulin III, mCD24, and PSA-NCAM; and 4% of acutely isolated SVZ cells are CD15 positive. Third, our investigation was only performed in normal mouse brain. Future studies are needed to address the *in vivo* MR imaging of NSC migration in adult diseased brains.

In summary, our results demonstrated that *in vivo* targeted MR imaging of endogenous NSCs in adult mouse brains could be successfully achieved by intraventricular delivery of anti-CD15 mAb-conjugated SPIONs. Use of these nanoparticles as the molecular probe could allow a rapid *in vivo* tracking of adult NSCs with MR imaging. Such *in vivo* targeted MR imaging of the NSCs can be used to reflect the neurogenesis size of the SVZ in the healthy brain and potentially the time course of activation of the NSCs within the SVZ in diseased brain, resulting in improved understanding of neurogenesis in normal mammalian brains and its alterations during diseases. This direct observation of NSCs has potential as an additional diagnostic and prognostic criterion in brain diseases, as the neurogenesis in the SVZ

might indicate the recovery phase and the stage and grade of the disease.

## Conflict of Interests

The authors declare that there is no conflict of interests regarding the publication of this paper.

## Authors' Contribution

Xiao-Mei Zhong and Fang Zhang contribute equally to this work.

## Acknowledgments

This work is supported by the National Natural Science Foundation of China (30870691, 81371607) and the Guangdong Natural Science Foundation (9151008901000001, 2014A030312018).

## References

- [1] I. Kazanis, "The subependymal zone neurogenic niche: a beating heart in the centre of the brain," *Brain*, vol. 132, no. 11, pp. 2909–2921, 2009.
- [2] R. L. Zhang, Z. G. Zhang, C. Roberts et al., "Lengthening the G<sub>1</sub> phase of neural progenitor cells is concurrent with an increase of symmetric neuron generating division after stroke," *Journal of Cerebral Blood Flow and Metabolism*, vol. 28, no. 3, pp. 602–611, 2008.
- [3] S. Ramaswamy, G. E. Goings, K. E. Soderstrom, F. G. Szele, and D. A. Kozlowski, "Cellular proliferation and migration following a controlled cortical impact in the mouse," *Brain Research*, vol. 1053, no. 1-2, pp. 38–53, 2005.
- [4] M. A. Curtis, P. S. Eriksson, and R. L. M. Faull, "Progenitor cells and adult neurogenesis in neurodegenerative diseases and injuries of the basal ganglia," *Clinical and Experimental Pharmacology and Physiology*, vol. 34, no. 5-6, pp. 528–532, 2007.
- [5] A. Arvidsson, T. Collin, D. Kirik, Z. Kokaia, and O. Lindvall, "Neuronal replacement from endogenous precursors in the adult brain after stroke," *Nature Medicine*, vol. 8, no. 9, pp. 963–970, 2002.
- [6] N. Picard-Riera, L. Decker, C. Delarasse et al., "Experimental autoimmune encephalomyelitis mobilizes neural progenitors from the subventricular zone to undergo oligodendrogenesis in adult mice," *Proceedings of the National Academy of Sciences of the United States of America*, vol. 99, no. 20, pp. 13211–13216, 2002.
- [7] G. U. Höglunger, P. Rizk, M. P. Muriel et al., "Dopamine depletion impairs precursor cell proliferation in Parkinson disease," *Nature Neuroscience*, vol. 7, no. 7, pp. 726–735, 2004.
- [8] G. A. Elder, R. De Gasperi, and M. A. Gama Sosa, "Research update: neurogenesis in adult brain and neuropsychiatric disorders," *Mount Sinai Journal of Medicine*, vol. 73, no. 7, pp. 931–940, 2006.
- [9] A. Consiglio, A. Gritti, D. Dolcetta et al., "Robust *in vivo* gene transfer into adult mammalian neural stem cells by lentiviral vectors," *Proceedings of the National Academy of Sciences of the United States of America*, vol. 101, no. 41, pp. 14835–14840, 2004.

- [10] M. Cayre, M. Bancila, I. Virard, A. Borges, and P. Durbec, “Migrating and myelinating potential of subventricular zone neural progenitor cells in white matter tracts of the adult rodent brain,” *Molecular and Cellular Neuroscience*, vol. 31, no. 4, pp. 748–758, 2006.
- [11] C. Lois and A. Alvarez-Buylla, “Long-distance neuronal migration in the adult mammalian brain,” *Science*, vol. 264, no. 5162, pp. 1145–1148, 1994.
- [12] S. O. Suzuki and J. E. Goldman, “Multiple cell populations in the early postnatal subventricular zone take distinct migratory pathways: a dynamic study of glial and neuronal progenitor migration,” *Journal of Neuroscience*, vol. 23, no. 10, pp. 4240–4250, 2003.
- [13] P. Taupin, “Protocols for studying adult neurogenesis: insights and recent developments,” *Regenerative Medicine*, vol. 2, no. 1, pp. 51–62, 2007.
- [14] A. D. R. Garcia, N. B. Doan, T. Imura, T. G. Bush, and M. V. Sofroniew, “GFAP-expressing progenitors are the principal source of constitutive neurogenesis in adult mouse forebrain,” *Nature Neuroscience*, vol. 7, no. 11, pp. 1233–1241, 2004.
- [15] L.-R. Zhao and S. C. Nam, “Multiphoton microscope imaging: the behavior of neural progenitor cells in the rostral migratory stream,” *Neuroscience Letters*, vol. 425, no. 2, pp. 83–88, 2007.
- [16] L. N. Manganas, X. Zhang, Y. Li et al., “Magnetic resonance spectroscopy identifies neural progenitor cells in the live human brain,” *Science*, vol. 318, no. 5852, pp. 980–985, 2007.
- [17] P. Ramm, S. Couillard-Despres, S. Plötz et al., “A Nuclear magnetic resonance biomarker for neural progenitor cells: is it all neurogenesis?” *Stem Cells*, vol. 27, no. 2, pp. 420–423, 2009.
- [18] E. M. Shapiro, O. Gonzalez-Perez, J. M. García-Verdugo, A. Alvarez-Buylla, and A. P. Koretsky, “Magnetic resonance imaging of the migration of neuronal precursors generated in the adult rodent brain,” *NeuroImage*, vol. 32, no. 3, pp. 1150–1157, 2006.
- [19] J. P. Sumner, E. M. Shapiro, D. Maric, R. Conroy, and A. P. Koretsky, “In vivo labeling of adult neural progenitors for MRI with micron sized particles of iron oxide: quantification of labeled cell phenotype,” *NeuroImage*, vol. 44, no. 3, pp. 671–678, 2009.
- [20] R. Vreys, G. V. Velde, O. Krylychkin et al., “MRI visualization of endogenous neural progenitor cell migration along the RMS in the adult mouse brain: validation of various MPIO labeling strategies,” *NeuroImage*, vol. 49, no. 3, pp. 2094–2103, 2010.
- [21] R. A. Panizzo, P. G. Kyrtatos, A. N. Price, D. G. Gadian, P. Ferretti, and M. F. Lythgoe, “In vivo magnetic resonance imaging of endogenous neuroblasts labelled with a ferumoxide-polycation complex,” *NeuroImage*, vol. 44, no. 4, pp. 1239–1246, 2009.
- [22] B. J. Nieman, J. Y. Shyu, J. J. Rodriguez, A. D. Garcia, A. L. Joyner, and D. H. Turnbull, “In vivo MRI of neural cell migration dynamics in the mouse brain,” *NeuroImage*, vol. 50, no. 2, pp. 456–464, 2010.
- [23] J. Yang, J. Liu, G. Niu et al., “In vivo MRI of endogenous stem/progenitor cell migration from subventricular zone in normal and injured developing brains,” *NeuroImage*, vol. 48, no. 2, pp. 319–328, 2009.
- [24] A. Capela and S. Temple, “LeX/ssea-1 is expressed by adult mouse CNS stem cells, identifying them as nonependymal,” *Neuron*, vol. 35, no. 5, pp. 865–875, 2002.
- [25] G. Baio, M. Fabbri, S. Salvi et al., “Two-step in vivo tumor targeting by biotin-conjugated antibodies and superparamagnetic nanoparticles assessed by magnetic resonance imaging at 1.5 T,” *Molecular Imaging and Biology*, vol. 12, no. 3, pp. 305–315, 2010.
- [26] J. J. E. In den Kleef and J. J. M. Cuppen, “RLSQ:  $T_1$ ,  $T_2$ , and  $\rho$  calculations, combining ratios and least squares,” *Magnetic Resonance in Medicine*, vol. 5, no. 6, pp. 513–524, 1987.
- [27] C. Y. Brazel, M. J. Romanko, R. P. Rothstein, and S. W. Levison, “Roles of the mammalian subventricular zone in brain development,” *Progress in Neurobiology*, vol. 69, no. 1, pp. 49–69, 2003.
- [28] C. A. G. Marshall, S. O. Suzuki, and J. E. Goldman, “Gliogenic and neurogenic progenitors of the subventricular zone: who are they, where did they come from, and where are they going?” *Glia*, vol. 43, no. 1, pp. 52–61, 2003.
- [29] M. Modo, M. Hoehn, and J. W. M. Bulte, “Cellular MR imaging,” *Molecular Imaging*, vol. 4, no. 3, pp. 143–164, 2005.
- [30] A. Saghatelian, A. de Chevigny, M. Schachner, and P.-M. Lledo, “Tenascin-R mediates activity-dependent recruitment of neuroblasts in the adult mouse forebrain,” *Nature Neuroscience*, vol. 7, no. 4, pp. 347–356, 2004.
- [31] W. W. Cheng and T. M. Allen, “The use of single chain Fv as targeting agents for immunoliposomes: an update on immunoliposomal drugs for cancer treatment,” *Expert Opinion on Drug Delivery*, vol. 7, no. 4, pp. 461–478, 2010.

## Research Article

# Calreticulin Binds to Fas Ligand and Inhibits Neuronal Cell Apoptosis Induced by Ischemia-Reperfusion Injury

Beilei Chen,<sup>1,2</sup> Zhengzheng Wu,<sup>1</sup> Jun Xu,<sup>2</sup> and Yun Xu<sup>1</sup>

<sup>1</sup>Department of Neurology, Drum Tower Hospital of Nanjing Medical University, Nanjing 210008, China

<sup>2</sup>Department of Neurology, Northern Jiangsu Province Hospital, Yangzhou 225009, China

Correspondence should be addressed to Yun Xu; xuyun20042001@aliyun.com

Received 20 April 2015; Accepted 7 July 2015

Academic Editor: Xingmei Zhang

Copyright © 2015 Beilei Chen et al. This is an open access article distributed under the Creative Commons Attribution License, which permits unrestricted use, distribution, and reproduction in any medium, provided the original work is properly cited.

**Background.** Calreticulin (CRT) can bind to Fas ligand (FasL) and inhibit Fas/FasL-mediated apoptosis of Jurkat T cells. However, its effect on neuronal cell apoptosis has not been investigated. **Purpose.** We aimed to evaluate the neuroprotective effect of CRT following ischemia-reperfusion injury (IRI). **Methods.** Mice underwent middle cerebral artery occlusion (MCAO) and SH-SY5Y cells subjected to oxygen glucose deprivation (OGD) were used as models for IRI. The CRT protein level was detected by Western blotting, and mRNA expression of CRT, caspase-3, and caspase-8 was measured by real-time PCR. Immunofluorescence was used to assess the localization of CRT and FasL. The interaction of CRT with FasL was verified by coimmunoprecipitation. SH-SY5Y cell viability was determined by MTT assay, and cell apoptosis was assessed by flow cytometry. The measurement of caspase-8 and caspase-3 activity was carried out using caspase activity assay kits. **Results.** After IRI, CRT was upregulated on the neuron surface and bound to FasL, leading to increased viability of OGD-exposed SH-SY5Y cells and decreased activity of caspase-8 and caspase-3. **Conclusions.** This study for the first time revealed that increased CRT inhibited Fas/FasL-mediated neuronal cell apoptosis during the early stage of ischemic stroke, suggesting it to be a potential protector activated soon after IRI.

## 1. Introduction

Ischemic stroke, with high morbidity and mortality, is the most common type of stroke accounting for more than 80% of all stroke cases. It can affect people of all ages. Previous studies have shown both endoplasmic reticulum (ER) stress and neuronal apoptosis are involved in the progression of ischemic stroke [1, 2].

The ER is an organelle responsible for protein synthesis and folding. ER stress occurs under some pathological conditions, such as ischemic stroke [1]. Calreticulin (CRT) is a conserved 46-kDa  $\text{Ca}^{2+}$  binding protein expressed virtually in all nucleated cells and is located preferentially in the ER [3]. As a chaperone molecular and a modulator of the  $\text{Ca}^{2+}$  balance, CRT resides mostly in the lumen of the ER, is upregulated during ER stress, and transferred to outside the cytomembrane [4].

Fas (also known as CD95 or APO-1) is a member of the tumor necrosis factor (TNF) receptor family and promotes

apoptosis through a well-established pathway. Activation of Fas can recruit and activate caspase-8, a cysteine protease, which then induces cleavage of other protein substrates, such as caspase-3, contributing to neuronal apoptosis [5, 6]. On the cell surface, CRT has been found to bind to FasL (Fas ligand), the ligand of Fas [7], and inhibit Fas/FasL-mediated apoptosis of Jurkat T cells [4, 8]. Given that the Fas/FasL pathway plays an important role in neuronal apoptosis during ischemic stroke [2], we speculated that if CRT expression is increased in the brain after ischemia-reperfusion injury (IRI), CRT may bind to FasL and interfere with Fas/FasL complexation, thereby protecting neurons from apoptosis and relieving ischemia-related damage.

To date, the effect of CRT on neuronal apoptosis has not been investigated. In this study, we observed upregulated CRT expression after ischemia and interaction between CRT and FasL, which led to reduced neuronal cell death, suggesting a possible novel approach to protecting the brain from IRI injury via based on CRT.

## 2. Materials and Methods

**2.1. Experiment Animals.** Kunming mice (10 per group, 25–30 g, 4 weeks old, male : female = 1:1) were obtained from the Experimental Animal Center of Nanjing University Medical School, Nanjing, China. Fifty mice were divided into the following five groups ( $n = 10$  for each group): sham-operated group and four groups (3 h-MCAO, 6 h-MCAO, 12 h-MCAO, and 24 h-MCAO) in which middle cerebral artery occlusion (MCAO) was performed and mice were killed at 3, 6, 12, or 24 h after reperfusion, respectively. A random block design was carried out using SAS software. The investigators were masked to the group assignments. The protocols for animal experiments were approved by the Animal Care and Use Committee of Nanjing University, Nanjing, China.

**2.2. MCAO Model.** The MCAO model was generated as previously described by Zhang et al. [9]. Briefly, intraperitoneal injection of ketamine (100 mg/mL) and xylazine (20 mg/kg) mixture (1:1) (1 mL/kg) was applied to anesthetize the mice. Mice were then subjected to MCAO using 6/0 monofilament nylon sutures with heat-rounded tips inserted through the internal carotid artery (ICA) into the beginning of the middle cerebral artery (MCA). After 2 h of occlusion of the MCA, the filament was withdrawn for blood reperfusion. Three, six, twelve, or twenty-four hours later, the mice were killed and the brain tissues were collected for real-time polymerase chain reaction (PCR) analysis, Western blotting, and immunofluorescence staining. The sham-operated group was treated using the same procedures as described above except MCAO. The mortality of MCAO among the model mice was approximately 10%.

**2.3. SY5Y Cell Culture and Oxygen Glucose Deprivation (OGD).** SH-SY5Y cells (a neuroblastoma cell line) were provided by the American Type Culture Collection (ATCC) and cultured in Dulbecco's Modified Eagle's Medium (DMEM) containing 10% heat-inactivated fetal bovine serum (FBS, Gibco) with 2 mM glutamine, 100 U/mL penicillin, and 100  $\mu$ g/mL streptomycin. Cells were maintained at 37°C in a humidified incubator with 5% CO<sub>2</sub>. The *in vitro* OGD model was established as described previously by Tarr et al. [4]. Briefly, an oxygen-depleted, glucose-free medium was applied to SH-SY5Y cells before incubation in a hypoxic chamber (5% CO<sub>2</sub>/95% N<sub>2</sub>) for 15 min. The chamber was sealed, and incubation at 37°C continued for 8 h. After OGD, the cells were returned to normal medium with the presence of different concentrations of CRT (Abcam, ab91577, UK) and incubated for use in subsequent experiments.

**2.4. Real-Time PCR.** Real-time PCR was performed as described previously [10]. Trizol reagent (Takara, Dalian, China) was used to extract total RNA, and a PrimeScript RT reagent kit (Takara) for Quantitative PCR (ABI 7500, Foster City, CA, USA) was used to reverse-transcribe the total RNA into cDNA with the supplement of a fluorescent dye (SYBR Green I; Takara). The primers were as follows:

CRT: forward, 5'-TGA TCC CAC AGA CTC CAA GC-3'; reverse, 5'-TCAGCGTATGCCTCATCGTT-3'; caspase-3: forward, 5'-TGT CAT CTC GCT CTG GTA CG3'; reverse, 5'-TCC CAT AAA TGA CCC CTT CA-3'; caspase-8: forward, 5'-GGC CTC CAT CTA TGA CCT GA-3'; reverse, 5'-TGT GGT TCT GTT GCT CGA AG-3'.

**2.5. Western Blotting.** Western blotting was carried out as described previously [11]. A nuclear and cytoplasmic protein extraction kit (Beyotime Institute of Biotechnology, Shanghai, China) was used to prepare cytoplasmic and nuclear proteins. Equal amounts of sample protein were separated by sodium dodecyl sulfate- (SDS-) polyacrylamide gel electrophoresis (PAGE) before blotting onto polyvinylidene fluoride membranes. Membranes were incubated with anti-CRT antibody (1:1000, Abcam, ab22683) at 4°C overnight. The protein was detected using horseradish peroxidase-conjugated anti-mouse or anti-rabbit secondary antibodies and visualized using enhanced chemiluminescence detection reagents (Bioworld, Nanjing, China). The intensity of blots was quantified using ImageJ software (National Institutes of Health, Bethesda, MD, USA).

**2.6. Coimmunoprecipitation (co-IP).** For co-IP, 500  $\mu$ L PBS with protease inhibitor (1:100, Sigma-Aldrich, St. Louis, MO, USA) was used to dilute 500  $\mu$ g protein. The solution was preincubated with anti-CRT antibody (12.5  $\mu$ g/mL, Abcam, ab22683) or anti-Fas antibody (1  $\mu$ g/mL, Santa Cruz Biotechnology Inc., sc-21730, Santa Cruz, CA, USA) at 4°C overnight on a rotating shaker. Additional rotation for 2 h was continued after addition of 20  $\mu$ L protein A/G-Sepharose bead slurry (Millipore, Billerica, MA, USA) to the mixture. Ice-cold cell lysis buffer was used to wash the slurry three times. Proteins were eluted with SDS sample buffer and boiled for 5 min. Supernatant was subjected to SDS-PAGE and Western blotting using anti-FasL antibody (1:200, Santa Cruz Biotechnology, Inc., sc-834).

**2.7. Immunofluorescence.** At 3 h after reperfusion, the SH-SY5Y cells were fixed in 4% paraformaldehyde for 20 min at room temperature and then seeded on cover slips. Monoclonal rabbit anti-CRT antibody (1:500, Bioss, bs-5913R, Beijing, China) and monoclonal mouse anti-FasL antibody (1:200, Abcam, ab81196) were applied to the cells at 4°C overnight. Then they were incubated with secondary antibody (1:200, Invitrogen, Carlsbad, CA, USA) for 45 min at room temperature. The nuclei of the cells were stained using a DAPI kit (KeyGen Biotech, Nanjing, China). Fluorescent images were taken by immunofluorescent microscopy (Olympus, Tokyo, Japan) and laser scanning confocal microscopy (Olympus).

**2.8. MTT and Caspase-8 and Caspase-3 Activity Assays.** The viability of OGD SH-SY5Y cells was assessed using the conventional MTT assay as previously described [12]. The caspase-8 and caspase-3 activities of OGD-exposed SH-SY5Y cells were assessed using caspase activity assay kits

(Beyotime Institute of Biotechnology, China) according to the manufacturer's protocol.

**2.9. Apoptosis Assay by Flow Cytometry.** Apoptosis among OGD-exposed cells was assessed using an Annexin V-FITC apoptosis detection kit (KeyGen Biotech, China). Cells ( $1 \times 10^6/\text{mL}$ ) were rinsed twice with PBS and then resuspended in binding buffer containing  $5 \mu\text{L}$  Annexin V-fluorescein isothiocyanate (FITC) and  $5 \mu\text{L}$  propidium iodide (PI). After incubation at room temperature in the dark for 15 min, the cells were analyzed by flow cytometry (FACS Cantoll, Becton Dickinson and Co., Franklin Lakes, NJ, USA) using Diva software.

**2.10. Statistical Analysis.** All data are expressed as mean  $\pm$  standard error of the mean (SEM). Differences between two groups were determined by independent samples *t*-tests. All statistical analyses were conducted using Statistical Product and Service Solutions 19.0 software (SPSS, Inc., Chicago, IL, USA). A difference was considered statistically significant at  $P < 0.05$ .

### 3. Results

**3.1. Increase in CRT Expression in the Cortices of MCAO Mice at 3 h after Reperfusion, Earlier Than the Increase in Caspase-8 and Caspase-3 mRNA Expression.** To investigate whether and when CRT expression was increased in the cortices of MCAO mice, real-time PCR and Western blotting were used to detect the mRNA and protein levels of CRT, respectively. Real-time PCR showed that CRT mRNA expression was significantly increased at 3, 6, 12, and 24 h after reperfusion, quickly reaching a peak at 3 h after reperfusion and remaining at high levels for the next 21 hours ( $200.0 \pm 15.63\%$  at 3 h,  $176.4 \pm 8.88\%$  at 6 h,  $142.7 \pm 13.66\%$  at 12 h, and  $136.8 \pm 14.74\%$  at 24 h) (Figure 1(a)). In line with the RT-PCR results, Western blotting showed high CRT levels from 3 h to 24 h after reperfusion with expression at 3 h being the highest (Figures 1(b1) and 1(b2)). We also used RT-PCR to explore when the expression of caspase-8 and caspase-3 was elevated. The increase in caspase-8 mRNA expression became significant 6 h after reperfusion and reached peak levels at 24 h ( $194.5 \pm 18.85\%$  at 6 h,  $317.5 \pm 34.41\%$  at 12 h, and  $353.4 \pm 39.29\%$  at 24 h, Figure 1(c)). Similarly, a significant increase in caspase-3 mRNA was detected 12 h and 24 h after reperfusion ( $193.8 \pm 26.42\%$  at 12 h and  $302.2 \pm 28.18\%$  at 24 h, Figure 1(d)).

**3.2. CRT Binds to FasL on the Neuronal Cell Surface after Ischemia.** To examine the expression of CRT and its location in the cortex of ischemic mice, immunofluorescence was used to stain brain slices from sham and MCAO mice. Little CRT was detected in the cortices of sham mice, whereas a large amount was detected in those mice subjected to MCAO and killed at 3 h after reperfusion. FasL was detected in the brain of both sham and MCAO mice (Figure 2(a)). To further validate whether CRT was expressed on the neuronal cell surface, laser scanning confocal microscope was used to

detect the quantity and location of CRT in OGD-exposed SH-SY5Y cells. CRT was barely visible in normal SH-SY5Y cells but became obvious in the cytoplasm and plasma membrane of the OGD-exposed SH-SY5Y cells 3 h after reperfusion and colocalized on the cell surface with FasL (Figure 2(b)). To verify that CRT can bind to FasL, protein was extracted from the cortices of sham mice and 3 h-MCAO mice. Co-IP was performed, and the results demonstrated that the two proteins can interact with each other in both groups; however, more protein complexes were observed in MCAO mice (Figures 2(c1) and 2(c2)). To confirm that CRT could compete with Fas and prohibit Fas/FasL combination, protein was extracted from SH-SY5Y cells and co-IP was performed. It was found that little Fas formed a complex with FasL in normal SH-SY5Y cells; however, increased interaction was detected in OGD-exposed SH-SY5Y cells cultured without CRT at 3 h after reperfusion. In contrast, with the presence of 40 ng/mL CRT, the amount of Fas/FasL was remarkably lower (Figures 2(d1) and 2(d2)).

**3.3. CRT Protected OGD-Exposed SH-SY5Y Cells.** To evaluate the ability of CRT to protect neurons during IRI, the SH-SY5Y cells were moved to medium containing different concentrations of CRT immediately after OGD. The MTT assay was applied to evaluate cell viability at 3, 6, 12, and 24 h after reperfusion. CRT at concentrations of 20–320 ng/mL increased the viability of OGD-exposed SH-SY5Y cells at 6 h after reperfusion from 40% (untreated control) to approximately 60% (Figure 3(a)). Thus, 40 ng/mL was used for subsequent experiments. The protective effects were obvious at 6 h after reperfusion and diminished with time ( $P = 0.0014$  at 6 h,  $P = 0.0051$  at 12 h, and  $P = 0.0393$  at 24 h, Figure 3(b)).

**3.4. CRT Protects OGD-Exposed SH-SY5Y Cells from Apoptosis and Downregulates the Activity of Caspase-8 and Caspase-3.** To determine whether CRT can protect neurons from apoptosis during ischemia, flow cytometry was used to detect the apoptosis rate and caspase activity assay kits were used to determine the activities of caspase-8 and caspase-3 at 3, 6, 12, and 24 h after reperfusion. The apoptosis rate of control SH-SY5Y cells was similar after 12 h in culture with or without 40 ng/mL CRT (untreated:  $3.47 \pm 0.26\%$ , CRT treated:  $3.46 \pm 0.24\%$ ,  $P = 0.9778$ ). However, in OGD-exposed SH-SY5Y cells, the apoptosis rate was significantly lower when the cells were treated with 40 ng/mL CRT for 12 h after reperfusion (untreated:  $19.66 \pm 1.06\%$ , CRT treated:  $14.24 \pm 1.18\%$ ,  $P = 0.0030$ ; Figures 4(a1) and 4(a2)). Compared with cells cultured without CRT, OGD-exposed SH-SY5Y cells cultured in the presence of 40 ng/mL CRT showed significantly less caspase-8 activity at 6 h (untreated:  $198.6 \pm 18.1\%$ , CRT treated:  $131.6 \pm 17.2\%$ ,  $P = 0.0153$ ) and 12 h after reperfusion (untreated:  $268.1 \pm 30.1\%$ , CRT treated:  $185.1 \pm 23.9\%$ ,  $P = 0.0443$ ). Similarly, reduced caspase-3 activity was also observed in OGD-exposed SH-SY5Y cells treated with 40 ng/mL CRT at 12 h (untreated:  $187.2 \pm 17.5\%$ , CRT treated:  $121.6 \pm 15.7\%$ ,  $P = 0.0121$ ) and 24 h after reperfusion (untreated:  $215.3 \pm 22.5\%$ , CRT treated:  $151.4 \pm 18.5\%$ ,  $P = 0.0418$ ; Figure 4(c)).

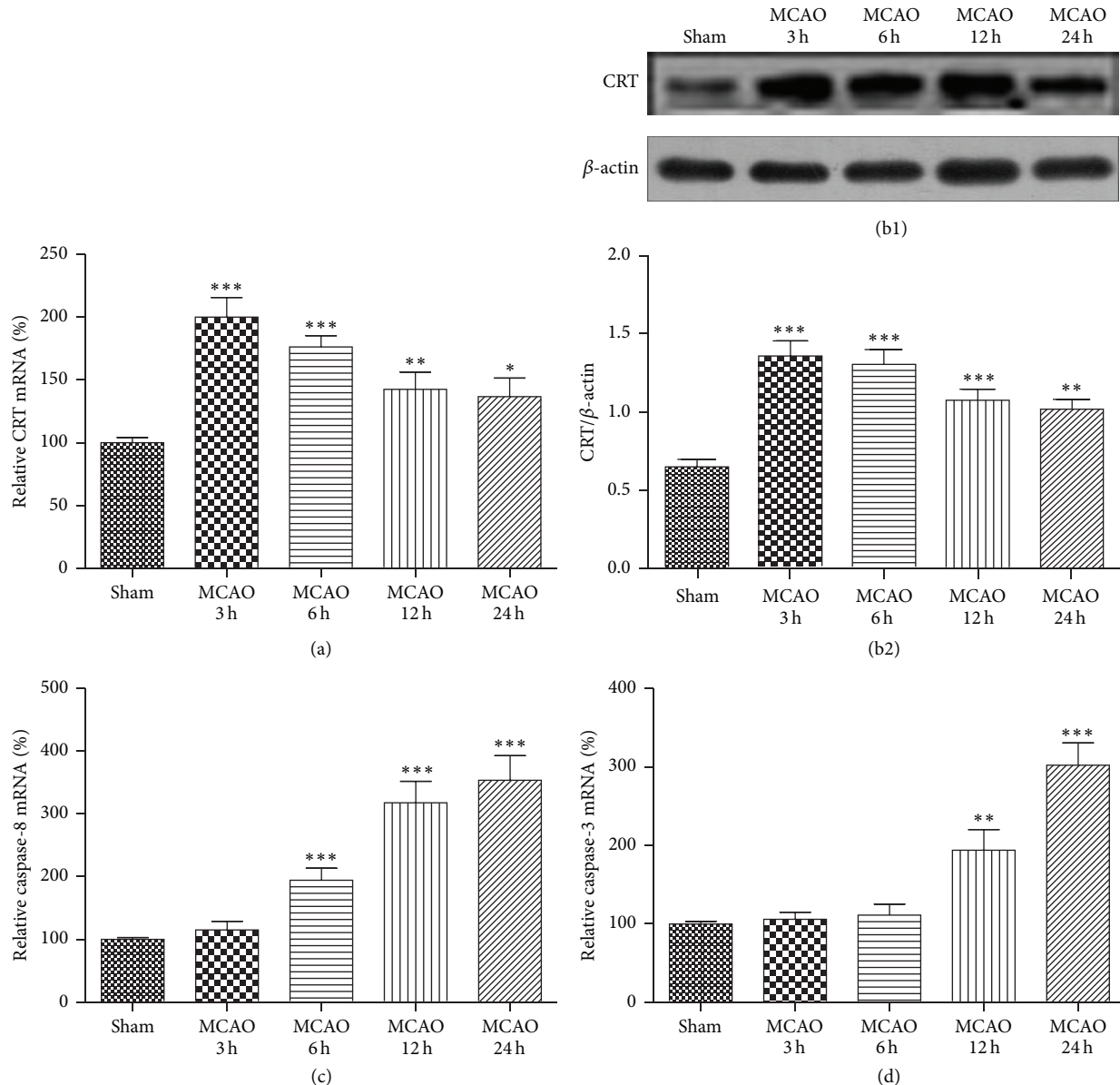


FIGURE 1: Variation in CRT protein level and mRNA expression of CRT, caspase-8, and caspase-3 in the cortices of MCAO mice. The ipsilateral cortices of the sham and MCAO mice were collected at 3, 6, 12, and 24 h after reperfusion. (a) CRT mRNA expression detected by real-time PCR and (b1, 2) CRT protein levels detected by Western blotting. (c) Caspase-8 and (d) caspase-3 mRNA detected by real-time PCR. \*  $P < 0.05$ , \*\*  $P < 0.01$ , and \*\*\*  $P < 0.0001$  versus sham.  $n = 6$  repeats.

#### 4. Discussion

This study revealed, for the first time, that CRT is upregulated during the early stage of ischemia and may interact with FasL to inhibit neuronal apoptosis. We first showed that the expression of CRT on the neuron surface was increased after IRI. As an ER chaperone protein, CRT normally resides in the ER and is increasingly expressed during ER stress, which is one of the early pathological processes in ischemic stroke. CRT barely can be detected in normal SH-SY5Y cells. However, higher levels of CRT protein and mRNA were detected in the cortices of MCAO mice compared with mice in the sham group. As a result of ER stress, highly expressed

CRT can be transferred to the plasma membrane [4] and has been demonstrated to be involved in multiple extracellular functions, such as cell attachment, immune thrombosis, and angiogenesis [13, 14].

In this study, we found that one of the major consequences following upregulated CRT expression on the cell surface could be the interruption to the formation of Fas/FasL complex due to competitive binding of CRT with FasL. The binding of CRT to FasL was verified in this study. A previous study showed that, on the T-cell surface, CRT can bind to FasL [7] and inhibit Fas/FasL-mediated apoptosis of T cells in the joints of patients with rheumatoid arthritis [8]. FASL has been reported to be expressed by both neurons and neuroglia

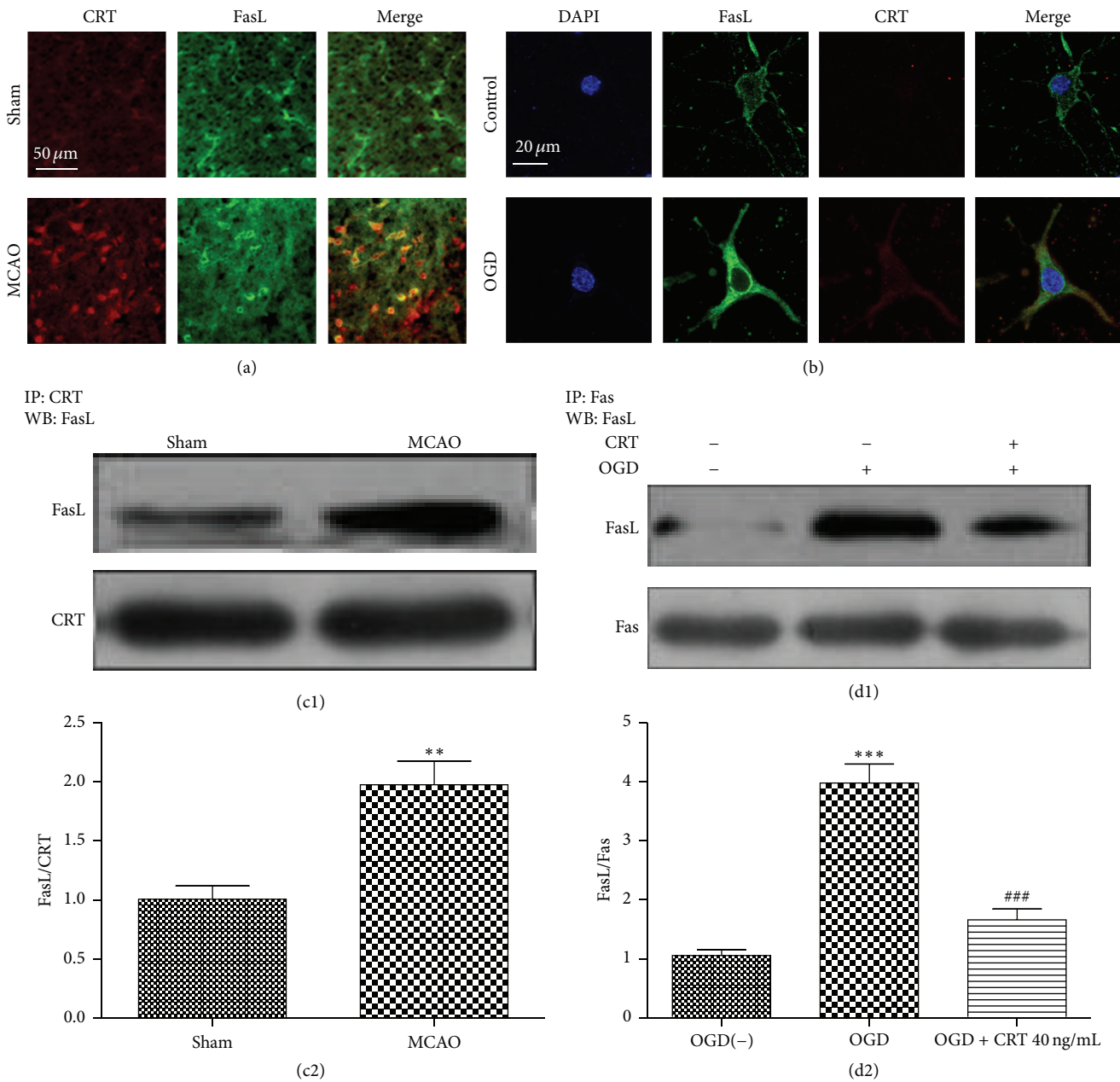


FIGURE 2: CRT binds to FasL on the surface of neurons after ischemia. (a) Immunofluorescent staining of the cortices of sham and MCAO mice. (b) Confocal microscopy images of immunostained normal SH-SY5Y cells and OGD-exposed SH-SY5Y cells at 3 h after reperfusion. (c1, 2) Co-IP of CRT and FasL in the cortices of sham and MCAO mice. (d1, 2) Co-IP of Fas and FasL in normal SH-SY5Y cells and OGD-exposed SH-SY5Y cells cultured with or without 40 ng/mL CRT. \*\* $P < 0.01$ , \*\*\* $P < 0.0001$  versus control, and ### $P < 0.0001$  versus OGD group.  $n = 6$  repeats.

[15]. It exists in two forms: a 37-kDa membrane-bound FasL (mFasL) and a 30-kDa soluble FasL (sFasL) [16]. sFasL is a cleaved and soluble form of FasL released from activated cells and is traditionally considered as a cytokine that can induce apoptosis in susceptible cells [16]. We found that, during IRI, CRT was transferred to the neuronal surface and colocalized with FasL. Furthermore, co-IP confirmed that CRT could bind to the 30-kDa sFasL. It is quite possible that upregulated CRT on the neuronal cell surface can bind to sFasL during IRI

and, therefore, prevents sFasL from activating the Fas/FasL pathway and triggering neuronal apoptosis.

It has been shown that increased surface expression of CRT is correlated with apoptosis rate. A study by Tarr et al. showed that the spontaneous apoptosis rate of Jurkat cells was about 8.5%, which is the same as the percentage of CRT-positive cells. After treatment with FasL, 24% of the Jurkat cells proceeded to undergo apoptosis, and CRT was expressed on the surface of 44% of these Jurkat cells [4].

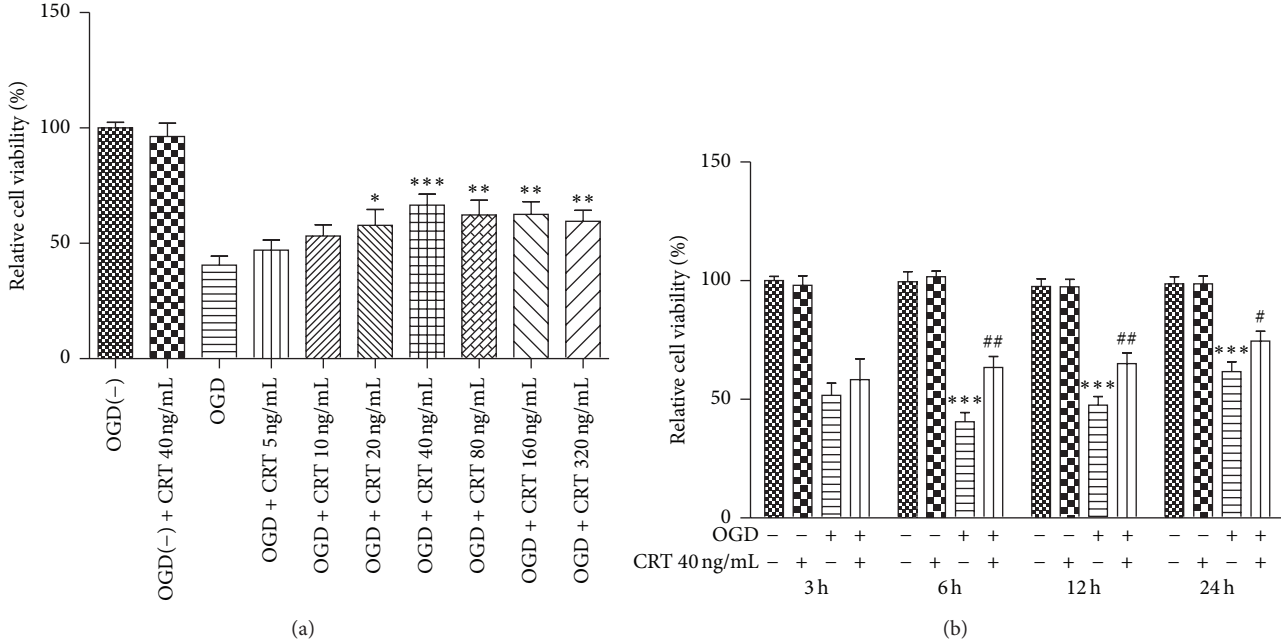


FIGURE 3: CRT protects SH-SY5Y cells during OGD. SH-SY5Y cells were cultured in media containing different concentrations of CRT after OGD. Cell viability was detected by the MTT assay. (a) Cell viability of SH-SY5Y cells cultured in different concentrations of CRT at 6 h after reperfusion and (b) cell viability of SH-SY5Y cells cultured with or without 40 ng/mL CRT at 3, 6, 12, and 24 h after reperfusion. Control in 3(a): untreated OGD-exposed SH-SY5Y cells. Control in (b): normal SH-SY5Y cells. \* $P < 0.05$ , \*\* $P < 0.01$ , and \*\*\* $P < 0.0001$  versus control and # $P < 0.05$ , ## $P < 0.01$  versus OGD group.  $n = 6$  repeats.

Our study showed that, in the cortices of MCAO mice, CRT mRNA expression was increased obviously at 3 h after reperfusion, which is earlier than the timing of the increase in mRNA expression of downstream signaling molecules of Fas/FasL-mediated apoptosis, that is, caspase-8 and caspase-3. Furthermore, CRT was also visible on the neuronal surface via immunohistofluorescent staining at 3 h after reperfusion, in line with the results of Tarr's study. The earlier increase in CRT expression makes it possible for CRT to inhibit Fas/FasL-mediated apoptosis. Our results showing that the viability of OGD-exposed SH-SY5Y cells was increased by the presence of CRT, most obviously at 6 h and 12 h after OGD, validated that CRT is a potential neuron protector induced soon after IRI. Our study also revealed that the high protein and mRNA expression of CRT faded with time, whereas the mRNA expression of caspase-8 and caspase-3 increased gradually within the first 24 h after reperfusion, suggesting that the protective effect of endogenous CRT may only exist during the early stage of IRI.

A previous study by Duus et al. demonstrated the interaction of CRT and FasL and a subsequent conformational change in FasL [7]. We hypothesize that such a change may prohibit FasL from interacting with its receptor, Fas, and, therefore, decrease the recruitment and activation of its downstream effector proteins. It was observed in our study that the apoptosis rate was lower in OGD-exposed SH-SY5Y cells cultured with the presence of 40 ng/mL CRT than in those cultured without CRT. Our study revealed that, in normal SH-SY5Y cells, the activity of caspase-8, which is first activated by Fas, was increased at 6 h after reperfusion and

maintained over the first 24 h. Then the activity of caspase-3, the protein substrate of caspase-8 and inducer of apoptosis, was elevated later than that of caspase-8. We also found that the activities of both caspase-8 and caspase-3 were lower in OGD-exposed SH-SY5Y cells cultured with 40 ng/mL CRT than in those cultured without CRT, further demonstrating the effect of CRT on impeding Fas/FasL-triggered apoptosis. It is worth noting that Fas/FasL is not the only pathway that mediates neuronal apoptosis after ischemic stroke. Many other apoptosis signals, such as TRAIL, TNF- $\alpha$ , and Bcl-2 [7, 17, 18], are also involved in neuronal apoptosis following IRI. As a result, CRT only partially inhibited apoptosis in OGD-exposed SH-SY5Y cells in our study.

FasL is involved in many mechanisms of neuronal injury besides apoptosis, such as inflammation and immunity [8, 19]. Thus, the interaction of CRT with FasL may prevent damage to neurons through some other pathways. The ER and non-ER functions of CRT, such as calcium storage and signaling, protein folding, and immunity regulation [13, 20], may also contribute to its effect on neuronal protection.

Our study is limited because SH-SY5Y cells are a neuroblastoma cell line, which differs from normal human neuronal cells in many aspects. For example, the high proliferative capability of the cell line leads to greater cell viability and a lower apoptosis rate after IRI compared to those in primary neurons. Most of our experiments were done *in vitro*, and more complicated *in vivo* experiments are needed to further elucidate the interaction between CRT and FasL. Nevertheless, our data do provide some insights into the neuroprotective effect of CRT in ischemic stroke.

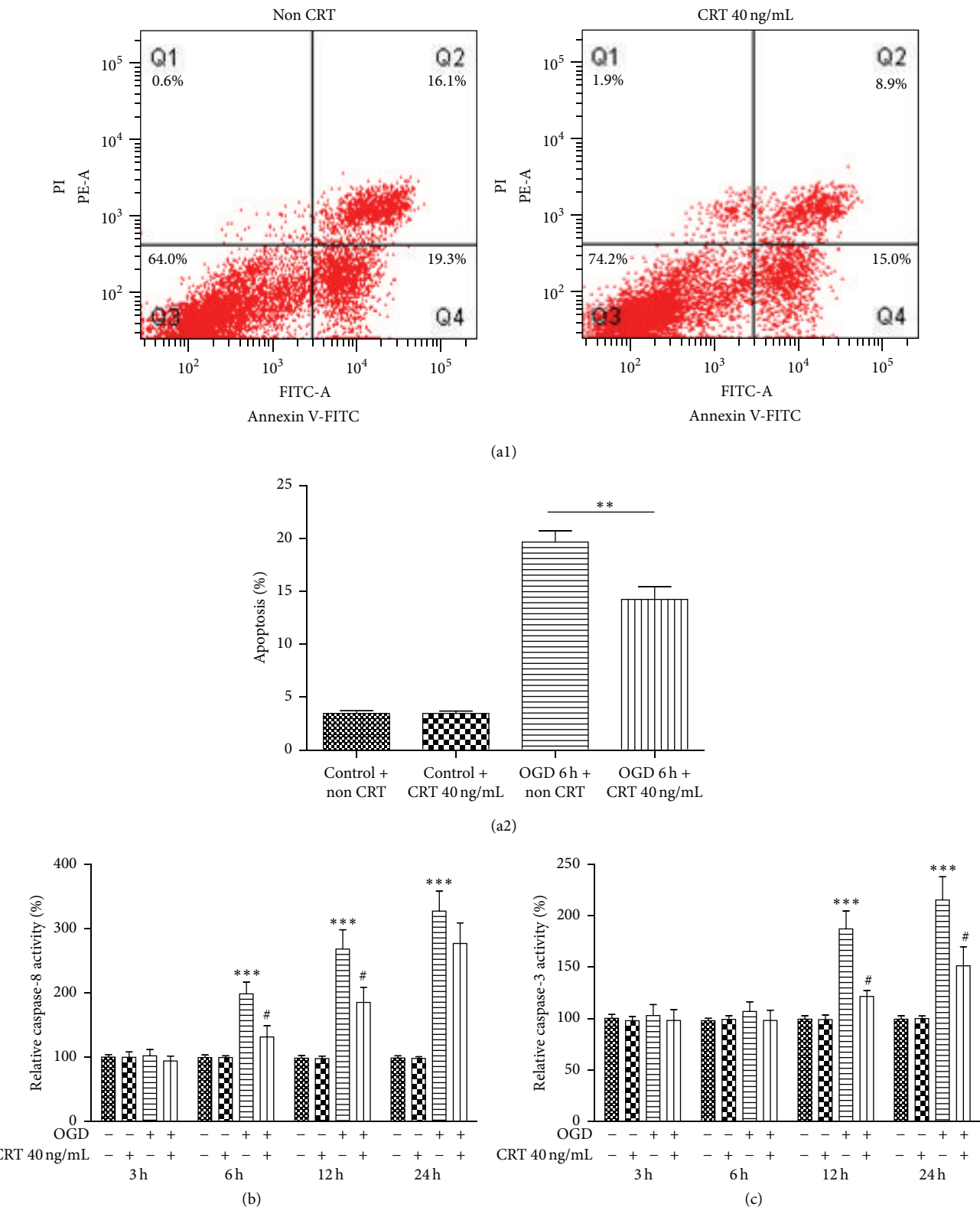


FIGURE 4: CRT prevents apoptosis among OGD-exposed SH-SY5Y cells and downregulates the activity of caspase-8 and caspase-3. SH-SY5Y cells were cultured in medium with or without 40 ng/mL CRT after OGD. (a1, 2) Apoptosis rate of OGD-exposed SH-SY5Y cells as detected by flow cytometry at 6 h after reperfusion and activity of (b) caspase-8 and (c) caspase-3 as detected using caspase activity assay kits at 3, 6, 12, and 24 h after reperfusion. Control: normal SH-SY5Y cells. \*\*  $P < 0.01$ , \*\*\*  $P < 0.0001$  versus control and #  $P < 0.05$  versus OGD group.  $n = 6$  repeats.

## 5. Conclusions

In conclusion, this study showed that, during the early stage of ischemic stroke, CRT was quickly upregulated within hours, transferred to the surface of neurons, and bound to FasL. This led to inhibition of Fas/FasL-mediated neuronal apoptosis and indicated the potential of CRT in neuron protection following ischemic stroke.

## Conflict of Interests

The authors declare that they have no conflict of interests related to this research or paper.

## References

- [1] K. Srinivasan and S. S. Sharma, "Augmentation of endoplasmic reticulum stress in cerebral ischemia/reperfusion injury associated with comorbid type 2 diabetes," *Neurological Research*, vol. 33, no. 8, pp. 858–865, 2011.
- [2] A. Martin-Villalba, I. Herr, I. Jeremias et al., "CD95 ligand (Fas-L/APO-1L) and tumor necrosis factor-related apoptosis-inducing ligand mediate ischemia-induced apoptosis in neurons," *The Journal of Neuroscience*, vol. 19, no. 10, pp. 3809–3817, 1999.
- [3] L. I. Gold, P. Eggleton, M. T. Sweetwyne et al., "Calreticulin: non-endoplasmic reticulum functions in physiology and disease," *FASEB Journal*, vol. 24, no. 3, pp. 665–683, 2010.
- [4] J. M. Tarr, P. J. Young, R. Morse et al., "A mechanism of release of calreticulin from cells during apoptosis," *Journal of Molecular Biology*, vol. 401, no. 5, pp. 799–812, 2010.
- [5] J. Jia, D. Guan, W. Zhu et al., "Estrogen inhibits Fas-mediated apoptosis in experimental stroke," *Experimental Neurology*, vol. 215, no. 1, pp. 48–52, 2009.
- [6] A. Rosell, E. Cuadrado, J. Alvarez-Sabín et al., "Caspase-3 is related to infarct growth after human ischemic stroke," *Neuroscience Letters*, vol. 430, no. 1, pp. 1–6, 2008.
- [7] K. Duus, R. T. Pagh, U. Holmskov, P. Højrup, S. Skov, and G. Houen, "Interaction of calreticulin with CD40 ligand, TRAIL and Fas ligand," *Scandinavian Journal of Immunology*, vol. 66, no. 5, pp. 501–507, 2007.
- [8] J. M. Tarr, P. G. Winyard, B. Ryan et al., "Extracellular calreticulin is present in the joints of patients with rheumatoid arthritis and inhibits FasL (CD95L)-mediated apoptosis of T cells," *Arthritis and Rheumatism*, vol. 62, no. 10, pp. 2919–2929, 2010.
- [9] M. Zhang, Q. Li, L. Chen et al., "PSD-93 deletion inhibits Fyn-mediated phosphorylation of NR2B and protects against focal cerebral ischemia," *Neurobiology of Disease*, vol. 68, pp. 104–111, 2014.
- [10] H. Zhao, S.-L. Wang, L. Qian et al., "Diammonium glycyrrhizinate attenuates  $\text{A}\beta(1-42)$ -induced neuroinflammation and regulates MAPK and NF- $\kappa$ B pathways in vitro and in vivo," *CNS Neuroscience and Therapeutics*, vol. 19, no. 2, pp. 117–124, 2013.
- [11] J. Li, S. Zhang, M. Lu et al., "Hydroxysafflor yellow A suppresses inflammatory responses of BV2 microglia after oxygen-glucose deprivation," *Neuroscience Letters*, vol. 535, no. 1, pp. 51–56, 2013.
- [12] Z. Zhang, Z. Wu, X. Zhu, X. Hui, J. Pan, and Y. Xu, "Hydroxysafflor yellow A inhibits neuroinflammation mediated by  $\text{A}\beta 1-42$  in BV-2 cells," *Neuroscience Letters*, vol. 562, pp. 39–44, 2014.
- [13] L. I. Gold, P. Eggleton, M. T. Sweetwyne et al., "Calreticulin: non-endoplasmic reticulum functions in physiology and disease," *The FASEB Journal*, vol. 24, no. 3, pp. 665–683, 2010.
- [14] S. Mans, Y. Banz, B. U. Mueller, and T. Pabst, "The angiogenesis inhibitor vasostatin is regulated by neutrophil elastase-dependent cleavage of calreticulin in AML patients," *Blood*, vol. 120, no. 13, pp. 2690–2699, 2012.
- [15] D. H. Shin, E. Lee, H. J. Kim et al., "Fas ligand mRNA expression in the mouse central nervous system," *Journal of Neuroimmunology*, vol. 123, no. 1-2, pp. 50–57, 2002.
- [16] T. Imanishi, D. K. Han, L. Hofstra et al., "Apoptosis of vascular smooth muscle cells is induced by Fas ligand derived from monocytes/macrophage," *Atherosclerosis*, vol. 161, no. 1, pp. 143–151, 2002.
- [17] W. Wang, T. Wang, W.-Y. Feng, Z.-Y. Wang, M.-S. Cheng, and Y.-J. Wang, "Ecdysterone protects gerbil brain from temporal global cerebral ischemia/reperfusion injury via preventing neuron apoptosis and deactivating astrocytes and microglia cells," *Neuroscience Research*, vol. 81-82, pp. 21–29, 2014.
- [18] M. Li, J. Peng, M.-D. Wang, Y.-L. Song, Y.-W. Mei, and Y. Fang, "Passive movement improves the learning and memory function of rats with cerebral infarction by inhibiting neuron cell apoptosis," *Molecular Neurobiology*, vol. 49, no. 1, pp. 216–221, 2014.
- [19] F.-N. Niu, X. Zhang, X.-M. Hu et al., "Targeted mutation of Fas ligand gene attenuates brain inflammation in experimental stroke," *Brain, Behavior, and Immunity*, vol. 26, no. 1, pp. 61–71, 2012.
- [20] M. Michalak, J. Groenendyk, E. Szabo, L. I. Gold, and M. Opas, "Calreticulin, a multi-process calcium-buffering chaperone of the endoplasmic reticulum," *Biochemical Journal*, vol. 417, no. 3, pp. 651–666, 2009.

## Research Article

# Effects of Nogo-A Silencing on TNF- $\alpha$ and IL-6 Secretion and TH Downregulation in Lipopolysaccharide-Stimulated PC12 Cells

Jianbin Zhong,<sup>1</sup> Shengnuo Fan,<sup>2</sup> Zhenwen Yan,<sup>2</sup> Songhua Xiao,<sup>2</sup> Limei Wan,<sup>1</sup> Chibang Chen,<sup>1</sup> Simin Zhong,<sup>1</sup> Lu Liu,<sup>1</sup> and Jun Liu<sup>2</sup>

<sup>1</sup>Neurology Department, People's Hospital of Zengcheng City (Boji Hospital Affiliated to Sun Yat-sen University), Guangzhou 511300, China

<sup>2</sup>Neurology Department, Sun Yat-sen Memorial Hospital, Sun Yat-sen University, Guangzhou 510120, China

Correspondence should be addressed to Jun Liu; docliujun@hotmail.com

Received 8 May 2015; Accepted 25 June 2015

Academic Editor: Sun-On Chan

Copyright © 2015 Jianbin Zhong et al. This is an open access article distributed under the Creative Commons Attribution License, which permits unrestricted use, distribution, and reproduction in any medium, provided the original work is properly cited.

Parkinson's disease (PD) is a common degenerative disease that lacks efficient treatment. Myelin-associated neurite outgrowth inhibitor A (Nogo-A) is relevant with inhibition of nerve regeneration and may play vital role in pathogenesis of PD. The study aimed to establish the shRNA expression plasmids of Nogo-A gene and explore the regulatory effects of Nogo-A silencing on the expression of inflammation factor tumor necrosis factor-alpha (TNF-alpha) and interleukin-6 (IL-6) as well as tyrosine hydroxylase (TH) in lipopolysaccharide- (LPS-) stimulated rat PC12 cells. The results showed that both mRNA and protein levels of Nogo-A in pGenesil-nogoA-shRNA group were downregulated. The viabilities of PC12 cells decreased with increase of LPS concentrations. LPS significantly increased the supernatant TNF-alpha and IL-6 concentrations and reduced TH protein expression in PC12 cells, while silencing Nogo-A could block these effects. These results suggested that LPS can activate PC12 cells to secrete inflammatory cytokines and lower the TH expression, which can be regulated by Nogo-A gene silencing. Nogo-A silencing might provide new ideas for PD treatment in the future.

## 1. Introduction

Parkinson's disease (PD) is a degenerative disease of extrapyramidal system commonly seen in middle-aged and aged people with the main pathological manifestations including loss of substantia nigra dopaminergic neurons and formation of Lewy body (LB) in nerve cells. As an incurable progressive disease, PD is primarily currently treated symptomatically without significant efficacy. Recent studies have suggested that gene therapy is likely to be a radical strategy for many incurable diseases in the near future by finding and targeting disease-causing genes and pathways; therefore, searching for PD-related genes and applying gene therapy may be one of the most effective means to treat PD [1, 2]. Myelin-associated neurite outgrowth inhibitor (Nogo) is a myelin sheath-derived protein expressed in oligodendrocytes and extensive neurons and is associated with inhibition of neurite outgrowth of the central nervous

system. There are three forms of Nogo, Nogo-A, Nogo-B, and Nogo-C. Nogo-A is a myelin-associated protein currently known to be most effective in central nervous system (CNS) inhibition. Its primary knowledge is mainly originated from the findings in experiments of central nerves repair after nerve injury. The results have indicated that Nogo-A, expressed by oligodendrocytes in both mature brain and spinal nerves, can inhibit neurite outgrowth and regeneration. Studies have shown that the inhibition effects of Nogo-A are involved in NgR signal transduction and RhoA. Researchers have found that neurons also express Nogo proteins, and the expression levels are increased in neuronal injury [3]. Both Nogo-A monoclonal antibody application and Nogo-A gene downregulation are able to partially counteract the inhibition of neurite regeneration and promote the regeneration of damaged nerves, thus enabling partial recovery of the neurological function. Neurite outgrowth inhibition by Nogo-A is also related with

activation of the inflammatory cytokines secretion in neurons [4]. Nogo-A has been shown to be involved in Parkinson's disease [5]. Inflammatory cytokines such as TNF-alpha and IL-6 also play important roles in the occurrence and progression of PD [6]. However, whether Nogo-A regulates generation of the inflammatory factors, thus being involved in the occurrence and progression of PD, is still unknown. This study used lipopolysaccharide- (LPS-) stimulated PC12 cells to establish PD model and silenced Nogo-A genes using RNA interference technology and primarily explore the status of secretion of inflammatory cytokines TNF- $\alpha$  and IL-6 and tyrosine hydroxylase expression in the established model, thus providing new ideas for PD treatment.

## 2. Materials and Methods

### 2.1. Materials

**Cells and Main Reagents.** PC12 cells were provided by Professor Jun Liu. Lipopolysaccharide (LPS) and dimethyl methyl sulfate (DMSO) were purchased from Sigma Corporation. CCK-8 kits were purchased from Japan. Trypsin, DMEM, fetal bovine serum, penicillin, and streptomycin were purchased from Gibco Corporation. Silencer siRNA construction Kit was purchased from Ambion Company, plasmids were purchased from Shanghai GenePharma Company, Lipofectamine2000 transfection reagents were purchased from Invitrogen Corporation, and TRIzol and SYBR Prime Script Real-Time Q-PCR kit were purchased from TAKARA Corporation. Anti-Nogo-A antibodies and anti-tubulin ( $\beta$ -tubulin) antibodies were purchased from Santa Cruz, USA. Anti-tyrosine hydroxylase antibodies and ECL kits were purchased from Merck Millipore. TNF- $\alpha$  and IL-6 ELISA kits were purchased from Shanghai Enzyme-linked Biotechnology Co., Ltd. Others were analytically pure reagents produced in China.

### 2.2. Methods

**2.2.1. Establishment of Nogo-A shRNA Expression Vector and PC12 Cells Transfection.** Nogo-A mRNA sequences were retrieved from the GenBank (genes registration number: NM\_031831.1), shRNA sequences were designed following the principle of siRNA design, Nogo-A gene was searched at 3075 bp after the start codon, the sequences with AA + N19 + UU were selected, and qualified 19 bp sequences were matched in the NCBI database using blast to search nucleotide sequence homology and ensure that the targeted gene is unique, thus determining the shRNA used in this research. Nonsilencing shRNA was designed as 19 bp double stranded RNA without homology to the rat gene sequences. ShRNA sense strand: 5'-AAAUCAGAUGAAGGCCAC-CCAUUTT-3', antisense strand: 5'-AAUGGGUGGCCU-UCAUCUGAUUU-3', nonsilencing shRNA sense strand: 5'-AAAUGACUCAUUGGCGCCUCGUUTT-3', and antisense strand: 5' AACGAGGCGCAAUGAGUCAUUTT-3'. Synthesized fragments were subcloned into pGenesil-1.1 to establish pGenesil-NogoA-shRNA, and pGenesil-1.1 was

used as empty plasmid vector. Traditionally cultured PC12 cells were used as control group. Lipofectamine2000 was used to transfet PC12 cells, and the transfected cells were cultured for 48 h.

### 2.2.2. Detection of Nogo-A Expression Using RT Q-PCR and Western Blot Assays

**Design and Synthesis of Nogo-A and  $\beta$ -Actin Primers.** Nogo-A upstream primer: 5'-CCTGCTCTCGGTGACTATCA-3'; Nogo-A downstream primer: 5'-GTAAACACCCAC-ATCAACACT-3';  $\beta$ -actin upstream primer: 5'-CTATCG-GCAATGAGCGGTTCC-3';  $\beta$ -actin downstream primer: 5'-TGTGTTGGCATAGAGGTCTTTACG-3'. Total RNA of the cells from three groups was extracted, cDNA synthesis was performed using reverse transcription Kit, and Nogo-A and  $\beta$ -actin primers were used for reaction using Bio-Rad Q-PCR instrument, thus obtaining the relative expression values of Nogo-A/ $\beta$ -actin.

**Detection of Nogo-A Protein Expression Using Western Blot Assays.** Total cellular proteins of the three groups were extracted using total protein extraction Kit. Proteins were transferred to nitrocellulose membranes by 10% and 5% SDS-PAGE electrophoresis, and the membranes were blocked by 10% defatted milk. Rabbit anti-Nogo-A antibodies (dilution ratio 1:1000) and anti-tubulin ( $\beta$ -tubulin) antibodies (dilution ratio 1:1000) were added to react at 4°C overnight, the membrane was rinsed by TBST 3 times and then added with horseradish peroxidase labeled goat anti-rabbit secondary antibodies (dilution ratio 1:5,000) to react at room temperature for 1 h, and ECL reagents were added to the membrane before exposure and photographing in dark room. Image analysis software Image J was used for quantitative analysis of the gray values of protein electrophoresis band.

**2.2.3. Establishment of Injury Model of LPS-Stimulated PC12 Cells.** PC12 cells were seeded at  $5 \times 10^3$  cells/well in 96-well plate and treated with various concentrations of LPS (0.01 to 100 nmol/L), cultured for 24 h, added with 10  $\mu$ L CCK-8 reagents, and incubated for 1 h, and then OD450 of each well were determined using MICROPLATE READER to evaluate the cell vitality and determine the optimal concentration for cell injury. After the optimal concentration was evaluated, we further investigated whether silencing of Nogo-A would affect the viability of PC12 cells after LPS challenge.

**2.2.4. Detection of Supernatant TNF- $\alpha$  and IL-6 Using ELISA.** According to the results of Section 2.2.3, the cells in control group, pGenesil-nogoA-shRNA group, and pGenesil-1.1 group were exposed to LPS at optimal concentration for 24 h, and TNF- $\alpha$  and IL-6 concentrations in supernatant fluid of each group were determined using conventional double antibody sandwich ELISA with microplate reader according to the ELISA Kit instructions.

**2.2.5. Detection of TH Expression Using Western Blot Assays.** Based on the results of Section 2.2.3, the cells in control group,

pGenesil-nogoA-shRNA group, and pGenesil-1.1 group were exposed to LPS at optimal concentration for 24 h, and Western blot assays were conducted using total protein extracts of each group according to the above described procedures.

**2.2.6. Statistical Analysis.** Each experiment described above had been replicated at least 3 times independently. All experimental data were analyzed using SPSS17.0 software, and measurement data were expressed as mean  $\pm$  standard deviation ( $x \pm s$ ) and analyzed using one-way ANOVA and LSD *t*-test.  $p < 0.05$  indicated a statistically significant difference.

### 3. Results

**3.1. mRNA and Protein Expressions in PC12 Cells after Nogo-A Silence.** RT Q-PCR results showed that control group and empty vector group were not significantly different in Nogo-A mRNA expression ( $p > 0.05$ ), whereas pGenesil-nogoA-shRNA (pG-Nogo) group had a significantly lower Nogo-A mRNA expression than those in control group and empty vector group. Results of Western blot assays showed that, compared with the control group and empty vector group, Nogo-A proteins at hour 48 after shRNA were reduced with statistical significance ( $p < 0.05$ ) (Figure 1).

**3.2. Determination of Cell Viability.** CCK8 tests showed that PC12 cell viabilities at hour 24 decreased gradually ( $p < 0.05$ ) with the gradual increase of LPS concentrations (0.01 to 100 nmol/L, Figure 2(a)) and got a relatively ideal value at 1 nmol/L ( $76 \pm 2.1\%$ ), which was used in subsequent experiments. Moreover, silencing of Nogo-A attenuated the viability loss of PC12 cells after LPS challenge (Figure 2(b)).

**3.3. Detection of Supernatant TNF- $\alpha$  and IL-6 by ELISA.** LPS at work concentration of 1 nmol/L was used, control group (untreated PC12 cells), pGenesil-1.1 + LPS group, and pGenesil-nogoA-shRNA + LPS group were exposed for 24 h before the ELISA assays were performed and the OD450 were recorded using MICROPLATE READER, the standard values were calculated according to the standard curve, mean values of three independent experiments were taken ( $p < 0.05$ ), and the results showed that LPS significantly increased the supernatant TNF-alpha and IL-6 concentrations, while silencing Nogo-A could block these effects (Figure 3).

**3.4. Detection of TH and Nogo-A Expression Using Western Blot Assays.** LPS at work concentration of 1 nmol/L was used, control group (untreated PC12 cells), pGenesil-1.1 + LPS group, and pGenesil-nogoA-shRNA + LPS group were exposed for 24 h before total proteins were extracted and determined by Western blotting assays, and the results showed that LPS could significantly reduce TH protein expression in PC12 cells, while Nogo-A silencing somewhat restored the protein level compared with the group treated by LPS alone (Figure 4).

### 4. Discussion

Currently confirmed neurite regeneration inhibitory factors include three classes, namely, soluble myelin-associated glycoprotein (MAG), oligodendrocyte myelin glycoprotein (OMgp), and three of Nogo proteins [7]. There are three isomers of homologous Nogo: Nogo-A, Nogo-B, and Nogo-C. Nogo-A performs strong neurite outgrowth inhibition effects. Nogo-66 loop of Nogo-A is bound by its receptor NgR and transferred to p75/RhoA/ROCK to activate the cAMP and cause intracellular signal transduction, thereby leading to nerve outgrowth inhibition.

Nogo-A is mainly distributed in oligodendrocytes and additionally is highly expressed in the neurons. Wang et al. [8] found that Nogo-A and Nogo receptors are highly expressed in the neuron nucleus of the cerebral cortex, hippocampus, hypothalamus, globus pallidus, caudate-putamen nucleus, and substantia nigra. Studies found that the positive density of Nogo-A in anterior horn motor neurons of mouse spinal cord was very high. The distribution characteristic of Nogo-A determined that its abnormal expression played an important role in the occurrence and progression in nervous system diseases such as cerebral and spinal trauma, stroke, and neurodegenerative diseases [9, 10]. As a common degenerative disease of the nervous system, PD is related with the loss and regeneration inhibition of dopaminergic neuron, and Nogo-A had been confirmed to be involved in the process [11–13].

Therefore, as a key factor in development and progression of nervous system diseases described above, Nogo-A may serve as potential therapeutic targets of various diseases, especially the PD. Chen et al. [14] found that application of specific antibody of Nogo-A protein IN-1 could block the neurite inhibition activity of Nogo-A, and GrandPré et al. [15] found that NgR antagonists could facilitate the neurite regeneration. Yang et al. [16] found that Nogo-A silencing could promote the recovery of demyelinating disease. Wang et al. [17] found that neurite outgrowth inhibition by Nogo-A was closely related with Wnt pathways, c-Jun, and c-Myc. Some scholars believed that Nogo-A is also involved in neuronal differentiation, apoptosis, and generation of free radicals [18, 19]. Interestingly, studies of Schapira et al. [2] indicated that neural inhibition of Nogo-A was related with inflammatory mediators.

With reference to various investigations [20, 21], we established PD model using LPS-stimulated PC12 cells, and the results showed that LPS significantly increased the supernatant TNF-alpha and IL-6 concentrations of PC12 cells while inhibiting the PC12 cell vitality, indicating that inflammation factor played an important role in PD pathogenesis. Nogo-A silencing led to significant decline of inflammation factors secretion and alleviated the cell viability loss induced by LPS, suggesting that Nogo-A gene was involved in inflammation factor secretion in PD. As an enzyme responsible for catalyzing conversion of amino acid l-tyrosine to dihydroxyphenylalanine, TH plays a decisive role in the synthesis of dopamine. Sufficient TH expression can lead to dopamine synthesis reduction and eventual PD pathogenesis. Therefore, it has been recognized as an indicator of PD [1, 22, 23]. The results of this study showed that LPS could significantly

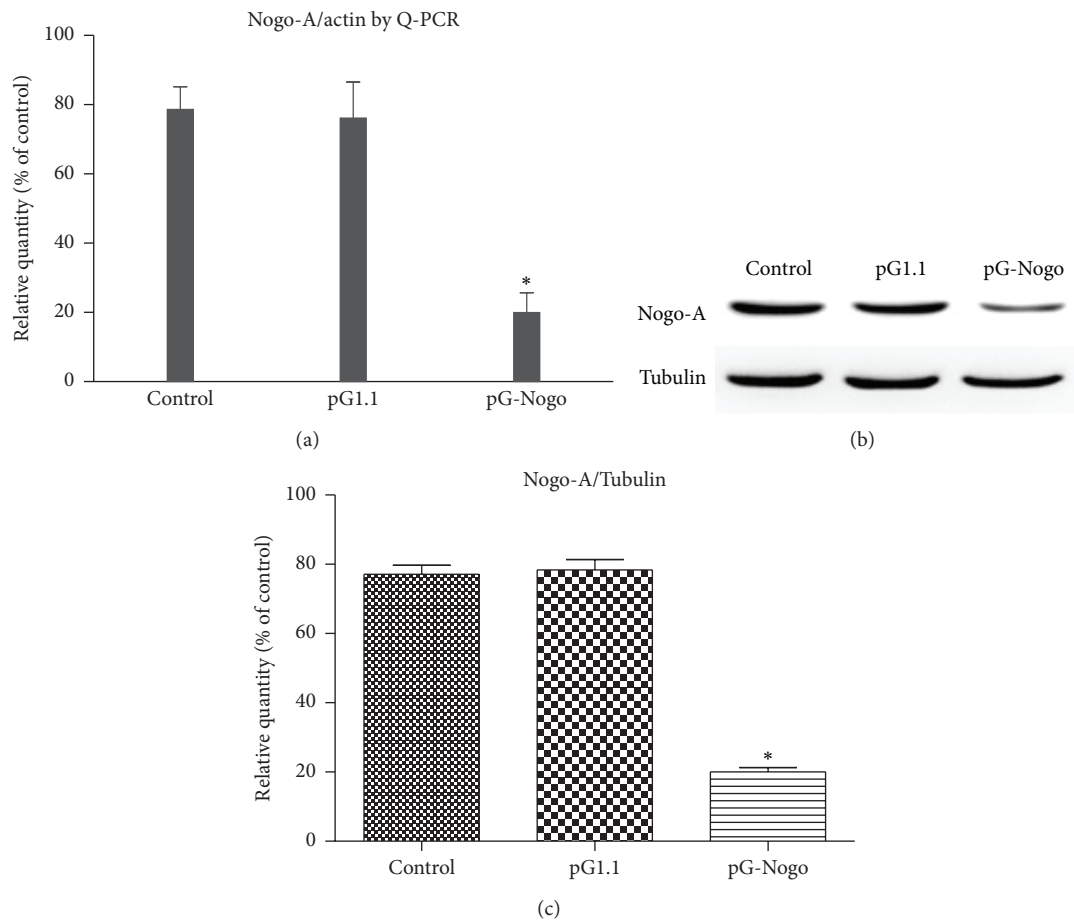


FIGURE 1: Detection of (a) Nogo-A mRNA levels using fluorescence quantitative PCR; (b, c) protein level using Western blot assays. pG1.1 refers to pGenesil-1.1 and pG-Nogo refers to pGenesil-nogoA-shRNA. \* $p < 0.05$ .

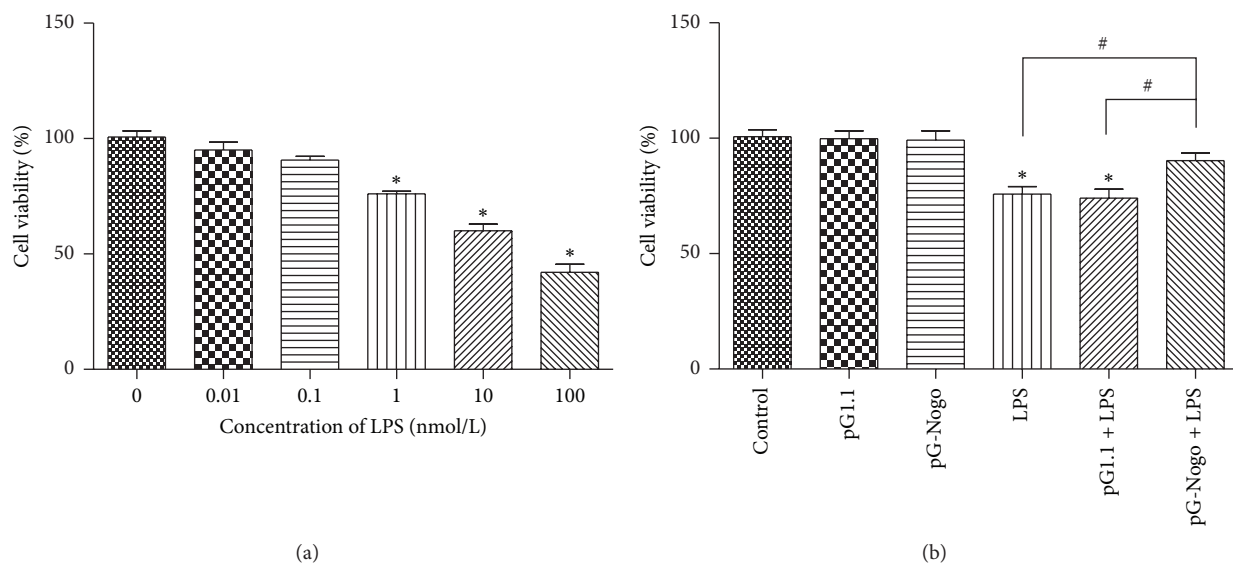
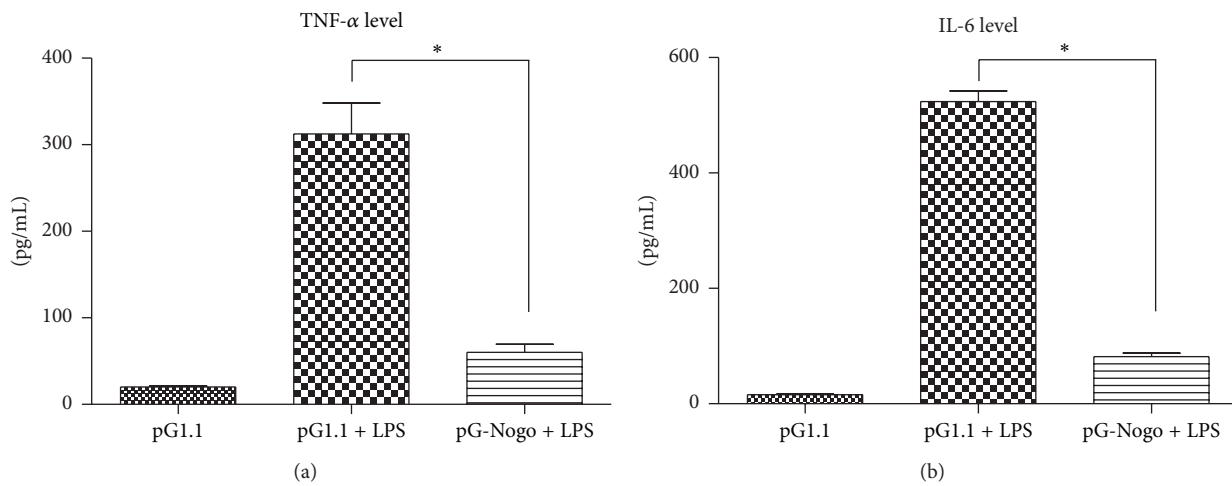
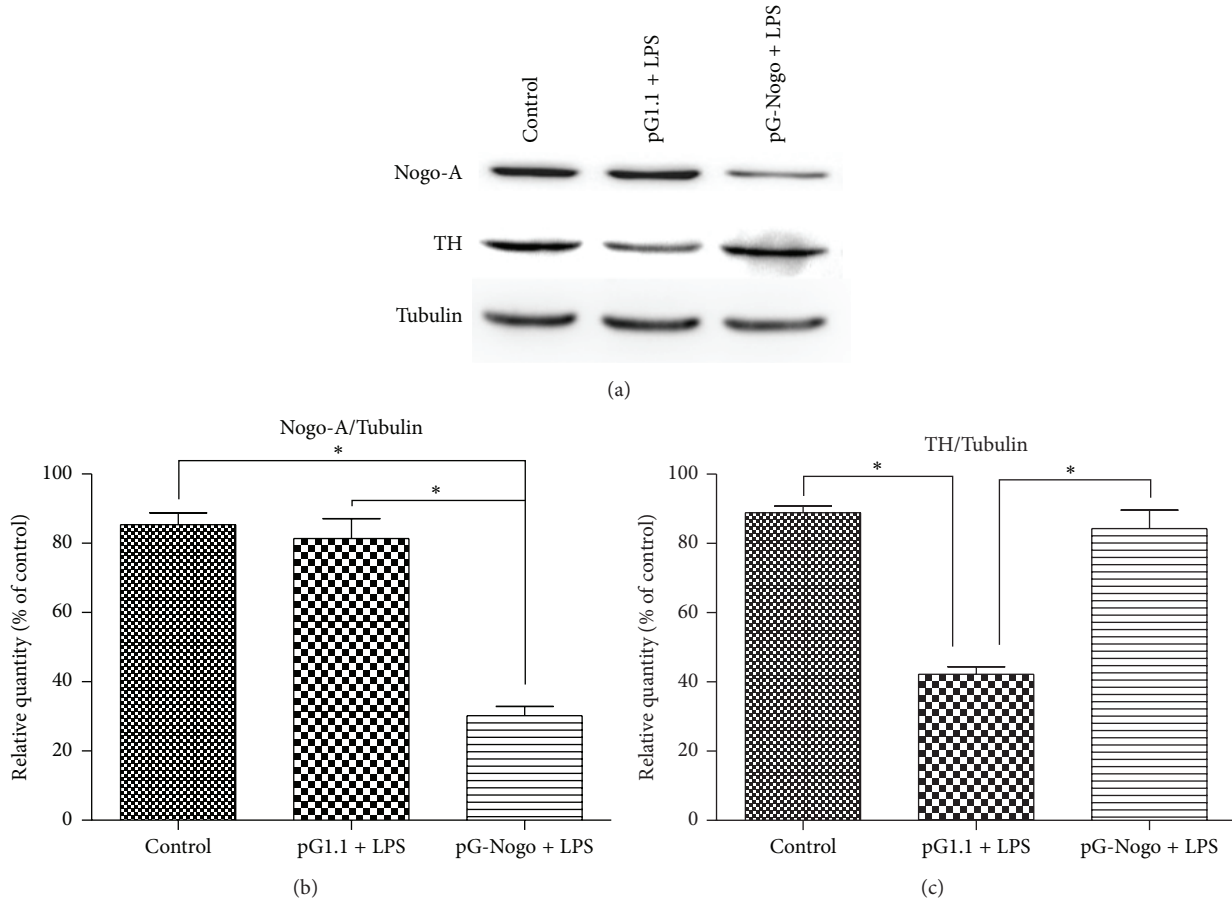


FIGURE 2: Cell viability tested by CCK8. (a) Gradual increase of LPS concentrations. (b) Silencing of Nogo-A on PC12 cells after treatment with LPS 1 nmol/L. \*\*#  $p < 0.05$ .

FIGURE 3: Detection of supernatant TNF- $\alpha$  and IL-6 using ELISA, \*  $P < 0.05$ .FIGURE 4: TH and Nogo-A levels of various groups determined by Western blot assays, \*  $P < 0.05$ .

reduce TH protein expression in PC12 cells. TH protein expression in group of Nogo-A silencing was somewhat restored compared with the group treated by LPS alone, showing that Nogo-A influenced the TH expression. These results suggest that Nogo-A has promotive effects on PD

and may accelerate the process of PD possibly by increasing the inflammatory substances secretion and reducing the TH expression through a certain way, but the exact mechanism is unclear and needs further investigation in the future.

## 5. Conclusion

This study indicated that Nogo-A had promotive effects on PD and might accelerate the process of PD possibly by increasing TNF-alpha and IL-6 secretion and reducing the TH expression. Silencing the Nogo-A presented a protective effect in the study, which provided new ideas for PD treatment.

## Conflict of Interests

The authors report no conflict of interests.

## Authors' Contribution

Jianbin Zhong and Shengnuo Fan contributed equally to this work.

## Acknowledgments

This work was supported by the National Natural Science Foundation of China (no. 81372919) and the Guangdong Natural Science Foundation (nos. S2012010010242 and S2013010013964).

## References

- [1] W. Khan, M. Priyadarshini, H. A. Zakai, M. A. Kamal, and Q. Alam, "A brief overview of tyrosine hydroxylase and alpha-synuclein in the Parkinsonian brain," *CNS & Neurological Disorders—Drug Targets*, vol. 11, no. 4, pp. 456–462, 2012.
- [2] A. H. Schapira, C. W. Olanow, J. T. Greenamyre, and E. Bezard, "Slowing of neurodegeneration in Parkinson's disease and Huntington's disease: future therapeutic perspectives," *The Lancet*, vol. 384, no. 9942, pp. 545–555, 2014.
- [3] X. Peng, J. Kim, Z. Zhou, D. J. Fink, and M. Mata, "Neuronal Nogo-A regulates glutamate receptor subunit expression in hippocampal neurons," *Journal of Neurochemistry*, vol. 119, no. 6, pp. 1183–1193, 2011.
- [4] N. R. Mehta, T. Nguyen, J. W. Bullen, J. W. Griffin, and R. L. Schnaar, "Myelin-associated glycoprotein (MAG) protects neurons from acute toxicity using a ganglioside-dependent mechanism," *ACS Chemical Neuroscience*, vol. 1, no. 3, pp. 215–222, 2010.
- [5] K. Schawkat, S. Di Santo, S. Seiler, A. Ducray, and H. Widmer, "Loss of Nogo-A-expressing neurons in a rat model of Parkinson's disease," *Neuroscience*, vol. 288, pp. 59–72, 2015.
- [6] S. V. More, H. Kumar, I. S. Kim, S. Song, and D.-K. Choi, "Cellular and molecular mediators of neuroinflammation in the pathogenesis of Parkinson's disease," *Mediators of Inflammation*, vol. 2013, Article ID 952375, 12 pages, 2013.
- [7] J. K. Lee and B. Zheng, "Role of myelin-associated inhibitors in axonal repair after spinal cord injury," *Experimental Neurology*, vol. 235, no. 1, pp. 33–42, 2012.
- [8] X. Wang, S. J. Chun, H. Treloar et al., "Localization of Nogo-A and Nogo-66 receptor proteins at sites of axon-myelin and synaptic contact," *The Journal of Neuroscience*, vol. 22, no. 13, pp. 5505–5515, 2002.
- [9] A. Schmandke, A. Schmandke, and M. E. Schwab, "Nogo-A: multiple roles in CNS development, maintenance, and disease," *The NeuroScientist*, vol. 20, no. 4, pp. 372–386, 2014.
- [10] T. Wang, J. Q. Xiong, X. B. Ren, and W. Sun, "The role of Nogo-A in neuroregeneration: a review," *Brain Research Bulletin*, vol. 87, no. 6, pp. 499–503, 2012.
- [11] C. Delay, C. Tremblay, E. Brochu et al., "Increased LINGO1 in the cerebellum of essential tremor patients," *Movement Disorders*, vol. 29, no. 13, pp. 1637–1647, 2014.
- [12] H. Inoue, L. Lin, X. Lee et al., "Inhibition of the leucine-rich repeat protein LINGO-1 enhances survival, structure, and function of dopaminergic neurons in Parkinson's disease models," *Proceedings of the National Academy of Sciences of the United States of America*, vol. 104, no. 36, pp. 14430–14435, 2007.
- [13] S. Seiler, D. Pollini, S. Di Santo, and H. R. Widmer, "Antagonizing Nogo-receptor 1 promotes the number of cultured dopaminergic neurons and elongates their neurites," *NeuroReport*, vol. 24, no. 18, pp. 1047–1052, 2013.
- [14] M. S. Chen, A. B. Huber, M. E. van der Haar et al., "Nogo-A is a myelin-associated neurite outgrowth inhibitor and an antigen for monoclonal antibody IN-1," *Nature*, vol. 403, no. 6768, pp. 434–439, 2000.
- [15] T. GrandPré, S. Li, and S. M. Strittmatter, "Nogo-66 receptor antagonist peptide promotes axonal regeneration," *Nature*, vol. 417, no. 6888, pp. 547–551, 2002.
- [16] Y. Yang, Y. Liu, P. Wei et al., "Silencing Nogo-A promotes functional recovery in demyelinating disease," *Annals of Neurology*, vol. 67, no. 4, pp. 498–507, 2010.
- [17] Y. Wang, J. Gu, X. Feng, H. Wang, Y. Tao, and J. Wang, "Effects of Nogo-A receptor antagonist on the regulation of the Wnt signaling pathway and neural cell proliferation in newborn rats with hypoxic ischemic encephalopathy," *Molecular Medicine Reports*, vol. 8, no. 3, pp. 883–886, 2013.
- [18] N. Xiong, "RNA interference suppression of Nogo-66 receptor prevents Nogo-66-mediated inhibition of invasion and adhesion and simultaneously increases cell apoptosis in C6 cells," *Oncology Reports*, vol. 30, no. 5, pp. 2171–2178, 2013.
- [19] Y. J. Mi, B. Hou, Q. Liao et al., "Amino-Nogo-A antagonizes reactive oxygen species generation and protects immature primary cortical neurons from oxidative toxicity," *Cell Death and Differentiation*, vol. 19, no. 7, pp. 1175–1186, 2012.
- [20] R. M. Yagnik and K. E. Benzeroual, "Tigecycline prevents LPS-induced release of pro-inflammatory and apoptotic mediators in neuronal cells," *Toxicology in Vitro*, vol. 27, no. 2, pp. 686–693, 2013.
- [21] M. R. Zarrindast, M. Javadi-Paydar, L. Delphi et al., "Morphine-induced nitric oxide production in PC12 cells," *Archives of Iranian Medicine*, vol. 15, no. 7, pp. 404–408, 2012.
- [22] J. Haavik and K. Toska, "Tyrosine hydroxylase and Parkinson's disease," *Molecular Neurobiology*, vol. 16, no. 3, pp. 285–309, 1998.
- [23] S. Tabrez, N. R. Jabir, S. Shakil et al., "A synopsis on the role of tyrosine hydroxylase in Parkinson's disease," *CNS & Neurological Disorders—Drug Targets*, vol. 11, no. 4, pp. 395–409, 2012.

## Research Article

# Screening and Identification of ssDNA Aptamer for Human GP73

Jingchun Du,<sup>1</sup> Jianming Hong,<sup>1</sup> Chun Xu,<sup>1</sup> Yuanyuan Cai,<sup>1</sup> Bo Xiang,<sup>2</sup>  
Chengbo Zhou,<sup>1</sup> and Xia Xu<sup>1</sup>

<sup>1</sup>Kingmed College of Laboratory Medicine, Guangzhou Medical University, Guangzhou 510182, China

<sup>2</sup>Department of Laboratory Medicine, The First Affiliated Hospital, Guangzhou Medical University, Guangzhou 510120, China

Correspondence should be addressed to Xia Xu; [xuxia503@126.com](mailto:xuxia503@126.com)

Received 29 June 2015; Accepted 8 September 2015

Academic Editor: William Z. Suo

Copyright © 2015 Jingchun Du et al. This is an open access article distributed under the Creative Commons Attribution License, which permits unrestricted use, distribution, and reproduction in any medium, provided the original work is properly cited.

As one tumor marker of HCC, Golgi Protein 73 (GP73) is given more promise in the early diagnosis of HCC, and aptamers have been developed to compete with antibodies as biorecognition probes in different detection system. In this study, we utilized GP73 to screen specific ssDNA aptamers by SELEX technique. First, GP73 proteins were expressed and purified by prokaryotic expression system and Nickle ion affinity chromatography, respectively. At the same time, the immunogenicity of purified GP73 was confirmed by Western blotting. The enriched ssDNA library with high binding capacity for GP73 was obtained after ten rounds of SELEX. Then, thirty ssDNA aptamers were sequenced, in which two ssDNA aptamers with identical DNA sequence were confirmed, based on the alignment results, and designated as A10-2. Furthermore, the specific antibody could block the binding of A10-2 to GP73, and the specific binding of A10-2 to GP73 was also supported by the observation that several tumor cell lines exhibited variable expression level of GP73. Significantly, the identified aptamer A10-2 could distinguish normal and cancerous liver tissues. So, our results indicate that the aptamer A10-2 might be developed into one molecular probe to detect HCC from normal liver specimens.

## 1. Introduction

Hepatocellular carcinoma (HCC) is one of the most common and highly malignant tumors worldwide [1]. At present, alpha-fetoprotein (AFP) assay and ultrasonography are employed in screening for early stage HCC. However, the sensitivity and specificity of these screening methods remain a major hurdle in early diagnosis of HCC. Because of the lack of a method for early diagnosis of HCC, the 5-year survival rate is less than 5% [2–4]. Therefore it is urgently needed to develop new methods for early diagnosis of HCC.

Golgi protein-73 (GP 73) is a type II Golgi membrane protein, which is significantly increased in HCC [5–7]. More interestingly, the sensitivity and specificity of GP73 for diagnosis of HCC are higher than those of AFP, which makes it be a better biomarker for early diagnosis of HCC [8–10]. Currently, an ELISA method that utilizes GP73 antibody is available for measurement of serum GP73.

Aptamers are short single-strand oligonucleotides, which could be selected from random oligonucleotides library via systemic evolution of ligands by exponential enrichment

(SELEX) technology. Importantly, aptamers bind target molecules with high affinity and selectivity [11, 12]. Unlike antibodies whose purity and specificity may vary among different preparations, aptamers can be easily synthesized and are extremely stable [13]. In addition, they could be easily labeled with fluorescent dyes or other reporters for diagnosis purpose [14].

Here, we screened the random oligonucleotides library for ssDNA aptamers against GP73 and identified several aptamers. We further characterized a selected aptamer and verified that it could recognize GP73 expressed in hepatic tissue.

## 2. Materials and Methods

**2.1. Expression, Purification, and Identification of Recombinant Human GP73.** The encoding sequence of Human GP73 was first amplified by PCR using specific primers (5'-CGG GAT CCA TGG GCT TGG GAA ACG GGC-3' and 5'-GGA AGC TTG AGT GTA TGA TTC CG-3'). After gel purification,

the PCR product was digested with BamH I and Hind III and ligated into vector pET-32a. The ligation product was transformed into DH5 $\alpha$  and recombinant clones were picked up for verification using PCR and enzyme digestion. The pET-32a-GP73 plasmid was finally confirmed by DNA sequencing.

The pET-32a-GP73 vector was transformed into *E. coli* BL21 (DE3) and positive clones, obtained by ampicillin selection, were induced to express GP73 by isopropyl  $\beta$ -D-1-thiogalactopyranoside (IPTG) (1 mM) under low temperature (25°C). The cell culture was harvested, resuspended in cold phosphate buffered saline (PBS) buffer, and lysed by sonication on ice with 10 sec on and 10 sec off intervals for a total of 25 cycles. The supernatant was collected by centrifugation at 10,000  $\times g$  for 20 min at 4°C and then applied to a Ni<sup>2+</sup>-chelating chromatography column. The column was eluted by a stepwise gradient of PBS containing different concentrations of imidazole (from 20 to 500 mM). The eluant was collected and analyzed by SDS-PAGE. The fractions containing recombinant protein GP73 were dialysed against PBS buffer and concentrated by concentrator (Eppendorf, Hamburg, Germany).

**2.2. Western Blotting.** The immunogenicity of the recombinant GP73 was detected by Western blotting with specific anti-GP73 antibody (Abcam, Cambridge, MS, USA). The purified GP73 protein or control samples (host cell lysate) were diluted with Laemmli buffer and denatured at 100°C for 5 min and centrifuged at 12,000 rpm for 5 min at 4°C. Supernatant was recovered, separated on 10% SDS-PAGE, and transferred onto 0.45  $\mu$ m PVDF membrane (Millipore, Billerica, MA, USA). After blocking membrane with TBS-Tween-20 containing 5% nonfat milk for 1 hour at room temperature, the membrane was incubated with anti-human GP73 antibody overnight at 4°C. Then, the membrane was incubated with horseradish peroxidase- (HRP-) conjugated secondary antibody for 1 hour at room temperature and was detected by chemiluminescence signaling kit (Cell Signaling Technologies, Beverly, MA, USA).

**2.3. SELEX Library and Primers.** The SELEX library contains a 45-base central random sequence flanked by two invariant 20-nucleotide regions in each end (5'-ACG CTC GGA TGC CAC TAC AG-N45-CTC ATG GAC GTG CTG GTG AC-3'). The forward primer (5'-ACG CTC GGA TGC CAC TAC AG-3') labeled with or without digoxigenin (Dig) and reverse primer (5'-GTC ACC AGC ACG TCC ATG AG-3') labeled with or without biotin were used in PCR to obtain the unlabeled, single-labeled, or double-labeled amplification products. All primers were synthesized by Invitrogen Biotech Co., Ltd.

**2.4. In Vitro Screening Procedure.** The selection of aptamers against GP73 was performed using a SELEX technology. First, the purified GP73 or BSA was adsorbed onto the wells of 96-well plates. In detail, the plates were coated with 200  $\mu$ L/well of 2  $\mu$ g/mL of GP73 or BSA dissolved in binding buffer (20 mM HEPES, 120 mM NaCl, 5 mM KCl, 1 mM CaCl<sub>2</sub>, and 1 mM MgCl<sub>2</sub>, pH 7.3) and incubated overnight at 4°C.

After washing for three times with the binding buffer, the incubated plates were blocked with 3% (w/v) BSA solution for 2 hours at 37°C, and unbound BSA was removed. Second, 10  $\mu$ M of the random ssDNA pool was prepared in 100  $\mu$ L of binding buffer and denatured for 5 min at 95°C, cooled for 5 min at 4°C, and then placed at room temperature for 5 min. The denatured ssDNA pool was added into the BSA coated wells and incubated for 40 min at 37°C to eliminate the sequences that were able to bind BSA. The unbound sequences were collected, added into the GP73-coated wells, and incubated for 60 min at 37°C. After incubation, the wells were washed 3 times with binding buffer containing 0.05% Tween-20 to remove unbound and weakly bound sequences. The remained sequences that bound GP73 were incubated in elution buffer (20 mM Tris-HCl, 4 mM GITC, and 1 mM DTT, pH 8.3) for 10 min at 80°C and then collected. The eluted oligonucleotides were purified by DNA purification kit (Tiangen, Beijing, China). The purified oligonucleotides were amplified by optimized PCR (1 cycle at 95°C for 5 min; 12 cycles at 95°C for 30 s, 50°C for 30 s, and 72°C for 30 s; 1 cycle at 72°C for 2 min), with unlabeled forward primer and biotin-labeled reverse primer. After amplification, the PCR products were denatured using 150 mM NaOH solution, and the unlabeled aptamer strands were separated using streptavidin-coated magnetic beads (Invitrogen, Carlsbad, CA, USA) and concentrated by ethanol precipitation. The separated aptamer strands were used as ssDNA pool for the next round of SELEX until the tenth round of screening was finished.

**2.5. Enzyme-Linked Aptamer Sorbent Assay (ELASA).** ELASA was used to monitor the binding affinity between screened ssDNA aptamers and GP73 protein. First, Dig-labeled forward primer was used to prepare Dig-labeled aptamers by PCR at the end of the first, second, fourth, sixth, eighth, and tenth round of SELEX selection, respectively. Then 4  $\mu$ g of Dig-labeled aptamers was dissolved in binding buffer, prepared as above, and added into GP73-BSA coated or BSA coated 96-well microtiter plate and incubated for 60 min at 37°C. After incubation, the wells were washed three times with binding buffer containing 0.05% Tween-20 to remove unbound and weakly bound ssDNA aptamers. Afterwards, 200  $\mu$ L of a 1:10<sup>4</sup> dilution of anti-Dig-ALP (alkaline phosphatase) antibody was added and allowed to react for 30 min at 37°C. Finally, after three-time washes with binding buffer containing 0.05% Tween-20, 200  $\mu$ L of freshly prepared PNPP solution (1 mg/mL) was added and the absorbance was measured at 405 nm after 30 min incubation (after quenching with 100  $\mu$ L/well of 1 M NaOH). The assays were performed in triplicate.

**2.6. Aptamer Sequencing and Secondary Structure Prediction.** After the tenth round of screening, the purified aptamer strands were amplified by PCR with unlabeled primers, and the PCR products were cloned into the pMD19-T vector (Clontech, Beijing, China). Thirty positive clones were picked up and sequenced. The similarity of these sequences was analyzed by sequence alignment software (Clustal). One sequence, which appeared twice among these aptamers,

was designated as A10-2 and subjected to secondary structure prediction using the mFold software [15] at 37°C in 150 mM [Na<sup>+</sup>] and 1 mM [Mg<sup>++</sup>], a web-based server for DNA folding and hybridization predicting (<http://unafold.rna.albany.edu/?q=mfold/DNA-Folding-Form>).

**2.7. Kinetics and Binding Capacity Studies of A10-2 for GP73.** First, the recombinant GP73 protein or fetal bovine serum (FBS) was diluted to a series of concentrations (31.25 ng/mL–4 µg/mL) in binding buffer and 200 µL of each solution was incubated in a 96-well microtiter plate overnight at 4°C. After washing for three times with binding buffer, the incubated plates were blocked with 3% (w/v) BSA solution for 2 hours at 37°C and then again washed three times in order to completely remove unbound BSA. Dig-labeled A10-2 were synthesized in Invitrogen Biotech Co., Ltd., dissolved in binding buffer at 40 ng/µL concentration and then denatured for 5 min at 95°C, cooled for 5 min at 4°C, and then placed at RT for 5 min. Afterwards, 200 µL of A10-2 was added into each well and the plate was incubated at 37°C for 2 hours and washed three times. Then anti-Dig-ALP antibody was added and developed using PNPP solution as mentioned above. The change of absorbance at 405 nm was measured by a microplate reader (Thermo, Shanghai, China) and the assays were performed in triplicate.

Second, three different concentrations of GP73 protein (5 × 10<sup>2</sup>, 1 × 10<sup>3</sup>, and 2 × 10<sup>3</sup> ng/mL) were incubated in the 96-well microtiter plate (200 µL/well) overnight at 4°C, and BSA solution was used to block the plate as above. Afterwards, 200 µL of Dig-labeled A10-2 was diluted into different concentrations (0.078–40 ng/µL) in binding buffer and added into each well. The plate was incubated at 37°C for 2 hours, after which individual well was washed three times with binding buffer to remove unbound Dig-labeled A10-2. Then anti-Dig-ALP antibody was added and developed using PNPP solution as mentioned above. The change of absorbance at 405 nm was measured by a microplate reader (Thermo) and the assays were performed in triplicate.

**2.8. Specificity Studies of A10-2 for GP73 by Antibody Blocking and Western Blotting Experiments.** The recombinant protein GP73 was diluted into 2 µg/mL in binding buffer and 200 µL of solution was incubated in a 96-well microtiter plate overnight at 4°C. After washing for three times with binding buffer, the incubated plates were blocked with 3% (w/v) BSA solution for 2 hours at 37°C and again washed three times in order to completely remove unbound BSA. The anti-GP73 antibody (Abcam) was diluted into a series of concentrations (0.03125–1 µg/mL) and 200 µL of each solution was added into the GP73-BSA coated plate and incubated for 1 hour at 37°C; binding buffer without anti-GP73 antibody was used as negative control. Then the microtiter plate was washed for three times with binding buffer and further incubated with 200 µL of Dig-labeled A10-2 (40 ng/µL). The plate was incubated at 37°C for 2 hours, after which individual wells were washed three times with binding buffer to remove unbound A10-2. Then anti-Dig-ALP antibody was added and developed using PNPP solution as mentioned above. The change of absorbance at 405 nm was measured by a

microplate reader (Thermo) and the assays were performed in triplicate.

To further confirm the specificity of A10-2 for GP73, the expression of GP73 in tumor cells HepG2, MCF-7, MDA-MB-231, MDA-MB-435, and A549 was measured by Western blotting, in which the biotin-labeled A10-2 (5 ng/µL) and streptomycin-conjugated HRP functioned as primary antibody and second antibody.

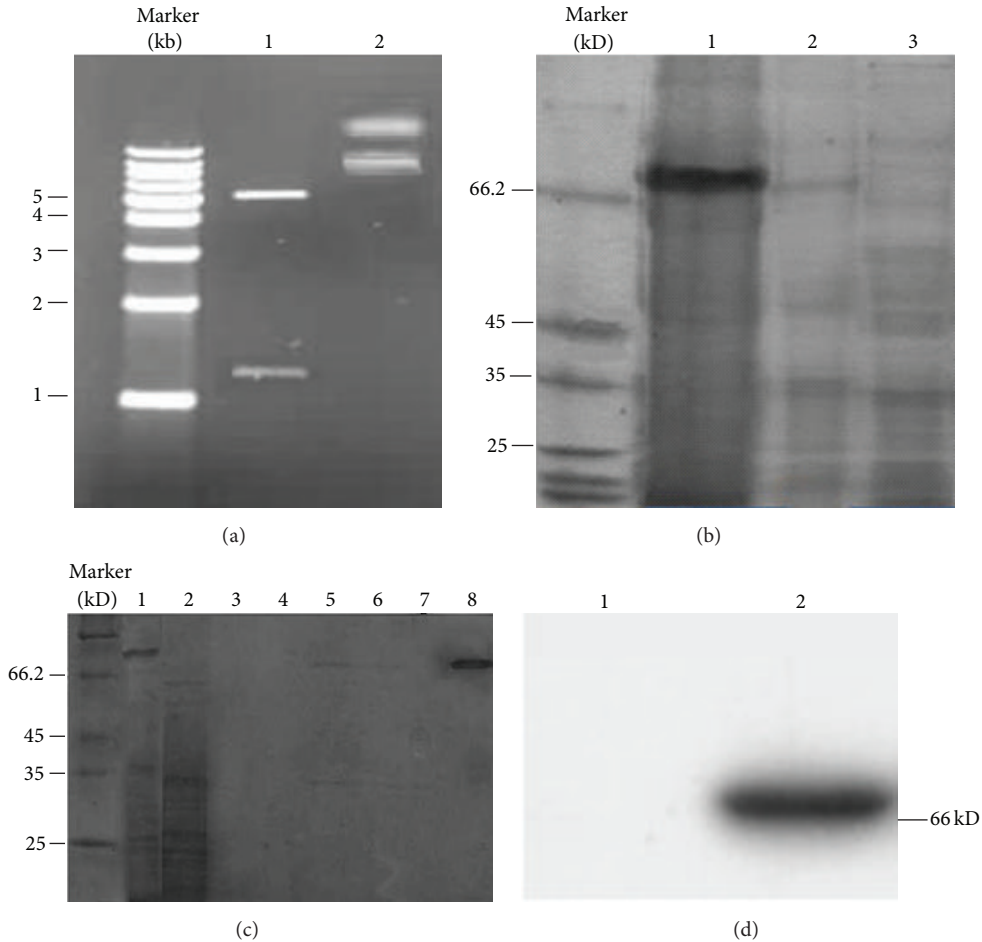
**2.9. Immunohistochemical Staining.** Formalin-fixed and paraffin-embedded tissue blocks derived from 20 normal and hepatocellular carcinoma (HCC) tissues samples were obtained from the First Affiliated Hospital of Guangzhou Medical University with the approval of the Hospital Research Ethics Committee. For histochemistry staining, 5 µm thick sections from tissue blocks were placed on microscopic slides and dried in a 60°C oven for 2 hours. Then, the sections were deparaffinized in xylene, rehydrated using gradient concentrations of ethanol, microwaved in 10 mM citrate buffer for 15 minutes to retrieve antigen, and blocked with 3% hydrogen peroxide for 10 minutes to inhibit endogenous peroxidase activity. After that, the sections were incubated with biotin-labeled A10-2 (40 ng/µL, 1:500 dilution) at 4°C overnight and then incubated with streptavidin-conjugated HRP (Abcam) at RT for 1 hour. Then, color development was performed with a DAB Plus Kit (Maixin, Fuzhou, China). Finally, the sections were counterstained in hematoxylin.

**2.10. Statistics.** Data are presented as means ± SEMs from three to five independent measurements in separate experiments and analyzed using SPSS version 12.0 (SPSS Inc., Chicago, IL, USA). A P value of <0.05 was considered to be statistically significant.

### 3. Results

**3.1. Expression, Purification, and Identification of Human GP73 Protein.** To prepare the recombinant human GP73 protein, the prokaryotic expression vector pET-32a-GP73 was constructed. As shown in Figure 1(a), the encoding sequence of GP73 was correctly inserted into the multiple cloning sites of pET-32a. After the pET-32a-GP73 plasmid was transformed into host *E. coli* BL21 (DE3), a single clone containing the expression vector was cultured into  $A_{600} = 0.6$  and induced to express the recombinant protein GP73 with 1 mM IPTG at 25°C. The expression efficiency and intracellular solubility of GP73 were analyzed by SDS-PAGE. The target protein was expressed with a molecular weight of approximate 68 kDa, which was identical to the predicted size (Figure 1(b)).

The Nickel ion affinity chromatography was used to purify the target protein, because the recombinant GP73 was expressed as a fusion protein with His Tag. As shown in Figure 1(c), the target protein GP73 combined closely with Ni<sup>2+</sup>-saturated matrix was collected with above 90% purification after the nonspecific parts were eluted with a series of concentrations of imidazole solution in PBS buffer. At the same time, the immunogenicity of the recombinant human GP73 was assessed by Western blotting. As shown in



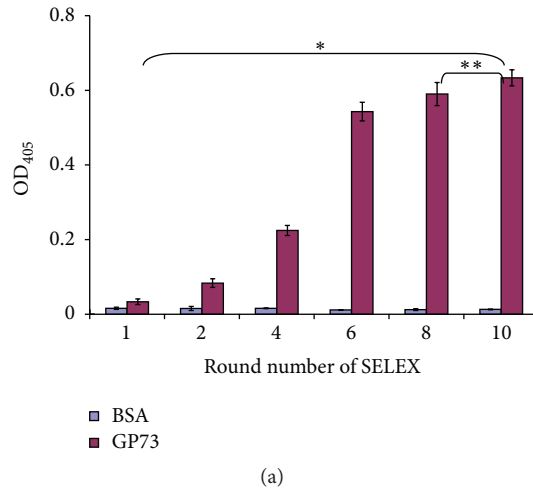
**FIGURE 1:** Preparation of the recombinant protein GP73. (a) The recombinant vector pET-32a-GP73 was confirmed by enzyme digestion. Lane 1, the double enzyme digestion product of the recombinant vector; Lane 2, the recombinant vector without double enzyme digestion. (b) The recombinant protein GP73 was induced in BL21 (DE3) by IPTG (1 mM) at 25°C. Lane 1, the supernatant of host BL21 (DE3) bearing pET-32a-GP73 with induction; Lane 2, the sediment of host BL21 (DE3) bearing pET-32a-GP73 with induction; Lane 3, the total lysate of BL21 (DE3) bearing pET-32a-GP73 without induction. (c) The recombinant protein GP73 was purified by affinity chromatography. Lane 1, the sample containing recombinant protein GP73 before loading affinity chromatography column; Lane 2, the eluate after loading affinity chromatography column; Lane 3, the eluate with PBS containing 20 mM imidazole; Lane 4, the eluate with PBS containing 40 mM imidazole; Lane 5, the eluate with PBS containing 60 mM imidazole; Lane 6, the eluate with PBS containing 80 mM imidazole; Lane 7, the eluate with PBS containing 100 mM imidazole; Lane 8, the eluate with PBS containing 500 mM imidazole. (d) The immunogenicity of the recombinant protein GP73 was confirmed by Western blotting with specific anti-GP73 antibody. Lane 1, the negative control; Lane 2, the purified GP73.

Figure 1(d), the recombinant human GP73 was recognized by specific anti-GP73 antibody.

**3.2. Selection of Specific Aptamers for Human GP73 Protein.** The aptamers specific for GP73 protein were selected by SELEX from an ssDNA library with a 45-nucleotide random region flanked by 20-nucleotide 5' and 3' fixed regions. The screening process was monitored by ELASA, which reflected the binding stringency between screened ssDNA library and target protein. As shown in Figure 2(a), the binding stringency between the ssDNA pool and GP73 gradually increased in small quantities before the fourth round ( $OD_{405} = 0.225 \pm 0.014$ ). However, the binding stringency rapidly increased after the sixth round ( $OD_{405} = 0.543 \pm 0.025$ ). There was no obvious difference in binding stringency between the eighth round ( $OD_{405} = 0.59 \pm 0.031$ ) and the tenth round

( $OD_{405} = 0.634 \pm 0.022$ ). The change of the binding stringency indicates that the ssDNA pool was enriched after the end of the screening process.

The ssDNA aptamer sequences, derived from the tenth enriched pool, were cloned into the pMD19-T plasmid, and thirty clones were picked for sequencing analysis. The results of sequence alignment showed that two clones were completely identical in nucleic acid sequence and the rate of reappearance was 6.7%, which was designated A10-2. The structure of aptamer A10-2 was predicted using one online program mFold, which yielded one potential secondary structure in the defined condition (Figure 2(c)). The aptamer A10-2 showed complex secondary structures, including protruding loops and stems. The Gibbs free energy (dG) of the aptamer was  $-5.1$ , suggesting that the aptamer A10-2 might maintain a rather stable structure.



### Clustal X (1.83) multiple sequence alignment

(b)

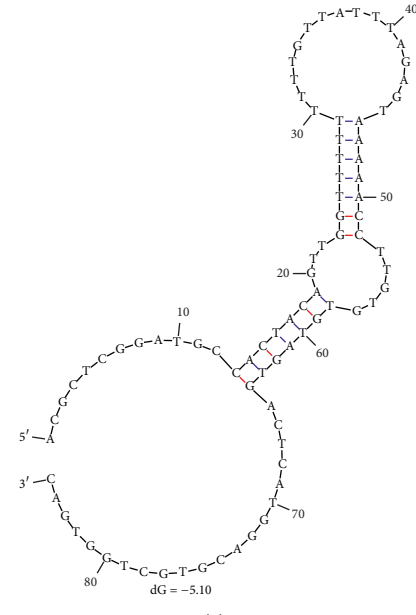


FIGURE 2: The SELEX screening of aptamers for GP73 and sequence analysis and structure prediction of aptamer A10-2. (a) The SELEX procession was monitored by ELASA. The binding capacity between selected ssDNA pool and GP73 was gradually increased with the increase of SELEX screening procession. (b) The encoding sequences of thirty aptamers derived from the tenth round of ssDNA pool were aligned and the sequences of two aptamers were the same, which were named A10-2. (c) The secondary structure and dG of A10-2 were analyzed using online mFold software. Asterisks indicate statistical significance: \* < 0.01 and \*\* > 0.05.

### 3.3. Binding Capacity of Aptamer A10-2 to Human GP73

**Protein.** In order to determine the binding capacity of A10-2 for GP73, the appropriate concentrations of GP73 were first determined in an ELASA assay. A series of concentrations of recombinant protein GP73 (from 31.25 ng/mL to 4  $\mu$ g/mL) were absorbed in microplate wells and incubated with Dig-labeled A10-2 and the quantity of A10-2 specifically binding to GP73 was determined after incubation with anti-Dig-ALP antibody. As shown in Figure 3(a), the aptamer A10-2 bound GP73 in a protein concentration-dependent manner and the binding capacity almost reached a plateau at the concentration of 2  $\mu$ g/mL of GP73. As far as the concentration of A10-2 in our experiment was concerned, the binding

capacity of A10-2 with GP73 changed most obviously in three consecutive concentrations of GP73 (2, 1, and 0.5  $\mu$ g/mL). In view of these results, the binding capacity of A10-2 for GP73 was determined under the condition of the three concentrations of GP73.

In order to determine the binding capacity of A10-2 for GP73 protein, the ELASA assay in which the 96-well plates were coated with three concentrations of GP73 protein was performed and a series of concentrations of Dig-labeled A10-2 were tested. Data were analyzed using nonlinear regression showing that they respond to a one-site binding curve with an equation  $y = (x \times B_{\max}) / (x + K_d)$ , where  $B_{\max}$  is the maximal binding and  $K_d$  is the concentration of ligand

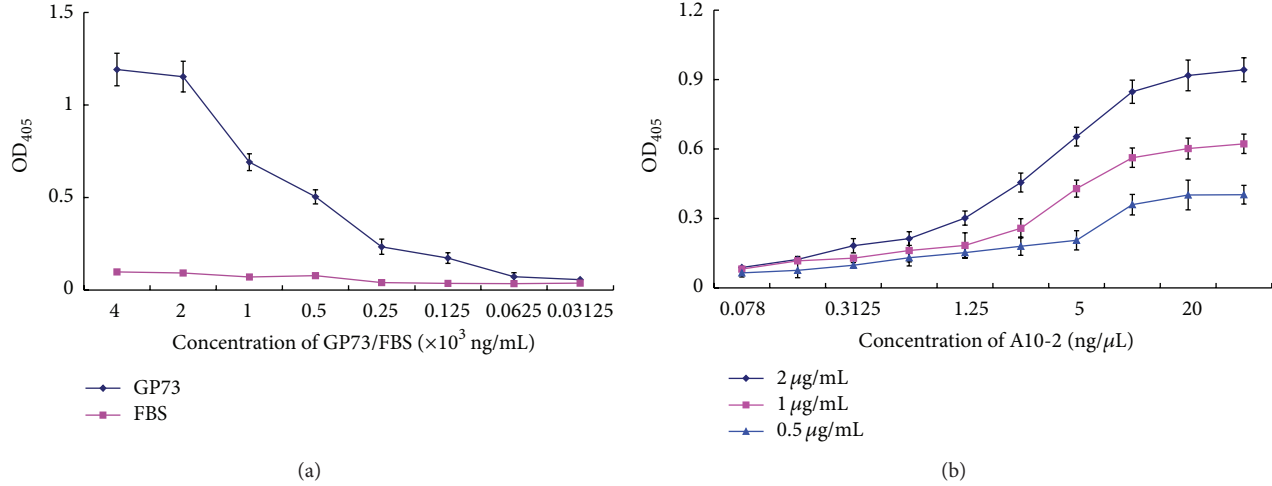


FIGURE 3: The binding capacity of A10-2 for GP73. (a) The recombinant protein GP73 was plated in a series of concentrations (31.25 ng/mL to 4  $\mu$ g/mL) and incubated with Dig-labeled A10-2. Finally, anti-Dig-ALP antibodies were added and revealed with PNPP solution at 405 nm. (b) Three concentrations of recombinant protein GP73 were plated and incubated with several concentrations (0.078–40 ng/ $\mu$ L) of Dig-labeled A10-2. Afterwards, anti-Dig-ALP antibodies were added and revealed as above. The  $K_d$  of A10-2 was calculated by nonlinear regression analysis. All experiments were performed in triplicate and repeated at least for three times.

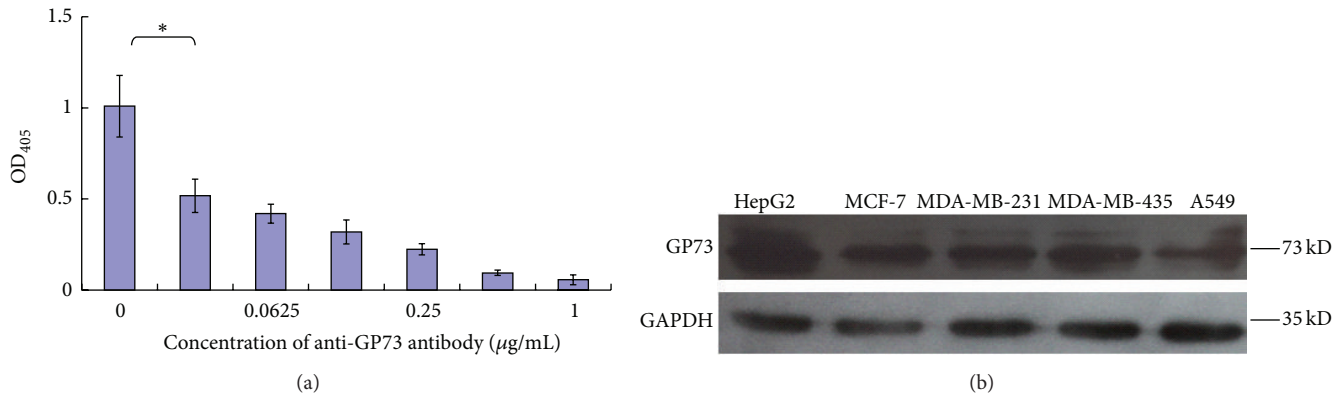


FIGURE 4: The specificity of A10-2 binding to GP73. (a) Before the Dig-labeled A10-2 was added and incubated with GP73-coated plate, the plate was first incubated with a series of concentrations of specific anti-GP73 antibody. Then the plate was continuously incubated with Dig-labeled A10-2 and revealed as above. (b) Biotin-labeled A10-2 recognized GP73 expressed in different tumor cell lines. All experiments were conducted in triplicate and repeated at least for three times. The asterisk indicates  $P < 0.01$ .

required to reach half-maximal binding. Data presented in Figure 3(b) indicated that A10-2 is able to detect GP73 protein in a concentration-dependent manner with  $K_d = 127.4 \pm 18.65$  nM.

**3.4. Binding Specificity of Aptamer A10-2 for Human GP73 Protein.** In order to determine the binding specificity of A10-2 to GP73, the specific anti-GP73 antibody was used to evaluate whether it could block the interaction between GP73 and A10-2. As shown in Figure 4(a), aptamer A10-2 could bind GP73 with high specificity while the binding capacity of A10-2 for GP73 dramatically declined when anti-GP73 antibody was first incubated with the coated GP73. At the same time, the binding capacity of A10-2 for GP73 was correspondingly decreased as anti-GP73 antibody concentration increased. In addition, A10-2 could replace anti-GP73 antibody to recognize GP73 protein in tumor cells

lines (Figure 4(b)). These results indicate that aptamer A10-2 is specific for GP73.

**3.5. Aptamer A10-2 Specially Recognizes GP73 in Human HCC Specimens.** In order to explore whether the A10-2 could be a potential probe to recognize tumor marker GP73 in vitro, we performed immunohistochemical staining in HCC specimens that had been pathologically confirmed. As shown in Figure 5, biotin-labeled A10-2 could clearly recognize GP73 in liver specimens. In normal liver tissue, GP73 was mainly located in the edge of liver bile duct. However, it was highly expressed in HCC tissue.

#### 4. Discussion

At present, the curative treatments of HCC are mainly determined by whether HCC could be diagnosed in the early stage.

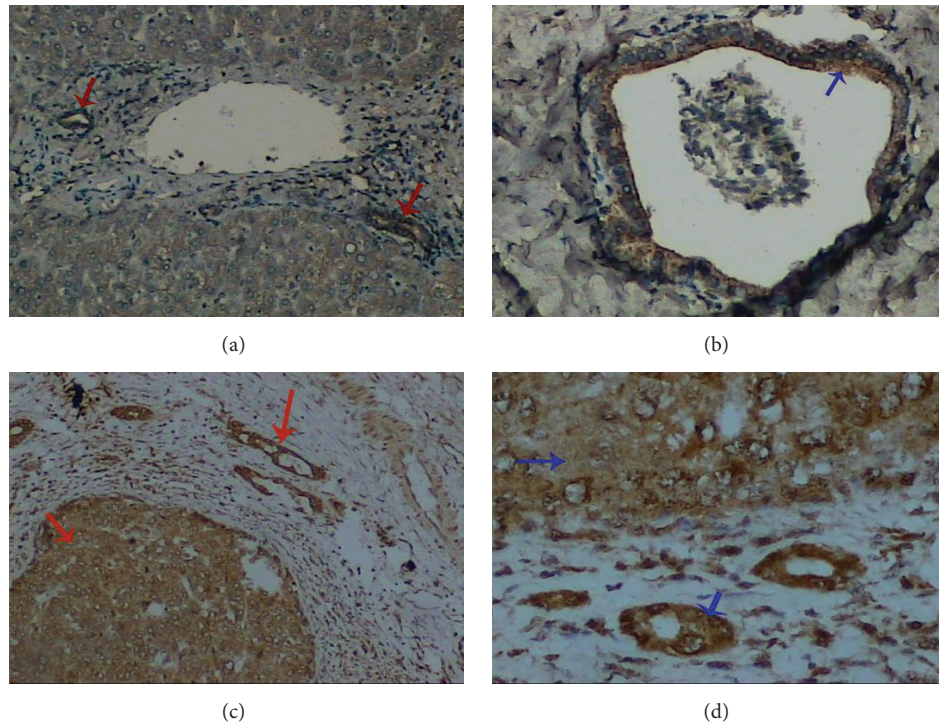


**FIGURE 5:** Detection of GP73 in human liver tissues by the aptamer A10-2. Tissue-specific GP73 expression was studied in normal liver and HCC tissues by indirect immunohistochemistry, in which Dig-labeled A10-2 were used as molecular probe. In normal tissue, GP73 is expressed in biliary epithelial cells ((a) and (b)). In HCC tissue, the hepatocytes and biliary epithelial cells were both strong stained ((c) and (d)). Arrows indicate the location of GP73. (a) and (c): original magnification 200x. (b) and (d): original magnification 400x. The results were the representations of 20 normal and HCC tissue samples.

Medical imaging exams and serum assay of alphafetoprotein (AFP) levels are the major ways to evaluate HCC. However, the sensitivity and specificity of AFP are not sufficient for clinical requirement and ultrasound examination could not find tumor with <1 cm diameter [16, 17]. As one new tumor marker of HCC, GP73 holds the promise for early diagnosis of HCC because the sensitivity and specificity of GP73 are both superior to those of AFP [18, 19].

In this study, we utilized GP73 as a target protein to screen specific ssDNA aptamers by SELEX technique. First, microgram levels of GP73 protein were expressed and purified by prokaryotic expression system and Nickel ion affinity chromatography, respectively. At the same time, the immunogenicity of purified GP73 was confirmed by the specific anti-GP73 antibody. The enriched ssDNA library with high binding capacity for GP73 was obtained after ten rounds of SELEX. Then, thirty ssDNA aptamers were sequenced and the nucleic acid sequences were aligned, in which two ssDNA aptamers with identical DNA sequence were confirmed, based on the alignment results, and designated as A10-2.

In the last decade, aptamers have been developed as biorecognition probes in different detection system [20, 21]. Whether A10-2 could be developed into one molecular probe to detect GP73 was further studied. The results of mFold analysis indicated that A10-2 may have a stable secondary structure because of the lower dG (-5.1). Then,

the equilibrium  $K_d$  was calculated by ELASA assay. The  $K_d$  value of A10-2 was in the range of  $\mu\text{M}$  to  $\text{nM}$  and is similar to many commercially available antibodies and others' reports [22, 23]. Interestingly, anti-GP73 antibody could block the binding of A10-2 to GP73, which might be due to the steric hindrance of the formed antigen-antibody complex. The specific binding of A10-2 to GP73 was also supported by the observation that several tumor cell lines exhibited variable expression level. Significantly, A10-2 could distinguish normal and cancerous liver tissues, where the biotin-labeled A10-2 staining was mainly located in the margin of normal liver bile duct. On the contrary, the biotin-labeled A10-2 staining was broadly distributed in the whole liver tissues of HCC patients. There are reports that GP73 was predominantly expressed by the epithelial lineage cells in normal liver and extensively expressed in HCC hepatocytes [24, 25]. The pattern of biotin-labeled A10-2 staining in liver tissues was consistent with the distribution of GP73 protein in liver tissues. These results demonstrate that A10-2 could specifically recognize GP73 and distinguish HCC tissues from normal live specimens.

In summary, we successfully obtained one ssDNA aptamer that can specifically bind HCC marker protein GP73 by SELEX technique. The identified aptamer A10-2 could specifically bind GP73 with high binding capacity. Moreover, the aptamer A10-2 might be developed into one molecular probe to detect HCC from normal liver specimens.

## Conflict of Interests

The authors declare that they have no conflict of interests.

## Acknowledgments

This research was supported by the Foundation of Science and Technology Commission of Guangdong Province of China (2013B021800309) and the Guangzhou Scientific Research Foundation of High School (1201430338).

## References

- [1] A. Jemal, F. Bray, M. M. Center, J. Ferlay, E. Ward, and D. Forman, "Global cancer statistics," *CA Cancer Journal for Clinicians*, vol. 61, no. 2, pp. 69–90, 2011.
- [2] H. B. El-Serag, A. C. Mason, and C. Key, "Trends in survival of patients with hepatocellular carcinoma between 1977 and 1996 in the United States," *Hepatology*, vol. 33, no. 1, pp. 62–65, 2001.
- [3] J. Bruix and M. Sherman, "Management of hepatocellular carcinoma: an update," *Hepatology*, vol. 53, no. 3, pp. 1020–1022, 2011.
- [4] M. Schwartz, S. Roayaie, and M. Konstadoulakis, "Strategies for the management of hepatocellular carcinoma," *Nature Clinical Practice Oncology*, vol. 4, no. 7, pp. 424–432, 2007.
- [5] Y. Zhou, L. Li, L. Hu, and T. Peng, "Golgi phosphoprotein 2 (GOLPH2/GP73/GOLM1) interacts with secretory clusterin," *Molecular Biology Reports*, vol. 38, no. 3, pp. 1457–1462, 2011.
- [6] R. Masuzaki, S. J. Karp, and M. Omata, "New serum markers of hepatocellular carcinoma," *Seminars in Oncology*, vol. 39, no. 4, pp. 434–439, 2012.
- [7] M.-C. Ba, H. Long, Y.-Q. Tang, and S.-Z. Cui, "GP73 expression and its significance in the diagnosis of hepatocellular carcinoma: a review," *International Journal of Clinical and Experimental Pathology*, vol. 5, no. 9, pp. 874–881, 2012.
- [8] B. Hu, X. H. Tian, J. Sun, and X. J. Meng, "Evaluation of individual and combined applications of serum biomarkers for diagnosis of hepatocellular carcinoma: a meta-analysis," *International Journal of Molecular Sciences*, vol. 14, no. 12, pp. 23559–23580, 2013.
- [9] Y. Mao, H. Yang, H. Xu et al., "Golgi protein 73 (GOLPH2) is a valuable serum marker for hepatocellular carcinoma," *Gut*, vol. 59, no. 12, pp. 1687–1693, 2010.
- [10] Y. X. Bao, Q. Cao, Y. Yang et al., "Expression and prognostic significance of Golgiglycoprotein73 (GP73) with Epithelial-Mesenchymal Transition (EMT) related molecules in Hepatocellular Carcinoma (HCC)," *Diagnostic Pathology*, vol. 8, article 197, 2013.
- [11] C. Tuerk and L. Gold, "Systematic evolution of ligands by exponential enrichment: RNA ligands to bacteriophage T4 DNA polymerase," *Science*, vol. 249, no. 4968, pp. 505–510, 1990.
- [12] A. D. Ellington and J. W. Szostak, "Selection in vitro of single-stranded DNA molecules that fold into specific ligand-binding structures," *Nature*, vol. 355, no. 6363, pp. 850–852, 1992.
- [13] P. R. Bouchard, R. M. Hutabarat, and K. M. Thompson, "Discovery and development of therapeutic aptamers," *Annual Review of Pharmacology and Toxicology*, vol. 50, pp. 237–257, 2010.
- [14] R. Nutiu and Y. Li, "Aptamers with fluorescence-signaling properties," *Methods*, vol. 37, no. 1, pp. 16–25, 2005.
- [15] M. Zuker, "Mfold web server for nucleic acid folding and hybridization prediction," *Nucleic Acids Research*, vol. 31, no. 13, pp. 3406–3415, 2003.
- [16] A. S. Lok, R. K. Sterling, J. E. Everhart et al., "Des- $\gamma$ -carboxy prothrombin and  $\alpha$ -fetoprotein as biomarkers for the early detection of hepatocellular carcinoma," *Gastroenterology*, vol. 138, no. 2, pp. 493–502, 2010.
- [17] C. M. Sturgeon, M. J. Duffy, B. R. Hofmann et al., "National academy of clinical biochemistry laboratory medicine practice guidelines for use of tumor markers in liver, bladder, cervical, and gastric cancers," *Clinical Chemistry*, vol. 56, no. 6, pp. e1–e48, 2010.
- [18] J. A. Marrero, P. R. Romano, O. Nikolaeva et al., "GP73, a resident Golgi glycoprotein, is a novel serum marker for hepatocellular carcinoma," *Journal of Hepatology*, vol. 43, no. 6, pp. 1007–1012, 2005.
- [19] C. D. M. Witjes, S. M. van Aalten, E. W. Steyerberg et al., "Recently introduced biomarkers for screening of hepatocellular carcinoma: a systematic review and meta-analysis," *Hepatology International*, vol. 7, no. 1, pp. 59–64, 2013.
- [20] J. Zhou, M. R. Battig, and Y. Wang, "Aptamer-based molecular recognition for biosensor development," *Analytical and Bioanalytical Chemistry*, vol. 398, no. 6, pp. 2471–2480, 2010.
- [21] B. Soontornworajit and Y. Wang, "Nucleic acid aptamers for clinical diagnosis: cell detection and molecular imaging," *Analytical and Bioanalytical Chemistry*, vol. 399, no. 4, pp. 1591–1599, 2011.
- [22] B. I. Escudero-Abarca, S. H. Suh, M. D. Moore, H. P. Dwivedi, and L.-A. Jaykus, "Selection, characterization and application of nucleic acid aptamers for the capture and detection of human norovirus strains," *PLoS ONE*, vol. 9, no. 9, Article ID e106805, 2014.
- [23] F.-B. Wang, Y. Rong, M. Fang et al., "Recognition and capture of metastatic hepatocellular carcinoma cells using aptamer-conjugated quantum dots and magnetic particles," *Biomaterials*, vol. 34, no. 15, pp. 3816–3827, 2013.
- [24] R. D. Kladney, G. A. Bulla, L. Guo et al., "GP73, a novel Golgi-localized protein upregulated by viral infection," *Gene*, vol. 249, no. 1-2, pp. 53–65, 2000.
- [25] A. Zhang and B. Cao, "Generation and characterization of an anti-GP73 monoclonal antibody for immunoblotting and sandwich ELISA," *The Journal of Biomedical Research*, vol. 26, no. 6, pp. 467–473, 2012.

## Research Article

# PI3K/AKT/mTOR/p70S6K Pathway Is Involved in A $\beta$ 25-35-Induced Autophagy

Shengnuo Fan,<sup>1</sup> Bei Zhang,<sup>2</sup> Ping Luan,<sup>3</sup> Beibei Gu,<sup>4</sup> Qing Wan,<sup>5</sup> Xiaoyun Huang,<sup>6</sup> Wang Liao,<sup>1</sup> and Jun Liu<sup>1</sup>

<sup>1</sup>Department of Neurology, Sun Yat-sen Memorial Hospital, Sun Yat-sen University, Guangzhou 510120, China

<sup>2</sup>Department of Neurology, The First Affiliated Hospital, Guangdong Pharmaceutical University, Guangzhou 510080, China

<sup>3</sup>Medical School, Shenzhen University, Shenzhen, Guangdong 518060, China

<sup>4</sup>Department of Anesthesiology, Sun Yat-sen Memorial Hospital, Sun Yat-sen University, Guangzhou 510120, China

<sup>5</sup>Department of Rehabilitation Medicine, Sun Yat-sen Memorial Hospital, Sun Yat-sen University, Guangzhou 510120, China

<sup>6</sup>Department of Neurology, Houjie Hospital, Dongguan 511711, China

Correspondence should be addressed to Jun Liu; docliujun@hotmail.com

Received 8 May 2015; Revised 17 July 2015; Accepted 4 August 2015

Academic Editor: Lap Ho

Copyright © 2015 Shengnuo Fan et al. This is an open access article distributed under the Creative Commons Attribution License, which permits unrestricted use, distribution, and reproduction in any medium, provided the original work is properly cited.

Disruption or deregulation of the autophagy system has been implicated in neurodegenerative disorders such as Alzheimer's disease (AD). A $\beta$  plays an important role in this autophagic system. In many cases, autophagy is regulated by the phosphatidylinositol 3-phosphate kinase/AKT/mammalian target of rapamycin/p70 ribosomal protein S6 kinase (PI3K/AKT/mTOR/p70S6K) signaling pathway. However, whether this signaling pathway is involved in A $\beta$ -induced autophagy in neuronal cells is not known. Here, we studied whether A $\beta$ 25-35 induces autophagy in HT22 cells and C57 mice and investigated whether PI3K is involved in the autophagy induction. We found that A $\beta$ 25-35 inhibited HT22 cell viability in a dose- and time-dependent manner. A $\beta$ 25-35 induced autophagosome formation, the conversion of microtubule-associated protein light chain 3 (LC3), and the suppression of the mTOR pathway both in vitro and in vivo. Furthermore, A $\beta$ 25-35 impaired the learning abilities of C57 mice. Our study suggests that A $\beta$ 25-35 induces autophagy and the PI3K/AKT/mTOR/p70S6K pathway is involved in the process, which improves our understanding of the pathogenesis of AD and provides an additional model for AD research.

## 1. Introduction

Macroautophagy (autophagy) is a phylogenetically conserved activity that occurs in organisms from yeast to mammals in which damaged organelles and misfolded proteins are degraded and recycled for the maintenance of a healthy cellular environment [1]. In addition to its importance in maintaining cell homeostasis by clearing damaged organelles and waste proteins, autophagy plays roles in many pathological processes, including the degradation of aggregating proteins in neurodegenerative diseases. Disruption or deregulation of the autophagy system has been implicated in neurodegenerative disorders such as Alzheimer's disease (AD) [2].

AD is a devastating disorder that leads to cognitive, behavioral, and memory deficits. The hallmarks of AD are

the superfluous accumulation of beta-amyloid (A $\beta$ ) into senile plaques and hyperphosphorylated tau into neurofibrillary tangles and neuronal loss in select brain areas involved in learning and memory. It is generally accepted that the excessive A $\beta$  peptide deposition that leads to synapse and neuronal cell loss is involved in AD pathogenesis [3]. A $\beta$  is cleaved from amyloid- $\beta$  protein precursor (APP) and comprises a set of 39–43-residue polypeptides that exert a range of neurotoxic effects that are considered to be important to the evolution of AD [4]. Emerging evidence has shown that A $\beta$ -induced autophagy plays an important role in AD [5, 6].

In mammalian cells, the phosphatidylinositol 3-phosphate kinase/AKT/mammalian target of rapamycin/p70 ribosomal protein S6 kinase (PI3K/AKT/mTOR/p70S6K) signaling pathway is the primary pathway that regulates autophagy when cells are exposed to certain conditions, such

as starvation, oxidative stress, infection, and tumor suppression [7]. However, whether the PI3K/AKT/mTOR/p70S6K signaling pathway is involved in A $\beta$ -induced autophagy in neuronal cells is not yet fully understood.

In the present work, we used immortalized murine hippocampal neurons (HT22 cells), which possess functional cholinergic properties when differentiated [8–10], as a cell model to study whether A $\beta$  exposure induces autophagy. Among all A $\beta$  fragments used in scientific researches, A $\beta$ 25–35 is the shortest active fragment that showed similar neurotoxicity effect to a full-length A $\beta$ . Considering A $\beta$ 25–35 can be easily synthesized, we choose this fragment as reagent in the study [11]. Additionally, we examined the morphocytological changes in mouse hippocampal cells after the intracerebroventricular administration of A $\beta$ 25–35. We further investigated whether the PI3K/AKT/mTOR/p70S6K pathway was involved in these autophagic processes. Our findings provide valuable information about the mechanism of the regulation of autophagy in AD pathogenesis.

## 2. Materials and Methods

**2.1. Reagents and Antibodies.** Dulbecco's modified Eagle's medium (DMEM), fetal bovine serum (FBS), neurobasal medium, and N2 supplement were obtained from Gibco (New York, USA). A $\beta$ 25–35 was synthesized by Shanghai Sangon Biological Engineering Technology & Services Co., Ltd. A cell counting kit-8 (CCK-8) was acquired from Dojin Laboratories (Kumamoto, Kyushu, Japan). DAPI was obtained from Invitrogen/Life Technologies (Carlsbad, CA, USA). The antibodies anti-phospho-AKT (Ser473), anti-AKT, anti-p70S6K, anti-p-p70S6K, and anti-tubulin and secondary antibody horseradish peroxidase- (HRP-) conjugated goat anti-rabbit IgG were obtained from Cell Signaling Technology (USA). Anti-LC3 was acquired from the MBL International Corporation. The Western blot chemiluminescent horseradish peroxidase substrate was purchased from Millipore (USA). All other experimental supplies and reagents were purchased from Invitrogen, Thermo Fisher, and MR Biotech.

**2.2. Cell Culture, Differentiation, A $\beta$  Preparation, and Treatment.** HT22 cells were maintained in DMEM supplemented with 10% FBS as previously described [8, 10] and differentiated in neurobasal medium containing 1 × N2 supplement for 24–48 h before use [9]. A $\beta$ 25–35 was diluted in sterile saline at a concentration of 0.5 mM and was maintained at 37°C for 7 days to pre-age the peptide [11]. The aged A $\beta$  solution was diluted to different concentrations before treatment. Bafilomycin A1 (100 nM) and rapamycin (1  $\mu$ M) were used accordingly. Different concentrations of A $\beta$ 25–35 were added to the HT22 cells for various times.

**2.3. Cell Viability Assay.** The viabilities of the HT22 cells were evaluated by CCK-8. Briefly, after the treatment of the different groups, 10  $\mu$ L/well of CCK-8 reagent was added to the cells, which were then incubated for 1.5 h at 37°C with 5% CO<sub>2</sub> in dark conditions. The optical density (OD) was

measured at an absorbance wavelength of 450 nm with a multifunctional microplate reader (SpectraMax M5, USA).

**2.4. Immunofluorescence Assay.** The appropriate concentrations (10 and 40  $\mu$ M) of A $\beta$  as determined with the CCK-8 test were used in the cultured HT22 cells for 24 h with or without bafilomycin A1. Rapamycin (1  $\mu$ M) was chosen as a positive control. The different groups were fixed in 4% paraformaldehyde for 15 min at room temperature and then permeabilized with 0.25% triton X-100 for 10 min. After blocking with 1% bovine serum albumin in PBS for 30 min, the samples were incubated with anti-LC3 (1:500) overnight at 4°C in a humidified chamber. After washing three times in PBS, incubating for 60 min with HRP-conjugated goat anti-rabbit IgG, and repeating the three washes, the samples were stained with DAPI for 5 min. Images were acquired with an upright immunofluorescence microscope (BX51WI, Olympus, USA).

**2.5. Mice and A $\beta$  Intracranial Injection.** All experiments were carried out in accordance with guidelines approved by ethical committee of Sun Yat-sen University, which includes minimizing the number of animals used and their suffering.

A total of 24 male 6-month-old C57BL/6J mice weighing 28.1 ± 1.4 g were used in this study. There were no significant changes in body weight between or within the groups of mice. The 24 mice were randomly divided into three groups of 8 mice each that were treated with sterile saline, low-dose A $\beta$ , and high-dose A $\beta$  group. The animal care and the experimental procedures of this study were approved by the Animal Care and Ethics Committee at Sun Yat-sen University, China.

The pre-aged A $\beta$ 25–35 was diluted to 2  $\mu$ g/ $\mu$ L with sterile saline before injection. A $\beta$ 25–35 was administered intracerebroventricularly (i.c.v.). Immediately before surgery, the mice were weighed and then anaesthetized with 10% chloral hydrate. A stereotaxic apparatus (Wood Dale, IL, USA) was used. Burr holes were made to access the hippocampus using the following previously determined coordinates relative to the bregma: anteroposterior, -1.5 mm; lateral, -1.0 mm; and vertical, 2.0 mm. The injections were performed with a Hamilton microsyringe equipped with a 3 mm needle. The injections were administered as follows: Group A received sterile saline (0.6  $\mu$ L); Group B received low-dose A $\beta$ 25–35 (0.3  $\mu$ L); and Group C received high-dose A $\beta$ 25–35 (0.6  $\mu$ L). The injection time was 5 min, and the needle was maintained at the injection site for 2 min prior to slow withdrawal.

**2.6. Behavioral Testing.** Spatial learning and memory functions were assessed with the Morris Water Maze (MWM) 2 weeks after the injections. The procedure consisted of 1 day of adaptation tests without a platform and 5 days of hidden platform tests plus a spatial probe test that was performed 24 h after the last hidden platform test. For each trial, the mouse was allowed to swim to find the hidden platform for a maximum of 60 s. The animals that did not find the platform within this time limit were guided to the platform and kept there for 15 s. The animals were given 4 trials per day. The intertrial interval was 15 min. The distal start positions

were semirandomly selected. The time required to find and climb onto the platform was recorded as the latency. The probe trial was performed 24 h after the last acquisition test. During the probe trials, the platform was removed, and the mice were free to swim in the water for 60 s. The numbers of crossings of the platform location and the time spent in the target quadrant were measured to assess the acquisition measurement of the water maze task.

**2.7. Transmission Electron Microscopy (TEM).** Upon the completion of behavioral testing, the mice were perfused with 4% paraformaldehyde. The brains were rapidly removed and fixed in ice-cold glutaraldehyde (3% in 0.1 M PBS, pH 7.4) for 1 h. The hippocampal samples were cut into 2 mm<sup>3</sup> pieces and postfixed 1% osmium tetroxide in PBS for 1 h at 4°C, processed through a graded series of acetone, embedded in Araldite, and polymerized overnight at 60°C. Thin sections (60 nm) were collected on formvar-coated, single-slot grids, stained with uranyl acetate and lead citrate, and then viewed on a FEI Tecnai G2 Spirit TWIN transmission electron microscope (OR, USA).

**2.8. Western Blot Analysis.** The HT22 cells were exposed to various conditions for various durations and were then washed gently with PBS twice and lysed with RIPA lysis buffer. Hippocampal samples from the mice in each group were collected after the completion of the behavioral testing. The tissues were homogenized using 10 up-and-down strokes of a prechilled Teflon-glass homogenizer in lysis buffer. The lysates were then sonicated and centrifuged. Subsequent to boiling and denaturing, the cell and tissue protein samples (30 µg) were subjected to 12% SDS-polyacrylamide gel electrophoresis and transferred to a PVDF membrane (Millipore, USA). After blocking with 5% nonfat milk, the membranes were incubated with the following primary antibodies overnight at 4°C: anti-phospho-AKT (1:1,000), anti-AKT (1:1,000), anti-phospho-p70S6K (1:1,000), anti-p70S6K (1:1,000), anti-LC3 (1:1,000), and anti-Tubulin (1:2,000). After washing with TBST three times, the membranes were incubated with anti-rabbit secondary antibodies (dilution, 1:2,000) for 60 min. The washings were then repeated. The membranes were incubated with horseradish peroxidase substrate for 5 min, and the fluorescence bands were detected with X-ray films. The intensities of the bands were quantified with a Gel-Pro Analyzer (Media Cybernetics Inc., USA).

**2.9. Statistical Analyses.** SPSS 13.0 software (SPSS Inc., Chicago, IL, USA) was used for the data processing. All of the data are expressed as the mean ± the standard error (SE). One-way ANOVAs with post hoc tests or *t*-tests were used for the statistical analyses. *P* < 0.05 was required for results to be considered statistically significant.

### 3. Results

**3.1. Aβ25-35 Decreased Cell Viability in a Dose- and Time-Dependent Manner.** When the HT22 cells were treated with increasing doses of Aβ25-35 for 24 h, the viabilities of the

HT22 cells decreased. As shown in Figure 1, Aβ25-35 significantly inhibited the growth of HT22 cells at doses greater than or equal to 40 µM (*P* < 0.05), and 40 µM Aβ25-35 resulted in remarkably increased cytotoxicity in the HT22 cells at various times ranging from 24 h to 48 h (*P* < 0.05). The autophagy inhibitor baflomycin A1 significantly exacerbated Aβ25-35 cytotoxicity, and the autophagy activator rapamycin had the opposite effect. Neither baflomycin A1 nor rapamycin exhibited significant toxicity to the HT22 cells when applied alone. We selected 40 µM as the optimal concentration of Aβ25-35 for the subsequent experiments.

**3.2. Aβ25-35 Induced Autophagosome Formation.** Punctate LC3 staining was observed in the perinuclear regions in the various groups. After Aβ25-35 treatment for 24 h, LC3 immunostaining was evaluated with an immunofluorescence microscope, and the presence of autophagosomes was detected by the visualization of punctate dots. As shown in Figure 2, 40 µM Aβ25-35 induced a greater number of punctate dots than 10 µM. The combination of Aβ25-35 and baflomycin A1 produced more dots than Aβ25-35 alone. Rapamycin (RP, 1 µM) served as a positive control.

**3.3. Intracranial Injection of Aβ25-35 Impaired the Learning Abilities of C57 Mice.** Two weeks after the intracranial injections of Aβ25-35, the MWM test was conducted to evaluate the learning and memory abilities of the mice. In the hidden-platform tests, the latencies diminished across training days in all the three groups. As shown in Figure 3, saline group exhibited lower escape latencies (Figure 3(a)) than Aβ25-35 groups across the successive days of training. Compared to low-dose group, high-dose group behaved worse, which indicated a dose-dependent effect of Aβ25-35. Probe trials were performed 24 h after the final place navigation tests. The numbers of platform area crossings and times spent in the target quadrant during the 60 s trials (Figures 3(b) and 3(c)) revealed that saline group performed significantly better than Aβ25-35 groups. Dose-dependent effects were also manifested in these measurements.

**3.4. Intracranial Injection of Aβ25-35 Induced a Large Accumulation of Autophagic Vesicles (AVs).** TEM revealed a large accumulation of autophagic vesicles (AVs) in the hippocampus 2 weeks after the injection of Aβ25-35. As depicted in Figure 3(d), there was extensive accumulation of AVs in the axons of Aβ25-35 groups. Compared to low-dose group, high-dose group exhibited a greater number of AVs, which indicated a dose-dependent effect. In contrast, autophagosomes were rarely observed in the neurons of saline group.

**3.5. PI3K/AKT/mTOR/p70S6K Pathway Is Involved in Aβ25-35-Induced Autophagy.** In vitro, we first detected the protein expressions of microtubule-associated protein light chain 3 in the HT22 cells (LC3) following Aβ25-35 (40 µM) treatment for various times and following Aβ25-35 treatment at different concentrations for 24 h. Consequently (Figure 4(a)), the conversion of the LC3 soluble form (LC3-I) into the autophagosome-associated form (LC3-II) (i.e., the LC3-II/I ratio) increased as the treatment time increased

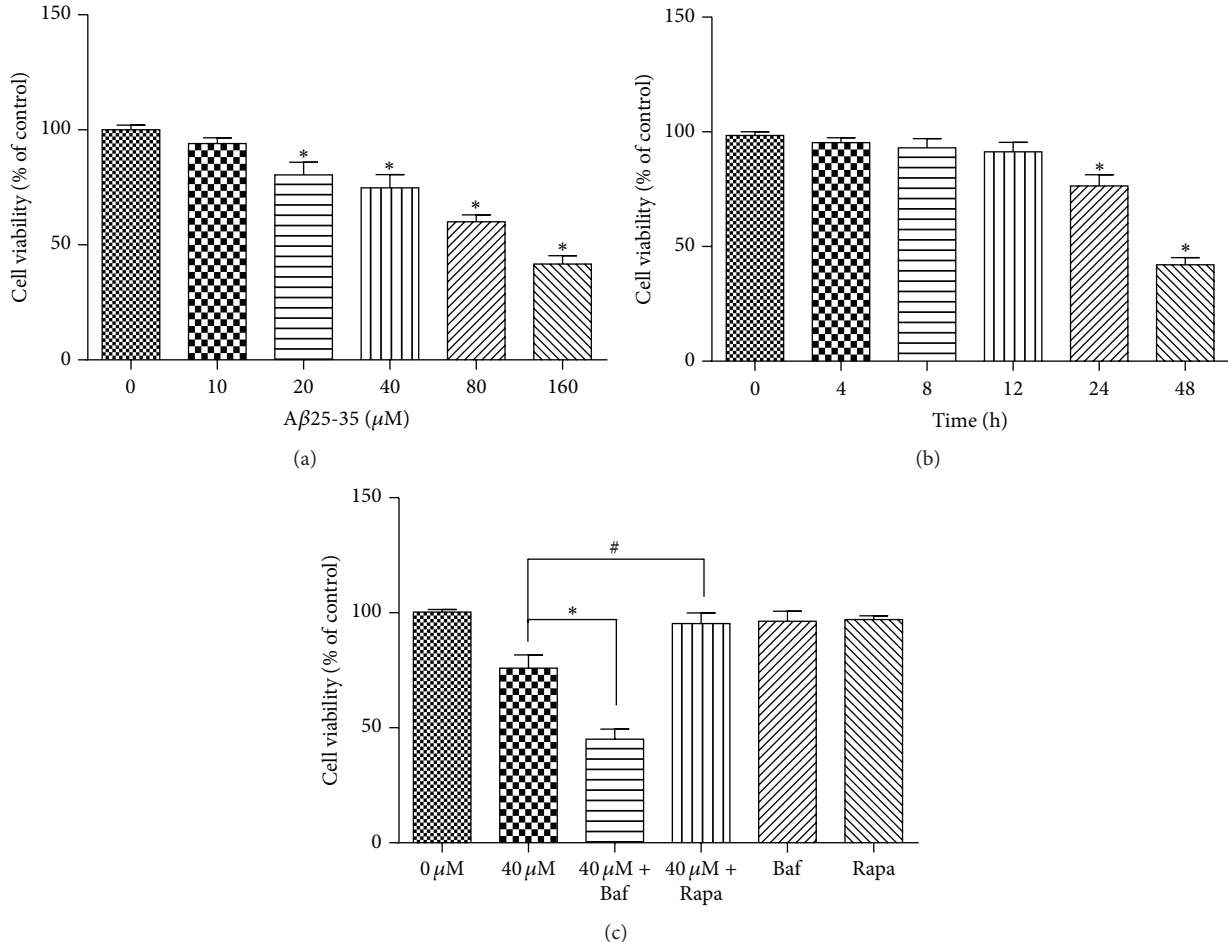


FIGURE 1:  $A\beta$ 25-35 inhibited the growth of HT22 cells. The viabilities of the HT22 cells incubated with (a) various doses of  $A\beta$ 25-35 for 24 h, (b) 40  $\mu$ M  $A\beta$ 25-35 for various times, and (c) 40  $\mu$ M  $A\beta$ 25-35 with bafilomycin A1 or rapamycin were evaluated with CCK8 assays. \*#  $P < 0.05$ .

from 0 h to 48 h. The 40  $\mu$ M  $A\beta$ 25-35 treatment resulted in a greater increase in this ratio than the 10  $\mu$ M  $A\beta$ 25-35 treatment (Figure 4(b)). We next examined whether the PI3K/AKT/mTOR/p70S6K pathway was involved in this process by analyzing the levels of phosphorylated p70S6K and AKT (Figure 4(b)). We found that  $A\beta$ 25-35 remarkably decreased the levels of phosphorylated p70S6K and AKT compared to the nontreated group.

In vivo, an augmentation of the LC3-II/I ratio and reductions in p70S6K and AKT were also detected following the injections of  $A\beta$ 25-35 (Figure 4(c)).

Together, our results indicated that  $A\beta$ 25-35 treatment inhibited HT22 cell viability in a dose- and time-dependent manner and dose-dependently impaired the learning abilities of the C57 mice.  $A\beta$ 25-35 treatment induced autophagy and PI3K/AKT/mTOR/p70S6K pathway is involved in this autophagic activity.

#### 4. Discussion

According to the amyloid cascade hypothesis,  $A\beta$  is a major etiological agent that causes devastating neurotoxicity, including oxidative stress, unbalanced calcium levels,

neurofibrillary tangles, inflammatory reactions, synaptic dysfunction, and hippocampal neuron loss [12, 13]. Our previous work [14], together with a substantial volume of in vitro and in vivo research from around the world, has verified the toxicity of  $A\beta$  [15, 16]. The present study also revealed that  $A\beta$ 25-35 inhibited HT22 cell viability in a dose- and time-dependent manner. Numerous studies have proven that the amelioration of this neurotoxicity and anti- $A\beta$  strategies improve neuronal survival, spatial memory, synaptic plasticity, and calcium homeostasis in AD models [17–19]. Therefore, the goal of achieving  $A\beta$  clearance is of great significance to AD therapy.

Autophagy has been indicated to play an important role in the pathogenesis of AD [2, 20], which occurs extensively in transgenic mouse models that overexpress  $A\beta$  [21] and in vitro models [22, 23]. In our work, we successfully induced autophagy via the treatment of HT22 cells and C57 mice with  $A\beta$ 25-35. Using generally accepted markers of autophagy [24], that is, LC3 punctate dot immunofluorescent, AV detection via TEM, and the LC3 II/I ratio, our research identified the formation of autophagosomes. Autophagy is recognized as a double-edged sword in the regulation of health and disease [20]. Emerging evidence shows that hyperactive

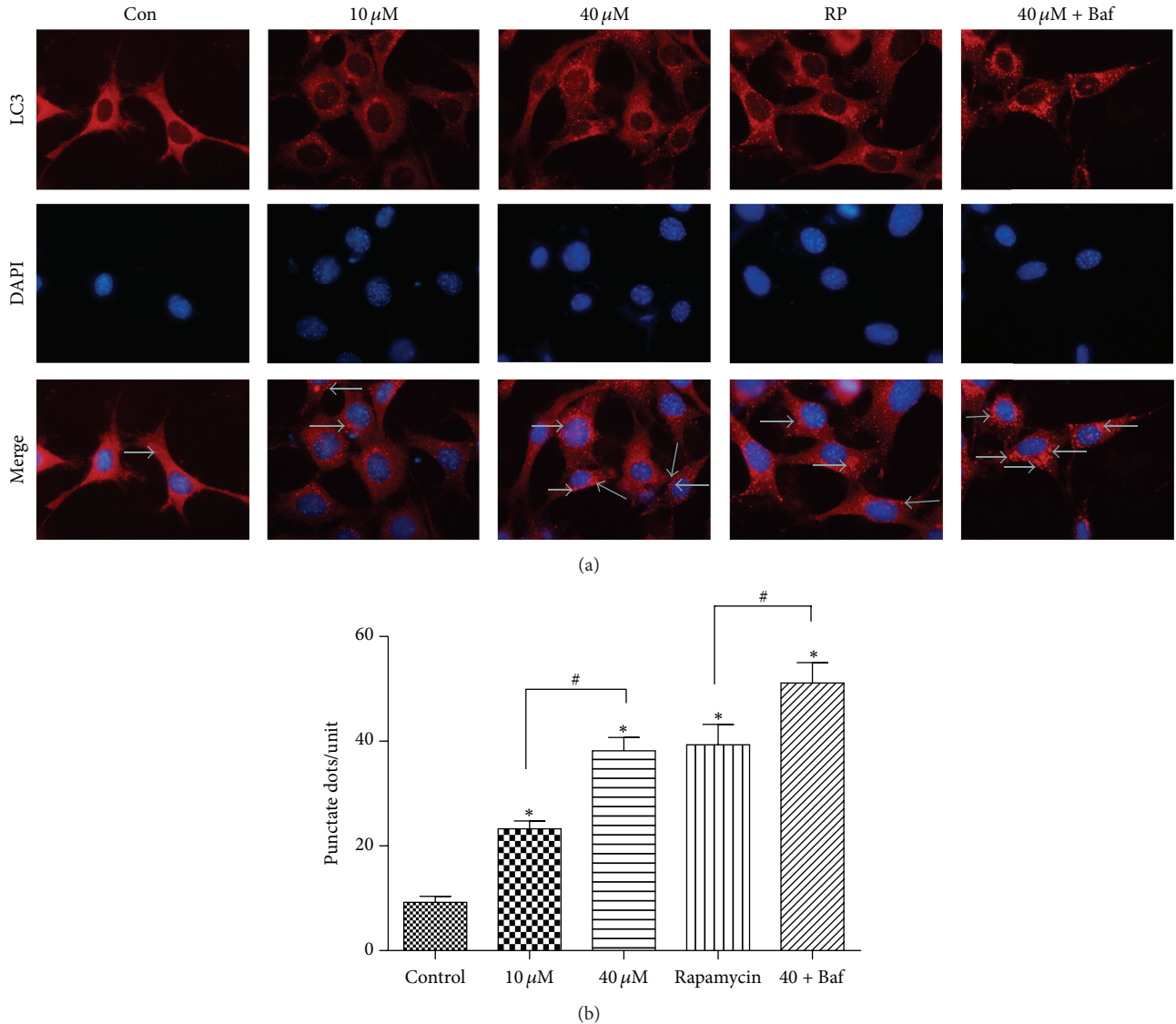


**FIGURE 2:** LC3 immunoreactivity is shown. HT22 cells were stained for LC3 (red arrows) and with the nuclear dye DAPI (blue) following the different treatments for 24 h. (Control) Negative control group: LC3 punctate dots (red) can barely be detected. (10  $\mu$ M) 10  $\mu$ M A $\beta$ 25-35 group: the dots exhibited a scattered distribution in the perinuclear region. (40  $\mu$ M) 40  $\mu$ M A $\beta$ 25-35 group: the dots are evenly spread around the perinuclear and cytoplasm regions. (RP) rapamycin group. (40  $\mu$ M + Baf) 40  $\mu$ M A $\beta$ 25-35 and bafilomycin A1 (Baf, 100 nM) group: the cells are filled with cluster-like dots. \*#  $P < 0.05$ .

autophagy is harmful to neuron survival. The inhibition of certain autophagic activities might prevent neurite degeneration [25]. Interestingly, regarding AD research, autophagy has been proven to be beneficial in most cases [16, 26, 27]. Hence, we presume that the autophagy induced by A $\beta$ 25-35 might act as a self-defense mechanism via the intracellular clearance of peptide deposits and the cellular organelles that are damaged by neurotoxicity. The upregulation of autophagy might protect against the neuronal degeneration that is induced by A $\beta$ 25-35 exposure. Recent studies have shown that enhancing autophagy with rapamycin rescues AD-like pathology and cognitive deficits in murine AD models [26, 27] and that blocking autophagy aggravates neurite degeneration [28]. The results of these studies are consistent with our findings.

However, sufficient and appropriate autophagy is required for proper function because pathologic autophagy also occurs. Compared to nondemented groups, heavy accumulations of autophagosomes are present in the AD cortex and hippocampus. The accumulation of autophagosomes in AD might be due to the stimulation of autophagy or a residually slow rate of autophagosome formation combined with a failure to complete sufficient lysosomal fusion and digestion [29]. Thus, there should be an equilibrium point in the modulation of autophagy. Recent research has indicated that primary lysosomal dysfunction causes cargo-specific deficits in axonal transport that lead to Alzheimer's-like neuritic dystrophy [30]. Therefore, it is possible that the deposition of A $\beta$  leads to a dysfunction of lysosomal proteolysis that would account for

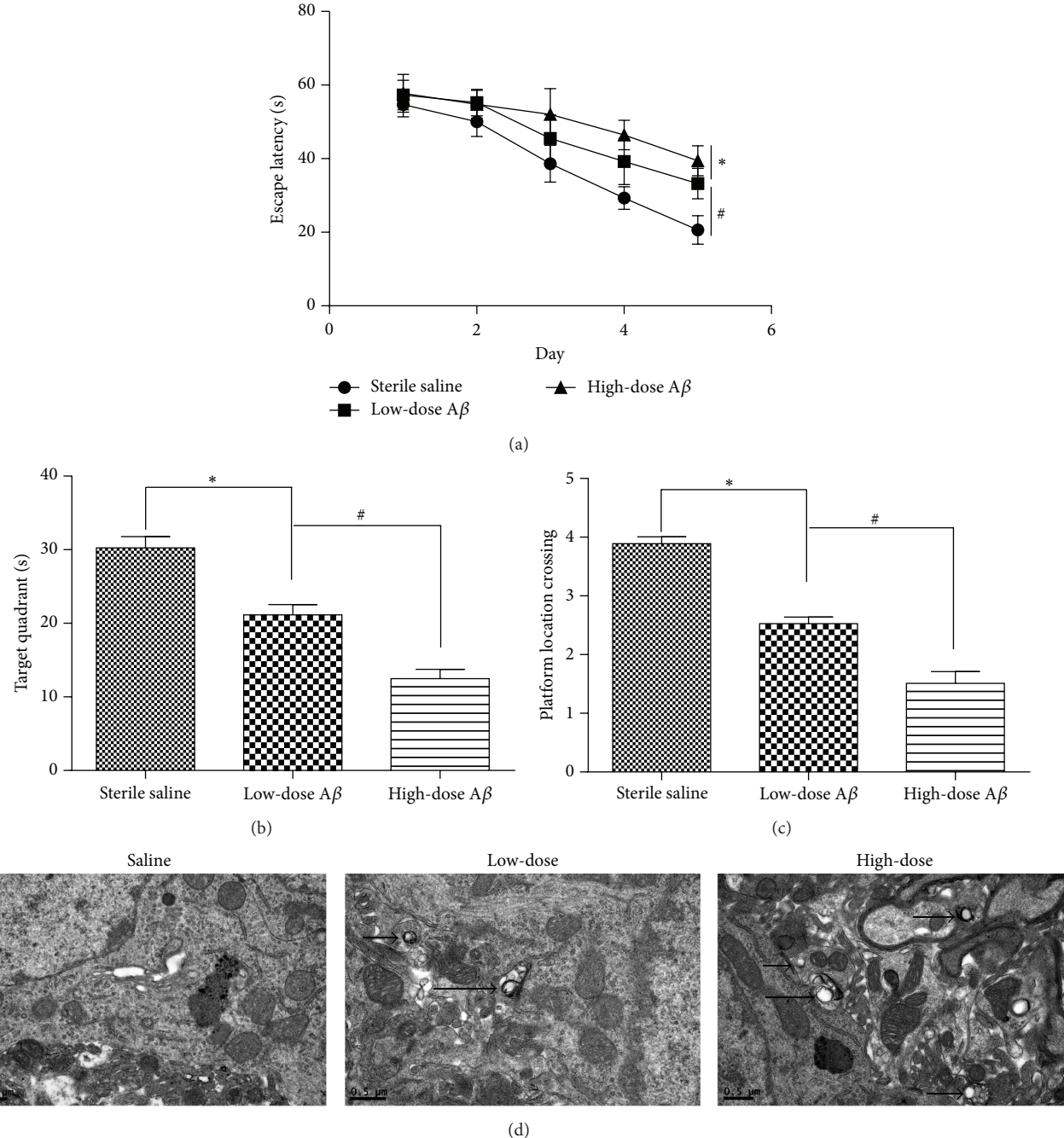


FIGURE 3: Intracranial injection of A $\beta$ 25-35 impaired the learning abilities of C57 mice in the MWM. (a) The mean escape latencies of the mice in the place navigation test. (b) The numbers of platform area crossings in the probe trials. (c) The times spent in the target quadrant in the probe trials. (d) Representative ultrastructural appearance of autophagic vacuoles (AVs, arrows) in mice hippocampus of each group. As shown in TEM pictures of saline group, there was barely any accumulation of autophagic vesicle in axons. Low-dose A $\beta$ 25-35 group showed significant accumulation of AVs, while high-dose A $\beta$ 25-35 group depicted more AVs than low-dose group. \*\*#  $P < 0.05$ .

the accumulation of autophagic structures. However, further study is needed to understand this autophagic system.

The function of mTOR is primarily mediated by mTOR complex 1 (mTORC1) and mTORC2. mTORC1 is a major negative regulator of autophagy and is also a key homeostatic regulator of cell growth, proliferation, and survival [31]. As the major upstream modulator, the PI3K pathway regulates

autophagy by phosphorylating AKT at serine residue 473 (Ser473), which influences the downstream elements p70S6K and 4E-BP1 [32]. The PI3K/AKT/mTOR/p70S6K pathway plays a vital role in the central nervous system (CNS), particularly in synaptic development and function [33, 34]. Dysregulation of the PI3K/AKT/mTOR/p70S6K pathway has commonly been reported in the brains of AD patients,

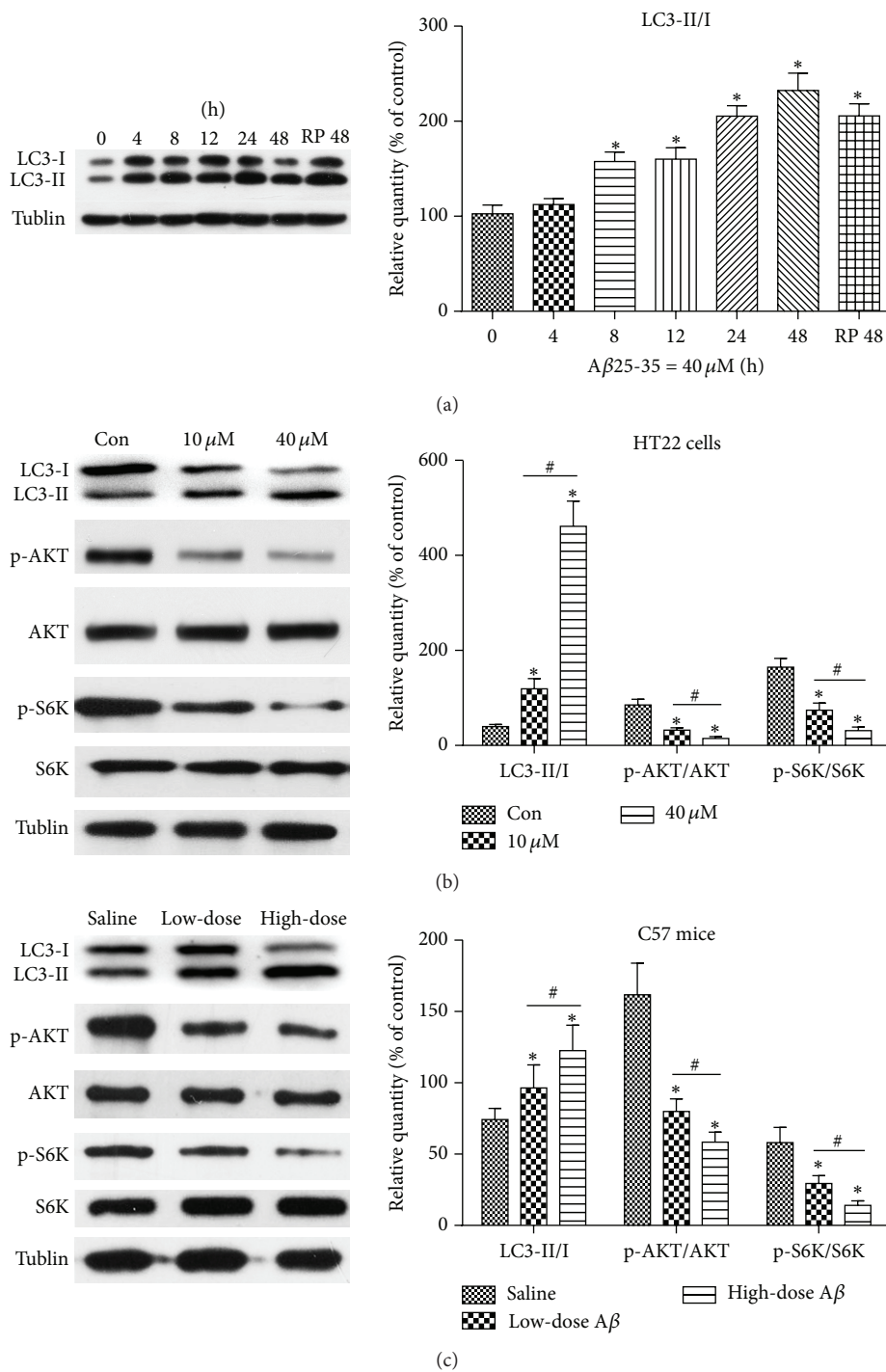


FIGURE 4: The effects of A $\beta$ 25-35 treatment on the LC3 II/I ratio and the levels of phosphorylation of AKT and p70S6K (S6K) in HT22 cells and C57 mice. (a) HT22 cells were treated with 40  $\mu$ M A $\beta$ 25-35 for various times ranging from 0 h to 48 h. Rapamycin (1  $\mu$ M, 48 h) served as a positive control. (b) The HT22 cells were divided into an untreated group, a 10  $\mu$ M A $\beta$ 25-35 group, and a 40  $\mu$ M A $\beta$ 25-35 group and treated for 24 h. The column graphs below the panels depict the relative expressions of LC3 II/I and phosphorylated AKT and p70S6K (S6K). (c) The mice were intracerebroventricularly administered sterile saline, low-dose A $\beta$ 25-35 (0.3  $\mu$ L), or high-dose A $\beta$ 25-35 (0.6  $\mu$ L). The expressions of Tubulin confirmed equal protein loading. \*#  $P < 0.05$ .

and both hypoactivation and hyperactivation are linked to autophagy disruptions related to the pathology of AD [35, 36]. In our study, we found that A $\beta$ 25-35 remarkably decreased the levels of phosphorylated p70S6K and AKT compared to the control group both in vitro and in vivo, which supports the speculation that PI3K pathway is involved in this autophagic process.

## 5. Conclusion

This study indicates that A $\beta$ 25-35 treatment inhibits HT22 cell viability in a dose- and time-dependent manner and dose-dependently impairs the learning abilities of the C57 mice. The study also suggests the PI3K/AKT/mTOR/p70S6K pathway is involved in A $\beta$ 25-35-induced autophagy both in HT22 cells and in C57 mice, and these findings might provide a better understanding of AD pathogenesis and an additional model for AD research.

## Conflict of Interests

The authors report no conflict of interests.

## Authors' Contribution

Shengnuo Fan and Bei Zhang contributed equally to this work.

## Acknowledgments

This work was supported by the National Natural Science Foundation of China (no. 81372919), the Guangdong Natural Science Foundation (no. S2013010013964), and Science and Technology Fundamental Research Project of Shenzhen (no. JCYJ20120613160333560).

## References

- [1] M. Komatsu, S. Waguri, T. Chiba et al., "Loss of autophagy in the central nervous system causes neurodegeneration in mice," *Nature*, vol. 441, no. 7095, pp. 880–884, 2006.
- [2] R. A. Nixon, "The role of autophagy in neurodegenerative disease," *Nature Medicine*, vol. 19, no. 8, pp. 983–997, 2013.
- [3] F. M. LaFerla, K. N. Green, and S. Oddo, "Intracellular amyloid- $\beta$  in Alzheimer's disease," *Nature Reviews Neuroscience*, vol. 8, no. 7, pp. 499–509, 2007.
- [4] J. C. Fiala, "Mechanisms of amyloid plaque pathogenesis," *Acta Neuropathologica*, vol. 114, no. 6, pp. 551–571, 2007.
- [5] R. A. Nixon, "Autophagy, amyloidogenesis and Alzheimer disease," *Journal of Cell Science*, vol. 120, part 23, pp. 4081–4091, 2007.
- [6] P. Nilsson and T. C. Saido, "Dual roles for autophagy: degradation and secretion of Alzheimer's disease A $\beta$  peptide," *BioEssays*, vol. 36, no. 6, pp. 570–578, 2014.
- [7] B. Levine and G. Kroemer, "Autophagy in the pathogenesis of disease," *Cell*, vol. 132, no. 1, pp. 27–42, 2008.
- [8] J. Liu, L. Li, and W. Z. Suo, "HT22 hippocampal neuronal cell line possesses functional cholinergic properties," *Life Sciences*, vol. 84, no. 9–10, pp. 267–271, 2009.
- [9] Z. Zhao, R. Lu, B. Zhang et al., "Differentiation of HT22 neurons induces expression of NMDA receptor that mediates homocysteine cytotoxicity," *Neurological Research*, vol. 34, no. 1, pp. 38–43, 2012.
- [10] Z.-Y. Zhao, P. Luan, S.-X. Huang et al., "Edaravone protects HT22 neurons from H<sub>2</sub>O<sub>2</sub>-induced apoptosis by inhibiting the MAPK signaling pathway," *CNS Neuroscience & Therapeutics*, vol. 19, no. 3, pp. 163–169, 2013.
- [11] T. Harkany, I. Abraham, C. Konya et al., "Mechanisms of  $\beta$ -amyloid neurotoxicity: perspectives of pharmacotherapy," *Reviews in the Neurosciences*, vol. 11, no. 4, pp. 329–382, 2000.
- [12] J. Everse and P. W. Coates, "Neurodegeneration and peroxidases," *Neurobiology of Aging*, vol. 30, no. 7, pp. 1011–1025, 2009.
- [13] J. Götz, L. M. Ittner, N. Schonrock, and R. Cappai, "An update on the toxicity of Abeta in Alzheimer's disease," *Neuropsychiatric Disease and Treatment*, vol. 4, no. 6, pp. 1033–1042, 2008.
- [14] F. He, Y.-P. Cao, F.-Y. Che, L.-H. Yang, S.-H. Xiao, and J. Liu, "Inhibitory effects of edaravone in  $\beta$ -amyloid-induced neurotoxicity in rats," *BioMed Research International*, vol. 2014, Article ID 370368, 7 pages, 2014.
- [15] H. J. Nell, S. N. Whitehead, and D. F. Cechetto, "Age-dependent effect of  $\beta$ -amyloid toxicity on basal forebrain cholinergic neurons and inflammation in the rat brain," *Brain Pathology*, vol. 25, no. 5, pp. 531–542, 2014.
- [16] N. Ronsisvalle, G. Di Benedetto, C. Parenti, S. Amoroso, R. Bernardini, and G. Cantarella, "CHF5074 protects SH-SY5Y human neuronal-like cells from amyloid-beta 25-35 and tumor necrosis factor related apoptosis inducing ligand toxicity in vitro," *Current Alzheimer Research*, vol. 11, no. 7, pp. 714–724, 2014.
- [17] N. Cho, H. K. Lee, B. J. Jeon et al., "The effects of *Betula platyphylla* bark on amyloid beta-induced learning and memory impairment in mice," *Food and Chemical Toxicology*, vol. 74, pp. 156–163, 2014.
- [18] M.-N. Wu, L.-W. Zhou, Z.-J. Wang et al., "Colivelin ameliorates amyloid  $\beta$  peptide-induced impairments in spatial memory, synaptic plasticity, and calcium homeostasis in rats," *Hippocampus*, vol. 25, no. 3, pp. 363–372, 2015.
- [19] M. Hanenberg, J. McAfoose, L. Kulic et al., "Amyloid- $\beta$  peptide-specific darpins as a novel class of potential therapeutics for alzheimer disease," *The Journal of Biological Chemistry*, vol. 289, no. 39, pp. 27080–27089, 2014.
- [20] B. Carroll, G. Hewitt, and V. I. Korolchuk, "Autophagy and aging: implications for age-related neurodegenerative diseases," *Essays in Biochemistry*, vol. 55, no. 1, pp. 119–131, 2013.
- [21] W. H. Yu, A. Kumar, C. Peterhoff et al., "Autophagic vacuoles are enriched in amyloid precursor protein-secretase activities: implications for  $\beta$ -amyloid peptide over-production and localization in Alzheimer's disease," *International Journal of Biochemistry and Cell Biology*, vol. 36, no. 12, pp. 2531–2540, 2004.
- [22] Y. Yang, S. Chen, J. Zhang et al., "Stimulation of autophagy prevents amyloid- $\beta$  peptide-induced neuritic degeneration in PC12 cells," *Journal of Alzheimer's Disease*, vol. 40, no. 4, pp. 929–939, 2014.
- [23] M. B. Fonseca, S. Solá, J. M. Xavier, P. A. Dionísio, and C. M. P. Rodrigues, "Amyloid  $\beta$  peptides promote autophagy-dependent differentiation of mouse neural stem cells: A $\beta$ -mediated neural differentiation," *Molecular Neurobiology*, vol. 48, no. 3, pp. 829–840, 2013.

- [24] D. J. Klionsky, F. C. Abdalla, H. Abieliovich et al., “Guidelines for the use and interpretation of assays for monitoring autophagy,” *Autophagy*, vol. 8, no. 4, pp. 445–544, 2012.
- [25] Y. Yang, M. Coleman, L. Zhang, X. Zheng, and Z. Yue, “Autophagy in axonal and dendritic degeneration,” *Trends in Neurosciences*, vol. 36, no. 7, pp. 418–428, 2013.
- [26] S. Wang, S.-L. Zhou, F.-Y. Min et al., “mTOR-mediated hyperphosphorylation of tau in the hippocampus is involved in cognitive deficits in streptozotocin-induced diabetic mice,” *Metabolic Brain Disease*, vol. 29, no. 3, pp. 729–736, 2014.
- [27] A. Caccamo, S. Majumder, A. Richardson, R. Strong, and S. Oddo, “Molecular interplay between mammalian target of rapamycin (mTOR), amyloid- $\beta$ , and Tau: effects on cognitive impairments,” *Journal of Biological Chemistry*, vol. 285, no. 17, pp. 13107–13120, 2010.
- [28] I.-H. Li, K.-H. Ma, S.-J. Weng, S.-S. Huang, C.-M. Liang, and Y.-S. Huang, “Autophagy activation is involved in 3,4-methylenedioxymethamphetamine (‘Ecstasy’)-induced neurotoxicity in cultured cortical neurons,” *PLoS ONE*, vol. 9, no. 12, Article ID e116565, 2014.
- [29] R. A. Nixon, J. Wegiel, A. Kumar et al., “Extensive involvement of autophagy in Alzheimer disease: an immuno-electron microscopy study,” *Journal of Neuropathology & Experimental Neurology*, vol. 64, no. 2, pp. 113–122, 2005.
- [30] S. Lee, Y. Sato, and R. A. Nixon, “Primary lysosomal dysfunction causes cargo-specific deficits of axonal transport leading to Alzheimer-like neuritic dystrophy,” *Autophagy*, vol. 7, no. 12, pp. 1562–1563, 2011.
- [31] E. A. Dunlop and A. R. Tee, “mTOR and autophagy: a dynamic relationship governed by nutrients and energy,” *Seminars in Cell & Developmental Biology*, vol. 36, pp. 121–129, 2014.
- [32] D. Heras-Sandoval, J. M. Pérez-Rojas, J. Hernández-Damián, and J. Pedraza-Chaverri, “The role of PI3K/AKT/mTOR pathway in the modulation of autophagy and the clearance of protein aggregates in neurodegeneration,” *Cellular Signalling*, vol. 26, no. 12, pp. 2694–2701, 2014.
- [33] Y. Jin, H.-J. Sui, Y. Dong et al., “Atorvastatin enhances neurite outgrowth in cortical neurons *in vitro* via up-regulating the Akt/mTOR and Akt/GSK-3B signaling pathways,” *Acta Pharmacologica Sinica*, vol. 33, no. 7, pp. 861–872, 2012.
- [34] J. Zheng, X. Feng, L. Hou et al., “Latanoprost promotes neurite outgrowth in differentiated RGC-5 cells via the PI3K-Akt-mTOR signaling pathway,” *Cellular and Molecular Neurobiology*, vol. 31, no. 4, pp. 597–604, 2011.
- [35] R. J. Griffin, A. Moloney, M. Kelliher et al., “Activation of Akt/PKB, increased phosphorylation of Akt substrates and loss and altered distribution of Akt and PTEN are features of Alzheimer’s disease pathology,” *Journal of Neurochemistry*, vol. 93, no. 1, pp. 105–117, 2005.
- [36] C. O’Neill, “PI3-kinase/Akt/mTOR signaling: impaired on/off switches in aging, cognitive decline and Alzheimer’s disease,” *Experimental Gerontology*, vol. 48, no. 7, pp. 647–653, 2013.

## Research Article

# Overexpression of NTRK1 Promotes Differentiation of Neural Stem Cells into Cholinergic Neurons

Limin Wang,<sup>1</sup> Feng He,<sup>2</sup> Zhuoyuan Zhong,<sup>3</sup> Ruiyan Lv,<sup>3</sup> Songhua Xiao,<sup>3</sup> and Zhonglin Liu<sup>3</sup>

<sup>1</sup>Department of Neurology, Guangdong General Hospital, Guangdong Academy of Medical Sciences, Guangdong Neuroscience Institute, Guangzhou, Guangdong 510080, China

<sup>2</sup>Department of Neurology, Linyi City People's Hospital, Linyi, Shandong 276000, China

<sup>3</sup>Guangdong Provincial Key Laboratory of Malignant Tumor Epigenetics and Gene Regulation, Department of Neurology, Sun Yat-sen Memorial Hospital, Sun Yat-sen University, Guangzhou, Guangdong 510120, China

Correspondence should be addressed to Zhonglin Liu; zhonglinliu@126.com

Received 9 July 2015; Revised 25 August 2015; Accepted 16 September 2015

Academic Editor: William Z. Suo

Copyright © 2015 Limin Wang et al. This is an open access article distributed under the Creative Commons Attribution License, which permits unrestricted use, distribution, and reproduction in any medium, provided the original work is properly cited.

Neurotrophic tyrosine kinase type 1 (NTRK1) plays critical roles in proliferation, differentiation, and survival of cholinergic neurons; however, it remains unknown whether enhanced expression of NTRK1 in neural stem cells (NSCs) can promote their differentiation into mature neurons. In this study, a plasmid encoding the rat NTRK1 gene was constructed and transfected into C17.2 mouse neural stem cells (NSCs). NTRK1 overexpression in C17.2 cells was confirmed by western blot. The NSCs overexpressing NTRK1 and the C17.2 NSCs transfected by an empty plasmid vector were treated with or without 100 ng/mL nerve growth factor (NGF) for 7 days. Expression of the cholinergic cell marker, choline acetyltransferase (ChAT), was detected by fluorescent immunocytochemistry (ICC). In the presence of NGF induction, the NSCs overexpressing NTRK1 differentiated into ChAT-immunopositive cells at 3-fold higher than the NSCs transfected by the plasmid vector (26% versus 9%,  $P < 0.05$ ). The data suggest that elevated NTRK1 expression increases differentiation of NSCs into cholinergic neurons under stimulation of NGF. The approach also represents an efficient strategy for generation of cholinergic neurons.

## 1. Introduction

The family neurotrophic tyrosine receptor kinase (NTRK), also known as tropomyosin receptor kinases (Trk), includes receptors regulating synaptic strength and plasticity in the mammalian nervous system [1]. NTRK1 is one of the three major family members. NTRK1 is synthesized in basal forebrain cholinergic neurons (BFCN) and displayed on their axons, where NTRK1 is bound by its primary ligand, nerve growth factor (NGF) [2, 3]. Expression of NTRK1 precedes expression of choline acetyltransferase (ChAT), the enzyme that mediates the biosynthesis of acetylcholine and serves as a marker of cholinergic neurons, during the development of central nervous system (CNS) [4, 5]. NGF produced by neocortical neurons can experimentally induce basal forebrain cells to differentiate into cholinergic cells through activation of NTRK1 [6–10]. Hence, NTRK1 is considered to be involved in the early neuronal development.

NTRK1 is synthesized in BFCN from development to adulthood [5] and is necessary for NGF-mediated survival of the neurons [11]. BFCNs are the predominant source of cortical cholinergic input and play a central role in spatial learning and memory [12]. Loss of these neurons parallels cognitive decline and is associated with Alzheimer's disease (AD) [13], a progressive debilitating neurodegenerative disorder that typically occurs in the elderly. Postmortem examination of the brains of patients diagnosed with early stage AD has shown that NTRK1 expression is reduced in BFCN [14], indicating that downregulation of NTRK1 contributes to the loss of the neurons and the early onset of AD. In addition, genetic variants of neurotrophin system genes including NTRK1 have been found to confer susceptibility to AD [15].

Although increasing evidence suggests NTRK1 plays critical role in proliferation, differentiation, and survival of cholinergic neurons [16–19], it remains unknown whether

enhanced expression of NTRK1 in neural stem cells (NSCs) can promote their differentiation into mature neurons.

In this study, we transfected mouse NSCs (C17.2 cell line) with a plasmid encoding the NTRK1. Under induction of NGF, the NSCs overexpressing NTRK1 differentiated into cholinergic neurons at 3-fold higher efficiency than the NSCs transfected by an empty vector. To the best of our knowledge, this is the first direct evidence from cell culture to show that enhanced expression of NTRK1 promotes the differentiation of NSCs under stimulation of NGF.

## 2. Materials and Methods

**2.1. Construction of Plasmid Encoding NTRK1.** Total RNA was isolated from PC12 cell line which is derived from a pheochromocytoma of the rat adrenal medulla. NTRK1 cDNA was synthesized by reverse transcription polymerase chain reaction (RT-PCR) using oligo (dT) primer according to the manufacturer's instructions. The NTRK1 gene was amplified by PCR using primers 5'-tctgaattcatgcgtcgaggc-cagggca-3' and 5'-actctcgagctagccagaacgtccagg-3'. The amplified NTRK1 gene was digested by EcoRI and XhoI at restriction sites introduced by the primers. The digested NTRK1 gene was then purified and cloned into plasmid vector pcDNA3.1(+) digested with the same enzymes. The resulting plasmid pcDNA-NTRK1 was confirmed by DNA sequencing.

**2.2. Cell Culture and Transfection.** The mouse C17.2 neural stem cells preserved in our laboratory were seeded in 6-well plates at a density of  $1 \times 10^5$  cells with Dulbecco's Modified Eagle Medium (DMEM) containing 10% fetal bovine serum (FBS) (Invitrogen, Carlsbad, CA, USA), 5% horse serum (HS) (Sigma Aldrich, St. Louis, MO, USA), and 2 mM glutamine in a humidified incubator (5% CO<sub>2</sub>, 95% air) at 37°C. When the cell monolayers reached a confluence of  $\geq 70\%$ , the cells were subjected to a transfection procedure using the Lipofectamine 2000 (GIBCO BRL company, Foster City, CA, USA) in accordance with the manufacturer's instructions. For each well of cells, 1  $\mu$ g of plasmid DNA and 3  $\mu$ L Lipofectamine 2000 were each diluted in 50  $\mu$ L of serum-free medium. They were combined after 10 min of incubation at room temperature (RT), and the mixture was left at RT for 45 min. The mixture was supplemented with serum-free medium until final volume of 1 mL and transferred to the cells prewashed twice with serum-free medium. After 5 h, the medium was replaced with DMEM medium containing 10% FBS and 5% HS. At two days after transfection, the cells were trypsinized and subcultured in growth media containing 200  $\mu$ g/mL G418. The G418-resistant clones were pooled, amplified, and maintained in the selective growth media.

**2.3. Western Blotting.** Cells were lysed in RIPA buffer containing 25 mM Tris.Cl pH 7.6, 150 mM NaCl, 1% NP-40, 1% sodium deoxycholate, and 0.1% SDS. Total protein was measured using the BCA method. For each sample, 15  $\mu$ g of total protein was resolved by 12% sodium dodecyl sulfate polyacrylamide gel electrophoresis (SDS-PAGE) and transferred to PVDF membrane. The blots were probed with

primary antibodies specific to NTRK1 (1:1000) or  $\beta$ -actin (1:1000) at 4°C overnight. The membranes were then incubated with secondary antibodies conjugated with horseradish peroxidase (HRP) for 60 min. Proteins bands were visualized using enhanced chemiluminescence (ECL) substrate and exposed to X-ray film.

**2.4. Induction of Cellular Differentiation.** The G418-resistant C17.2 cells overexpressing NTRK1 were seeded into 6-well plates and cultured in growth media with or without 100 ng/mL NGF. As control, the G418-resistant C17.2 cells without NTRK1 overexpression were also treated with the same procedure. ChAT expression was detected after 7 days of treatment.

**2.5. Fluorescent Immunocytochemistry (ICC).** Cells were fixed in 4% polymethonal for 30 min, washed in phosphate buffered saline (PBS) three times, and blocked with normal goat serum (NGS) for 1 h. Subsequently, the cells were washed in PBS and incubated with rabbit anti-ChAT polyclonal antibody (Boster, Wuhan, China) at 4°C overnight. The cells were washed and incubated with goat anti-rabbit IgG FITC-conjugated secondary antibody at 32°C for 1 h. The labeled cells were observed under a fluorescence microscope (Nikon, TE2000). From 12 random fields of view, the ChAT-positive cells as well as the total cells were counted for each treatment group.

**2.6. Statistical Analysis.** For each field of view, the ratio of ChAT-positive cells to total cells was calculated as the frequency of cells expressing ChAT. The average mean frequency was calculated using the frequencies obtained from 12 random fields of view. The data are presented as means  $\pm$  standard deviation. The statistical analysis was performed using the Student's *t*-test as described previously [20].  $P < 0.05$  was considered statistically significant.

## 3. Results

**3.1. NTRK1 Overexpression.** The complete NTRK1 coding sequence (CDS) was amplified from PC12 rat cell line and cloned into plasmid vector pcDNA3.1(+) downstream the cytomegalovirus (CMV) promoter resulting plasmid pcDNA-NTRK1. The C17.2 neural stem cells were transfected by pcDNA-NTRK1 and empty vector pcDNA3.1(+), respectively. The G418-resistant cells were selected and expanded. The level of NTRK1 expression was measured using western blot. As shown in Figure 1, the NSCs transfected by pcDNA-NTRK1 expressed NTRK1 at much higher level than the NSCs transfected by the empty vector pcDNA3.1(+). The latter has similar level of NTRK1 as the nontransfected control C17.2 NSCs. The data confirmed that the NTRK1 gene had been successfully transfected into the NSCs.

**3.2. Identification of Cholinergic Neurons.** The NSCs proved to overexpress NTRK1 were cultured in serum-free media with or without NGF. Seven days of NGF induction resulted in efficient generation of cells expressing ChAT measured by ICC (Figure 2). As control, the G418-resistant NSCs derived from C17.2 cells transfected by the empty vector

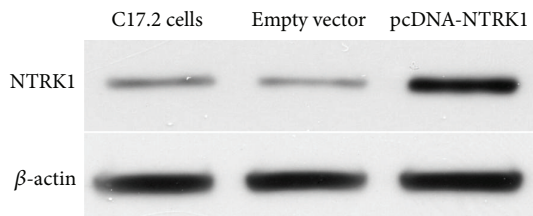


FIGURE 1: Western blot analysis of NTRK1 expression in NSCs. NTRK1 expression was measured in the nontransfected C17.2 cells, and G418-resistant C17.2 cells derived from transfections using pcDNA-NTRK1 or the empty vector pcDNA3.1(+).  $\beta$ -actin was measured to serve as an internal loading control.

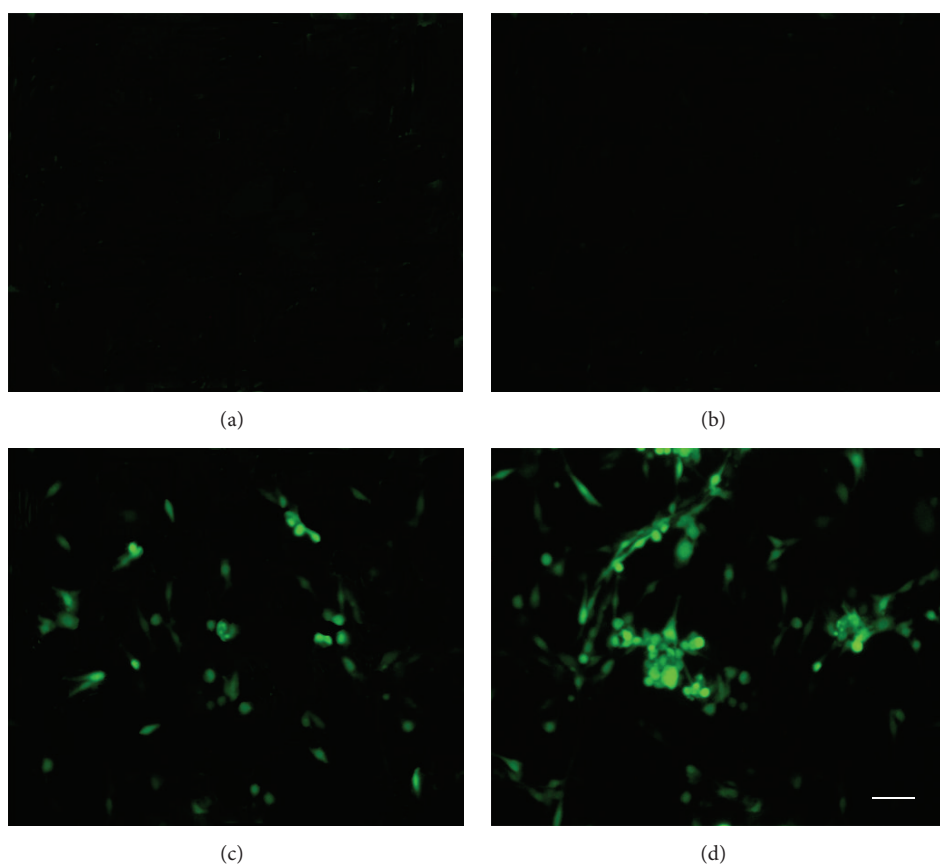


FIGURE 2: ICC photomicrographs (400x) of G418-resistant NSCs with or without NGF treatment. In the absence of NGF exposure, pcDNA3.1(+)-transfected cells (a) and pcDNA-NTRK1-transfected cells (b) showed no ChAT expression. Following NGF exposure for 7 d, both pcDNA3.1(+)-transfected cells (c) and pcDNA-NTRK1-transfected cells (d) were immunopositive for ChAT (FITC labeled).

were also treated similarly. Although NGF treatment led to generation of ChAT-expressing cells, less efficient than the NSCs overexpressing NTRK1, the ChAT-negative cells included astrocytes and small round cells which may at least include nondifferentiated NSCs. From 12 random fields of view, the ChAT-positive cells and the total cells were counted. Under treatment of NGF, the percentage of ChAT-positive cells was  $25.98 \pm 4.71\%$  for NSCs overexpressing NTRK1 and was  $9.08 \pm 3.26\%$  for NSCs transfected by the plasmid vector ( $P < 0.01$ ). Of note, the experiment represents

three independent experiments which had consistent findings.

The ChAT positive ratio of NTRK1-transfected cells exposed to NGF was  $(25.98 \pm 4.71)\%$ , and that of pseudotransfected cells exposed to NGF was  $(9.08 \pm 3.26)\%$  ( $P < 0.01$ , NGF-treated NTRK1-transfected versus NGF-treated pseudotransfected exposed to NGF) (Figure 3). No fluorescent labeling was observed in either the nontransfected control cells or the NTRK1-transfected cells that were not exposed to NGF.

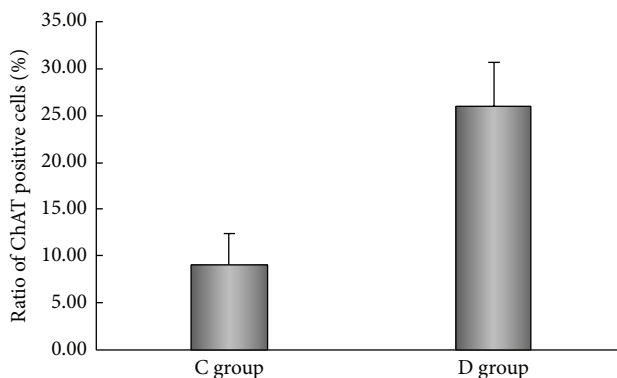


FIGURE 3: Ratio of ChAT positive cells differentiated in the NTRK1 transfected group (D) was higher than that in the pseudotransfected group (C) ( $n = 12$ ).

#### 4. Discussion

Growing evidence shows that NTRK1 plays critical role in the differentiation and survival of neurons. However, it remains obscure how NTRK1 expression level in neural stem cells affects differentiation efficiency. In this study, the full length NTRK1 gene was stably transferred into neural stem cells. Overexpression of NTRK1 led to 3-fold higher differentiation efficiency (26% versus 9%) when subjected to stimulation by NGF. These findings indicate that differentiation of NSCs into a cholinergic fate is related to expression level of NTRK1.

NTRK1 (TrkA), NTRK2 (TrkB), and NTRK3 (TrkC) are the three major members of NTRK family. These three receptors together with another membrane receptor, p75NTR, play central role in the proliferation, differentiation, and survival of neurons [1]. NTRK1 is bound and activated by NGF [21, 22]. NT-3 also binds NTRK1 as a lower affinity heterologous ligand [23]. In the presence of p75NTR, NGF shows enhanced activation of NTRK1 [24–26], as p75NTR increases the rate of NGF association with NTRK1 [27]. On the other hand, NT3 becomes much less effective at activating NTRK1 due to the presence of p75NTR [28–30]. NTRK1 gene has 17 exons [31]. Different isoforms of NTRK1 also affect the neurotrophin-mediated signaling. The isoform lacking a short insert in the juxtamembrane region is activated efficiently only by NGF. Presence of this insert increases activation of NTRK1 by NT3 without affecting its activation by NGF [32]. Although the differentiation of NSCs is regulated by a complicated network *in vivo*, use of *in vitro* cultured cells allows us to determine the effect of NGF on the differentiation of NSCs without interfering by other neurotrophins, consistent with previous finding that the NSCs (C17.2 cells) synthesize NTRK1 [33], but at a much lower level compared to the cells stably transfected by plasmid encoding NTRK1 gene. This is expected as the CMV promoter which drives the NTRK1 gene in the plasmid has been proven highly active in neurons [34].

C17.2 is an immortalized mouse neural progenitor cell line which was established by retroviral-mediated transduction of the *v-myc* oncogene into mitotic progenitor cells of neonatal mouse cerebellum [35]. C17.2 cells are maintained as

monolayer in cell culture dishes in DMEM supplemented with fetal calf serum and horse serum. Under induction of serum-free media containing neurotrophins, the C17.2 cells differentiate into neurons and astrocytes with distinct morphology. ChAT is the enzyme responsible for synthesis of acetylcholine from acetyl-coenzyme A and choline and is found in high concentration in cholinergic neurons, both in the central nervous system (CNS) and in peripheral nervous system (PNS). Our data showed that the parental C17.2 cells could be induced to differentiate into cholinergic neurons, but less efficient than the NSCs overexpressing NTRK1. This is most likely because more molecules of NTRK1 displayed on the membrane facilitate the NGF-mediated signal transduction.

NTRK1 consists of an extracellular ligand-binding domain, a single transmembrane domain, and an intracellular tyrosine kinase domain. After being bound by nerve growth factor (NGF), NTRK1 is activated and initiates a signaling cascade of molecules including Ras/Raf/MAP kinase, PI3K/Akt, and PLC- $\gamma$  [36–38]. However, it remains poorly understood how these NTRK1-activated pathways regulate the differentiation and survival of the neurons. It has been found that the cholinergic gene locus contains a region located within 2 kb immediately 5' border of the R-exon, which confers responsiveness to NGF in reporter gene assays [39]. The region contains two activator protein 1 (AP-1) sites as well as a putative cAMP response element (CRE) [40]. However, the precise mechanism between NTRK1 activation and ChAT expression has not yet been appreciated. In this study we focused on cholinergic neurons generated under induction of NGF. But it is interesting to examine whether other types of neurons were generated during the process. Furthermore, the cholinergic neurons may also synthesize other transmitters as reported previously [41].

In conclusion, the present study demonstrated that overexpression of NTRK1 facilitates more efficient differentiation of NSCs into cholinergic neuron in response to NGF treatment. It also represents an efficient strategy to generate cholinergic neurons.

#### Conflict of Interests

The authors declare that there is no conflict of interests.

#### Authors' Contribution

Limin Wang and Feng He contributed equally to this work.

#### Acknowledgments

This work was supported by the Science and Technology Planning Project of Guangdong Province (no. 2014A020212148) and Guangzhou city (no. 1563000791). This work was supported by Grant [2013]163 from Key Laboratory of Malignant Tumor Molecular Mechanism and Translational Medicine of Guangzhou Bureau of Science and Information Technology and Grant KLB09001 from the Key Laboratory of Malignant Tumor Gene Regulation and Target Therapy of Guangdong Higher Education Institutes.

## References

- [1] E. J. Huang and L. F. Reichardt, "Trk receptors: roles in neuronal signal transduction," *Annual Review of Biochemistry*, vol. 72, pp. 609–642, 2003.
- [2] L. Harel, B. Costa, M. Tcherpakov et al., "CCM2 mediates death signaling by the TrkA receptor tyrosine kinase," *Neuron*, vol. 63, no. 5, pp. 585–591, 2009.
- [3] R. W. Alfa, M. H. Tuszyński, and A. Blesch, "A novel inducible tyrosine kinase receptor to regulate signal transduction and neurite outgrowth," *Journal of Neuroscience Research*, vol. 87, no. 12, pp. 2624–2631, 2009.
- [4] J. A. Luther and S. J. Birren, "Neurotrophins and target interactions in the development and regulation of sympathetic neuron electrical and synaptic properties," *Autonomic Neuroscience: Basic and Clinical*, vol. 151, no. 1, pp. 46–60, 2009.
- [5] Y. Li, D. M. Holtzman, L. F. Kromer et al., "Regulation of TrkA and ChAT expression in developing rat basal forebrain: evidence that both exogenous and endogenous NGF regulate differentiation of cholinergic neurons," *Journal of Neuroscience*, vol. 15, no. 4, pp. 2888–2905, 1995.
- [6] A. Tacconelli, A. R. Farina, L. Cappabianca, A. Gulino, and A. R. Mackay, "TrkAIII: a novel hypoxia-regulated alternative TrkA splice variant of potential physiological and pathological importance," *Cell Cycle*, vol. 4, no. 1, pp. 8–9, 2005.
- [7] P. Dutta, A. Koch, B. Breyer et al., "Identification of novel target genes of nerve growth factor (NGF) in human mastocytoma cell line (HMC-1 (V560G c-Kit)) by transcriptome analysis," *BMC Genomics*, vol. 12, article 196, 2011.
- [8] V. Nikoletopoulou, H. Lickert, J. M. Frade et al., "Neurotrophin receptors TrkA and TrkB cause neuronal death whereas TrkC does not," *Nature*, vol. 467, no. 7311, pp. 59–63, 2010.
- [9] A. Lambiase, A. Micera, G. Pellegrini et al., "In vitro evidence of nerve growth factor effects on human conjunctival epithelial cell differentiation and mucin gene expression," *Investigative Ophthalmology and Visual Science*, vol. 50, no. 10, pp. 4622–4630, 2009.
- [10] D. Sareen, M. Saghizadeh, L. Ornelas et al., "Differentiation of human limbal-derived induced pluripotent stem cells into limbal-like epithelium," *Stem Cells Translational Medicine*, vol. 3, no. 9, pp. 1002–1012, 2014.
- [11] M. V. Sofroniew, N. P. Galletly, O. Isacson, and C. N. Svendsen, "Survival of adult basal forebrain cholinergic neurons after loss of target neurons," *Science*, vol. 247, no. 4940, pp. 338–342, 1990.
- [12] K. Okada, K. Nishizawa, T. Kobayashi, S. Sakata, and K. Kobayashi, "Distinct roles of basal forebrain cholinergic neurons in spatial and object recognition memory," *Scientific Reports*, vol. 5, Article ID 13158, 2015.
- [13] M. Mesulam, "The cholinergic lesion of Alzheimer's disease: pivotal factor or side show?" *Learning and Memory*, vol. 11, no. 1, pp. 43–49, 2004.
- [14] S. E. Counts and E. J. Mufson, "The role of nerve growth factor receptors in cholinergic basal forebrain degeneration in prodromal Alzheimer disease," *Journal of Neuropathology and Experimental Neurology*, vol. 64, no. 4, pp. 263–272, 2005.
- [15] A. Cozza, E. Melissari, P. Iacopetti et al., "SNPs in neurotrophin system genes and Alzheimer's disease in an Italian population," *Journal of Alzheimer's Disease*, vol. 15, no. 1, pp. 61–70, 2008.
- [16] K. J. Park, C. A. Gross, I. Aubert, D. R. Kaplan, and F. D. Miller, "P75NTR-dependent, myelin-mediated axonal degeneration regulates neural connectivity in the adult brain," *Nature Neuroscience*, vol. 13, no. 5, pp. 559–566, 2010.
- [17] O. M. E. Abdel-Salam, "Stem cell therapy for Alzheimer's disease," *CNS and Neurological Disorders—Drug Targets*, vol. 10, no. 4, pp. 459–485, 2011.
- [18] C. J. Bissonnette, L. Lyass, B. J. Bhattacharyya, A. Belmadani, R. J. Miller, and J. A. Kessler, "The controlled generation of functional basal forebrain cholinergic neurons from human embryonic stem cells," *Stem Cells*, vol. 29, no. 5, pp. 802–811, 2011.
- [19] Y. Itou, R. Nochi, H. Kurabayashi, Y. Saito, and T. Hisatsune, "Cholinergic activation of hippocampal neural stem cells in aged dentate gyrus," *Hippocampus*, vol. 21, no. 4, pp. 446–459, 2011.
- [20] X. Zhang, S.-Y. Wanda, K. Brenneman et al., "Improving *Salmonella* vector with rec mutation to stabilize the DNA cargoes," *BMC Microbiology*, vol. 11, article 31, 2011.
- [21] D. R. Kaplan, B. L. Hempstead, D. Martin-Zanca, M. V. Chao, and L. F. Parada, "The trk proto-oncogene product: a signal transducing receptor for nerve growth factor," *Science*, vol. 252, no. 5005, pp. 554–558, 1991.
- [22] R. Klein, S. Jing, V. Nanduri, E. O'Rourke, and M. Barbacid, "The trk proto-oncogene encodes a receptor for nerve growth factor," *Cell*, vol. 65, no. 1, pp. 189–197, 1991.
- [23] L. Ivanisevic, W. Zheng, S. B. Woo, K. E. Neet, and H. U. Saragovi, "TrkA receptor 'hot spots' for binding of NT-3 as a heterologous ligand," *The Journal of Biological Chemistry*, vol. 282, no. 23, pp. 16754–16763, 2007.
- [24] D. O. Clary and L. F. Reichardt, "An alternatively spliced form of the nerve growth factor receptor TrkA confers an enhanced response to neurotrophin 3," *Proceedings of the National Academy of Sciences of the United States of America*, vol. 91, no. 23, pp. 11133–11137, 1994.
- [25] B. L. Hempstead, D. Martin-Zanca, D. R. Kaplan, L. F. Parada, and M. V. Chao, "High-affinity NGF binding requires coexpression of the trk proto-oncogene and the low-affinity NGF receptor," *Nature*, vol. 350, no. 6320, pp. 678–683, 1991.
- [26] A. M. Davies, K.-F. Lee, and R. Jaenisch, "p75-deficient trigeminal sensory neurons have an altered response to NGF but not to other neurotrophins," *Neuron*, vol. 11, no. 4, pp. 565–574, 1993.
- [27] D. Mahadeo, L. Kaplan, M. V. Chao, and B. L. Hempstead, "High affinity nerve growth factor binding displays a faster rate of association than p140trk binding. Implications for multi-subunit polypeptide receptors," *Journal of Biological Chemistry*, vol. 269, no. 9, pp. 6884–6891, 1994.
- [28] C. Brennan, K. Rivas-Plata, and S. C. Landis, "The p75 neurotrophin receptor influences NT-3 responsiveness of sympathetic neurons in vivo," *Nature Neuroscience*, vol. 2, no. 8, pp. 699–705, 1999.
- [29] P. S. Mischel, S. G. Smith, E. R. Vining, J. S. Valletta, W. C. Mobley, and L. F. Reichard, "The extracellular domain of p75NTR is necessary to inhibit neurotrophin-3 signaling through TrkA," *The Journal of Biological Chemistry*, vol. 276, no. 14, pp. 11294–11301, 2001.
- [30] M. Bibel, E. Hoppe, and Y.-A. Barde, "Biochemical and functional interactions between the neurotrophin receptors trk and p75(NTR)," *The EMBO Journal*, vol. 18, no. 3, pp. 616–622, 1999.
- [31] L. Alberti, C. Carniti, C. Miranda, E. Roccato, and M. A. Pierotti, "RET and NTRK1 proto-oncogenes in human diseases," *Journal of Cellular Physiology*, vol. 195, no. 2, pp. 168–186, 2003.
- [32] C. Strohmaier, B. D. Carter, R. Urfer, Y.-A. Barde, and G. Dechant, "A splice variant of the neurotrophin receptor trkB with increased specificity for brain-derived neurotrophic factor," *The EMBO Journal*, vol. 15, no. 13, pp. 3332–3337, 1996.

- [33] N. Nguyen, S. B. Lee, Y. S. Lee, K.-H. Lee, and J.-Y. Ahn, "Neuroprotection by NGF and BDNF against neurotoxin-exerted apoptotic death in neural stem cells are mediated through TRK receptors, activating PI3-kinase and MAPK pathways," *Neurochemical Research*, vol. 34, no. 5, pp. 942–951, 2009.
- [34] R. Holehonnur, S. K. Lella, A. Ho, J. A. Luong, and J. E. Ploski, "The production of viral vectors designed to express large and difficult to express transgenes within neurons," *Molecular Brain*, vol. 8, article 12, 2015.
- [35] E. Y. Snyder, D. L. Deitcher, C. Walsh, S. Arnold-Aldea, E. A. Hartwieg, and C. L. Cepko, "Multipotent neural cell lines can engraft and participate in development of mouse cerebellum," *Cell*, vol. 68, no. 1, pp. 33–51, 1992.
- [36] D. R. Kaplan and F. D. Miller, "Neurotrophin signal transduction in the nervous system," *Current Opinion in Neurobiology*, vol. 10, no. 3, pp. 381–391, 2000.
- [37] M. V. Chao, "Neurotrophins and their receptors: a convergence point for many signalling pathways," *Nature Reviews Neuroscience*, vol. 4, no. 4, pp. 299–309, 2003.
- [38] A. Simi and C. F. Ibáñez, "Assembly and activation of neurotrophic factor receptor complexes," *Developmental Neurobiology*, vol. 70, no. 5, pp. 323–331, 2010.
- [39] B. Schütz, R. Damadzic, E. Weihe, and L. E. Eiden, "Identification of a region from the human cholinergic gene locus that targets expression of the vesicular acetylcholine transporter to a subset of neurons in the medial habenular nucleus in transgenic mice," *Journal of Neurochemistry*, vol. 87, no. 5, pp. 1174–1183, 2003.
- [40] B. Berse, I. Lopez-Coviella, and J. K. Blusztajn, "Activation of TrkA by nerve growth factor upregulates expression of the cholinergic gene locus but attenuates the response to ciliary neurotrophic growth factor," *Biochemical Journal*, vol. 342, no. 2, pp. 301–308, 1999.
- [41] B. Lavoie and A. Parent, "Pedunculopontine nucleus in the squirrel monkey: distribution of cholinergic and monoaminergic neurons in the mesopontine tegmentum with evidence for the presence of glutamate in cholinergic neurons," *Journal of Comparative Neurology*, vol. 344, no. 2, pp. 190–209, 1994.